

Electronic Thesis and Dissertation Repository

8-24-2020 10:00 AM

Material evaluation and structural monitoring of early-age masonry structures

Kyle Dunphy, *The University of Western Ontario*

Supervisor: Sadhu, Ayan, *The University of Western Ontario*

A thesis submitted in partial fulfillment of the requirements for the Master of Engineering Science degree in Civil and Environmental Engineering

© Kyle Dunphy 2020

Follow this and additional works at: <https://ir.lib.uwo.ca/etd>



Part of the [Civil Engineering Commons](#), [Other Electrical and Computer Engineering Commons](#), and the [Structural Engineering Commons](#)

Recommended Citation

Dunphy, Kyle, "Material evaluation and structural monitoring of early-age masonry structures" (2020). *Electronic Thesis and Dissertation Repository*. 7235.
<https://ir.lib.uwo.ca/etd/7235>

This Dissertation/Thesis is brought to you for free and open access by Scholarship@Western. It has been accepted for inclusion in Electronic Thesis and Dissertation Repository by an authorized administrator of Scholarship@Western. For more information, please contact wlsadmin@uwo.ca.

Abstract

During the initial construction period, “*early-age*” masonry walls are susceptible to lateral loads induced by wind or earthquake, which may result in damages or catastrophic failures. To mitigate such consequences at construction sites, temporary bracings are adopted to provide lateral support to masonry walls until they are matured enough to serve as the inherent lateral system of the structure. However, current temporary bracing guidelines provide oversimplified design due to the lack of available information on the material properties of early-age masonry. Moreover, there are no existing techniques for monitoring masonry walls to detect cracks due to construction activities. This thesis presents innovative techniques for the structural health monitoring of early-age masonry structures at construction sites. The stress-strain behavior of early-age masonry structures that have been cured for 3 to 72 hours was estimated through a detailed uniaxial tensile testing program. A 3D microscopic numerical model with cohesion-based interaction surfaces was developed to accurately estimate the tensile behavior and failure patterns of early-age masonry assemblages. A novel hybrid image processing and deep learning algorithm are then proposed for the efficient crack detection in masonry structures at the construction site. Finally, a general discussion on the results, contributions, and future research are provided.

Keywords

Masonry structures; Construction; Stress-strain behavior; Finite element modeling; Experimental testing; Structural health monitoring; Image processing; Deep learning; Crack detection.

Summary for Lay Audience

Early-age masonry structures are weak in the lateral direction and are susceptible to damages due to extreme wind events and earthquakes. To mitigate the potential of these damages, temporary braces are installed to provide structural resistance against these natural phenomena. However, the design of these braces is based on the strength properties of the masonry structures. During the initial construction period, there is minimal information available on these properties, and therefore the bracing design becomes inaccurate. Additionally, there are no existing autonomous techniques to detect cracks of masonry structures under construction. In this thesis, the detection and prevention of damages in early-age masonry structures form the key objectives. Numerous experiments were conducted to determine the tensile strength of masonry prisms during initial construction. A numerical model was developed to accurately depict the strength and failure behavior of masonry so that the strength can be estimated during construction. Lastly, an automatic crack detection algorithm was created using a hybrid Artificial Intelligence technique to allow for the rapid detection of damages.

Acknowledgments

I would like to express my sincere gratitude to my supervisor Dr. Ayan Sadhu. I began researching with Dr. Sadhu while I was pursuing the NSERC USRA internship during my undergraduate studies at Lakehead. This experience is what inspired me to continue my graduate studies with him at Western. Dr. Sadhu is an excellent teacher and mentor, and I am honored to have the opportunity to grow as an individual researcher under his supervision.

I would like to thank Dr. Bennett Banting and the Canadian Masonry Design Centre (CMDC) for providing me with space, resources, time, and knowledge to conduct my experimental work. Moreover, I would like to thank CMDC and Mitacs Accelerate grant for providing the funding to conduct the research presented in this thesis. To Dr. Ayman El Ansary and Dr. Maged Youssef, I thank you for your continued guidance and patience during the preparation of my thesis. I would also like to thank Dr. Jinfei Wang for her valuable time to review my thesis as the university examiner. Special thanks are reserved for Dr. Sreekanta Das at the University of Windsor for providing me images of masonry structures that I used in the thesis.

I would also like to thank the team members of my research group for helping me with my experimentations. I would not have been able to complete the very demanding and time extensive work without the help of Mohamed, Premjeet, Shea, and Sandeep, and I hope to be able to return the favor in kind.

I would like to thank those who have been with me since the beginning of my academic career, in particular my parents Ken and Grace, and my sisters Maegan and Shannon. To my wife, Katelyn, it was your love and support that allowed me to reach this goal, and it will be your devotion going forward that will give me strength as I face new challenges.

Table of Contents

Abstract	ii
Summary for Lay Audience	iii
Acknowledgments.....	iv
Table of Contents	v
List of Tables	viii
List of Figures	x
List of Appendices	xiii
Nomenclature	xv
Abbreviations	xviii
1 Introduction	1
1.1 Research Background	1
1.2 Literature Review.....	3
1.2.1 Material Properties of Early-age Masonry.....	3
1.2.2 Identification of Cracks in Early-age Masonry structures	12
1.3 Gap Areas.....	15
1.4 Research Objectives.....	16
1.5 References.....	17
2 Experimental Evaluation of Early-age Masonry	24
2.1 Preparation of Test Specimens.....	24
2.2 Proposed Test Setup.....	28
2.3 Data Acquisition and Wireless Data Transmission	29
2.4 Details of the Experiments.....	32
2.4.1 Evaluation of Tensile Stress.....	33
2.4.2 Evaluation of Uniaxial Tensile Strain.....	34

2.5	Early-Age Masonry Properties	35
2.5.1	Extraction of Stress-Strain Curves.....	35
2.5.2	Modulus of Elasticity of Early-age Masonry	38
2.5.3	Summary of Strength Parameters for Early-age Masonry	42
2.6	Outlier Analysis	43
2.6.1	Correlation Between Material Properties and Curing Times.....	46
2.7	Conclusions.....	50
2.8	References.....	50
3	Finite Element Study of Early-age Masonry.....	52
3.1	Model Parameters of the Masonry Prism.....	52
3.1.1	FEM of the Mortar	54
3.2	Finite Element Modeling of Masonry Assemblage	59
3.2.1	Definition of the Simulation Model.....	59
3.2.2	Quasi-static Condition	64
3.2.3	Mesh Sensitivity Analysis.....	67
3.3	Comparison of Numerical and Experimental Results.....	68
3.4	Case Study – Masonry Walls under Construction	74
3.4.1	Macro model of the Masonry Wall.....	74
3.4.2	FEM of the Early-Age Masonry Wall	80
3.5	Conclusions.....	85
3.6	References.....	86
4	Robust Crack Identification Technique for Masonry Structures	88
4.1	Implementation of CNN	88
4.1.1	Basics of CNN	88
4.1.2	Crack identification using the traditional CNN approach.....	91
4.1.3	Image Preparation	94

4.1.4	Performance evaluation of the CNN technique	97
4.2	Hyper-parameter Tuning.....	99
4.2.1	Shortcomings of Standalone CNN technique	103
4.3	The Proposed Hybrid Crack Identification Technique	103
4.3.1	Determination of optimal threshold.....	107
4.3.2	Proposed Hybrid Method.....	113
4.3.3	Results and discussions.....	115
4.4	Conclusions.....	118
4.5	References.....	119
5	Conclusions and Summary.....	122
5.1	Conclusions.....	122
5.2	Contributions.....	123
5.3	Future Work	123
	Appendices.....	125
	Curriculum Vitae	135

List of Tables

Table 2.1: Mean calibration weight of the test setup for tensile testing.	33
Table 2.2 Summarization of regression parameters for a 3-hour sample.	41
Table 2.12: Summarization of the effect of IQRT on parameter COV.	46
Table 3.1: Variation of σ_d and E with the curing period.	53
Table 3.2: Variation of stress concentration factor with the curing period.	55
Table 3.3: Strength parameters of a 3-hour cured sample in ABAQUS.	56
Table 3.4: Material model for cohesion-based contact elements for a 3-hour curing period.	59
Table 3.5: Section assignment and the associated material model.	61
Table 3.6: Loading curves for varying time intervals.	66
Table 3.7: Mesh sensitivity analysis of 3D simulated masonry course.	67
Table 3.8: Comparison of experimental and numerical stress-strain parameters for the 3-hour curing.	72
Table 3.9: Percentage error between experimental and numerical stress-strain parameters across all the curing periods.	73
Table 3.10: Strength, cohesion and loading parameters for the macro model across all curing periods.	78
Table 3.11: Percentage error between experimental and numerical stress-strain parameters for macro model across all curing periods.	79
Table 3.12: Variation of the curing period with height of the masonry wall.	82
Table 4.1: Detailed description of the selected CNN layers.	94
Table 4.2: Initial accuracy of the selected CNN architecture.	99

Table 4.4: Hypertuning of the network and training parameters.	103
Table 4.3: Statistical results obtained from the IP.	112
Table 4.5: Algorithm parameters for pixel-level masonry crack detection.	117

List of Figures

Figure 1.1: (a) Catastrophic failure of masonry wall (DOC 2013), (b) a temporary external bracing system during construction (Lang 2005).	1
Figure 1.2: Typical location of cracks and their patterns in masonry walls (Pereira and Pereira 2015).	2
Figure 1.3: Flowchart of the thesis.	17
Figure 2.1: Prepared concrete masonry block with painters' tape.	25
Figure 2.2: A certified mason constructing samples for experimentation.	26
Figure 2.3: Mechanical mixing of Type S Spec Mix mortar.	26
Figure 2.4: Preparation of the masonry prism; (a) prepared mortar, (b) applied mortar, (c) finished joint.	27
Figure 2.5: Finalized construction of a masonry assemblage for testing.	28
Figure 2.6: Apparatus configuration for uniaxial tensile testing.	29
Figure 2.7: Attachment of LVDTs to a two-course masonry prism.	30
Figure 2.8: Individual components of the displacement sensing and data acquisition system; (a) DAQ, (b) LVDT, (c) signal conditioner, and (d) base station.	31
Figure 2.9: A typical data acquisition setup of the LVDT.	32
Figure 2.10: Raw strain and applied load.	36
Figure 2.11: Individual and averaged stress-strain curves of a typical test.	37
Figure 2.12: Rigid shift of the stress-strain curve.	38
Figure 2.13: Typical de-bonding failure of early-age masonry.	39
Figure 2.14: Comparison of the linear regression model and experimental data.	41

Figure 2.15: IQRT of the peak strain of a 4-hour dataset.	45
Figure 2.16: Variation of E and σ_d with the curing period.....	47
Figure 2.17: The proposed equation for variation of (a) debonding stress and (b) E with the curing period.	49
Figure 3.1: Stress concentration of the simulated mortar.	54
Figure 3.2: Variation of stress concentration factor over the simulation period.	56
Figure 3.3: 2D planar sketches and 3D solids of masonry blocks and mortars.	60
Figure 3.4: Preliminary assemblage structure in ABAQUS.	62
Figure 3.5: Application of loading and boundary conditions.	64
Figure 3.6: Variation of the kinetic, internal, and external energy.	65
Figure 3.7: Variation of the percentage of kinetic energy with load duration.	66
Figure 3.8: (a) Final assemblage partition and (b) mesh distribution.	68
Figure 3.9: Normal stress gradients (a) before and (b) after the failure.	69
Figure 3.10: Average normal stress (a) and average logarithmic strain (b) extracted from ABAQUS.	71
Figure 3.11: Comparison of experimental and numerical E values.	72
Figure 3.12: Macroscopic model of the expanded masonry prism.	76
Figure 3.13: Normal stress gradients (a) before and (b) after the failure of the macro model.	80
Figure 3.14: (a) Macroscopic model of the early-age masonry wall and (b) applied wind loading.....	81
Figure 3.15: Deflection of simulated early-age masonry wall under wind and gravity loads.	84

Figure 4.1: Schematic of a simple CNN architecture (O’Shea and Nash 2015).....	89
Figure 4.2: The proposed CNN architecture.....	93
Figure 4.3: Segmented grayscale image for the creation of the training database.	96
Figure 4.4: Data augmentation of the training database of the damaged specimens.....	97
Figure 4.5: Confusion matrix of the testing data.	98
Figure 4.6: Variation of training, validation and testing accuracy with (a) external dropout layer P_r , (b) internal dropout layer P_r , (c) momentum, (d) L_2R , (e) LRDF, (f) MBS and (g) ILR.	103
Figure 4.7: (a) RGB, and (b) greyscale image of an undamaged masonry surface.	104
Figure 4.8: RGB (a) and greyscale (b) image of damaged masonry.	105
Figure 4.9: Variation of damage localization with (a) low TH , (b) average TH , and (c) high TH	106
Figure 4.10: Crack detection using the proposed image-thresholding method.	107
Figure 4.11: Variation of matrix density with the threshold value.	109
Figure 4.12: True classification of the cracks in the masonry prism.	110
Figure 4.13: Variation of MCC with TH for determining optimal TH	111
Figure 4.14: Variation of N with ρ_m	112
Figure 4.15: Flowchart of the proposed hybrid method.	114
Figure 4.16: A sample test image (a) undamaged, and (b) damaged state.	116
Figure 4.17: Classification of the sub-images by CNN.	116
Figure 4.18: Pixel-level localization of early-age masonry crack.	118

List of Appendices

Appendix A.1: Summary of tensile Parameters at 3-hour curing	125
Appendix A.2: Summary of tensile Parameters at 4-hour curing	125
Appendix A.3: Summary of tensile parameters at 6-hour curing	126
Appendix A.4: Summary of tensile parameters at 7-hour curing	126
Appendix A.5: Summary of tensile parameters at 13-hour curing	127
Appendix A.6: Summary of tensile parameters at 18-hour curing	127
Appendix A.7: Summary of tensile parameters at 24-hour curing	128
Appendix A.8: Summary of tensile parameters at 48-hour curing	128
Appendix A.9: Summary of tensile parameters at 72-hour curing	129
Appendix B.1: Strength parameters of a 4-hour cured sample in ABAQUS.	129
Appendix B.2: Strength parameters of a 6-hour cured sample in ABAQUS.	129
Appendix B.3: Strength parameters of a 7-hour cured sample in ABAQUS.	129
Appendix B.4: Strength parameters of a 13-hour cured sample in ABAQUS.	130
Appendix B.5: Strength parameters of a 18-hour cured sample in ABAQUS.	130
Appendix B.6: Strength parameters of a 24-hour cured sample in ABAQUS.	130
Appendix B.7: Strength parameters of a 48-hour cured sample in ABAQUS.	130
Appendix B.8: Strength parameters of a 72-hour cured sample in ABAQUS.	130
Appendix C.1: Material model for cohesion-based contact elements for a 4-hour curing period.	131

Appendix C.2: Material model for cohesion-based contact elements for a 6-hour curing period.	131
Appendix C.3: Material model for cohesion-based contact elements for a 7-hour curing period.	132
Appendix C.4: Material model for cohesion-based contact elements for a 13-hour curing period.	132
Appendix C.5: Material model for cohesion-based contact elements for a 18-hour curing period.	133
Appendix C.6: Material model for cohesion-based contact elements for a 24-hour curing period.	133
Appendix C.7: Material model for cohesion-based contact elements for a 48-hour curing period.	134
Appendix C.8: Material model for cohesion-based contact elements for a 72-hour curing period.	134

Nomenclature

E	Modulus of Elasticity [MPa]
ε_d	Debonding strain
σ_d	Debonding stress [kPa]
σ	Tensile normal stress [Pa]
P_i	Tensile load at time step 'i' [lbs]
P_o	Initial tensile load at time step 't = 0' [lbs]
$\varepsilon_{t,i}$	Elastic tensile strain at time step 'i'
δ_i	Displacement at time step 'i' [mm]
δ_o	Initial displacement at time step 't = 0' [mm]
D_m	Depth of mortar [mm]
δ_1	Absolute displacement of LVDT 1 [mm]
δ_2	Absolute displacement of LVDT 2 [mm]
V	Raw voltage reading [V]
Y_i	Independent vector
X_i	Dependent vector
\hat{Y}_i	Prediction of the dependent vector
B	Regression parameter
R^2	Coefficient of Determination
SST	Sum of the squared total errors
SSR	Sum of the squared residual errors
SSE	Sum of the squared errors
Y^*	Mean value of the real independent variable, Y_i
COV	Coefficient of variation
$\bar{\sigma}$	Standard deviation

μ	Mean value
$Q1$	First quartile
$Q3$	Third quartile
N	Number of samples
IQR	Interquartile range
ρ	Density [ton/mm ³]
ν	Poissons' ratio
K_t	Stress concentration factor
σ_{max}	Maximum normal stress [MPa]
σ_n	Nominal stress [MPa]
t	Traction stress vection [MPa]
t_n	Traction stress in the normal direction [MPa]
t_s	Traction stress in the longitudinal shear direction [MPa]
t_t	Traction stress in the transverse shear direction [MPa]
K_{mn}	Traction stress in the normal direction [N/mm ³]
K_{ss}	Traction stress in the longitudinal shear direction [N/mm ³]
K_{tt}	Traction stress in the transverse shear direction [N/mm ³]
K	Traction stiffness vector [N/mm ³]
P_f	Load at failure [N]
φ	Reduction factor
σ_a	Applied tensile stress [MPa]
A_e	Surface area of ears [mm ²]
W	External energy applied [mJ]
E_I	Internal energy [mJ]
E_T	Total energy [mJ]

E_K	Kinetic energy [mJ]
ε_l	Logarithmic strain at time step ‘ l ’
H	Height of the expanded masonry unit [mm]
H_B	Height of the block [mm]
H_M	Height of half the mortar [mm]
E_B	Modulus of elasticity of the block [MPa]
E_M	Modulus of elasticity of the mortar [MPa]
p	External wind pressure normal to the surface [kPa]
p_i	Internal wind pressure normal to the surface [kPa]
I_w	Importance factor
q	Reference velocity pressure [kPa]
c_e	Exposure factor
c_{ei}	Exposure factor for internal wind pressure
c_t	Topographic factor
c_g	Gust effect factor
c_{gi}	Gust effect factor for internal wind pressure
c_p	External pressure coefficient
c_{pi}	Internal pressure coefficient
f_c	Number of filters
I	Input height or width
f	Height or width of the kernel
P	Number of zero padding
S	Stride of the kernel
P_c	Probability of classification
TP	True positive reading
TN	True negative reading

<i>FP</i>	False positive reading
<i>FN</i>	False negative reading
T	Threshold matrix
U	Undamaged image matrix
D	Damaged image matrix
L	Damage localization matrix
CR	Crack output image matrix
<i>TH</i>	Threshold value
ρ_m	Matrix density
$\rho_{o,m}$	Optimal matrix density
N_o	Normalization factor
<i>A</i>	Coefficient of exponential regression
<i>C</i>	Coefficient of exponential regression
<i>MCC</i>	Matthews correlation coefficient

Abbreviations

AI	Artificial Intelligence
FEM	Finite Element Modelling
IRA	Initial Absorption Rate
UDEC	Universal Distinct Element Code
RC	Reinforced Concrete
DOF	Degree of Freedom
SHM	Structural Health Monitoring
IP	Image Processing
DIC	Digital Image Correlation

UAVs	Unmanned Aerial Vehicles
SVM	Support Vector Machine
CMDC	Canadian Masonry Design Centre
LVDT	Linear Variable Differential Transformer
DAQ	Data Acquisition
IQRT	Interquartile Range Technique
L ₂ R	L ₂ Regularization
LRDF	Learn Rate Drop Factor
MBS	Mini-batch Size
ILR	Initial Learn Rate

1 Introduction

1.1 Research Background

During initial construction periods, early-age masonry walls exhibit only a fraction of their design load resistances. This fractional strength is attributed to the active curing of the mortar and grout used in masonry construction during the first 12 to 24 hours following construction (I. M. Institute 2013). Although the early-age masonry structures have significant strength in the vertical direction due to their self-weight, they often have negligible lateral strength. With such circumstances, earthquakes or wind events have the potential to cause catastrophic failure or damages, as shown in Figure 1.1 (a), resulting in economic loss or injury to construction workers. To mitigate this situation, external bracing, as shown in Figure 1.1 (b) has been employed as a temporary bracing system (Jin and Gambatese 2020) to provide lateral resistance for masonry structures during construction. However, there is a lack of guidelines and known properties of early-age masonry, making the current bracing systems subjective and over-conservative to prevent structural failure and economic losses.



Figure 1.1: (a) Catastrophic failure of masonry wall (DOC 2013), (b) a temporary external bracing system during construction (Lang 2005).

As a result, early-age masonry walls are susceptible to premature cracking due to lateral loads and failure of inadequate temporary bracing systems, as shown in Figure 1.2. Although a crack is considered as minimal damage, significant catastrophes can occur if

the initial crack is overlooked once it is detected. A crack can lead to more significant structural damage, including flaking, spalling, and mortar loss. For early-age masonry walls at the construction site, there does not exist any autonomous technique for the detection of cracks. Though existing bracing guidelines define the creation of a restriction zone to protect masons in the case of a catastrophic failure (MCAA 2012), this has to be monitored by a qualified person and does not necessarily progressively monitor any damage that has occurred. By autonomously detecting cracks in early-age masonry structures through Artificial Intelligence (AI) techniques, catastrophic failures could be minimized, preventing economic and physical damages.

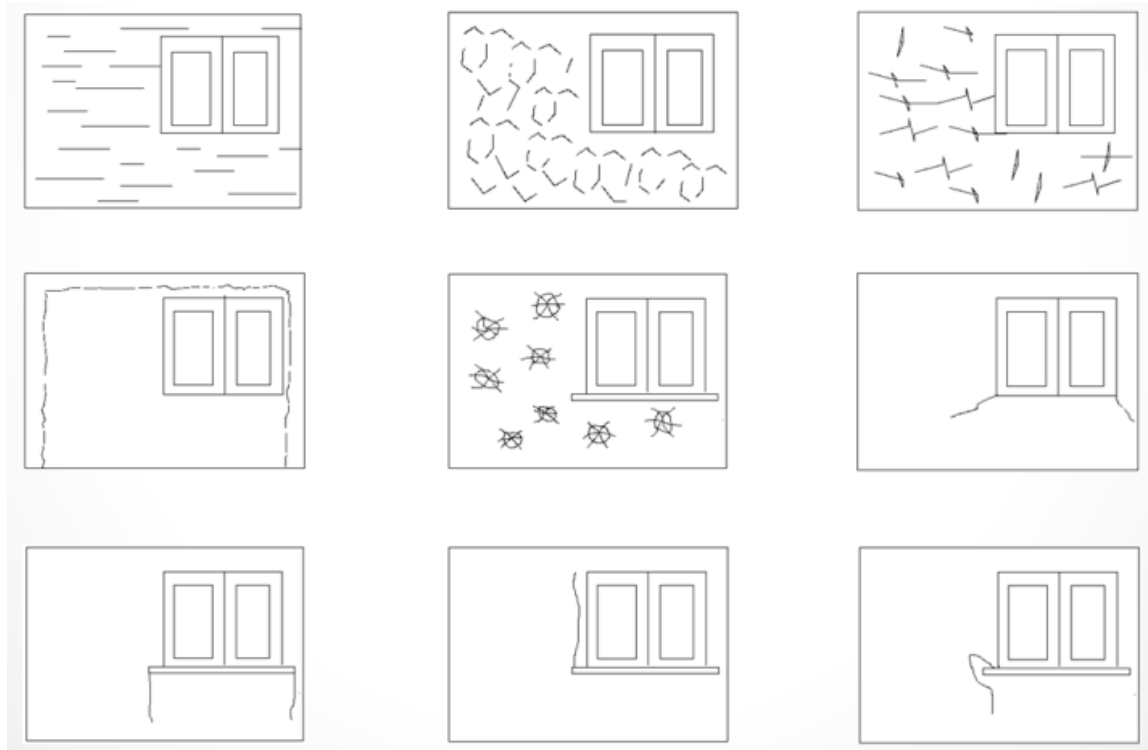


Figure 1.2: Typical location of cracks and their patterns in masonry walls (Pereira and Pereira 2015).

Structural Health Monitoring (Cawley 2018) offers attractive tools to inspect, retrofit, and control of newer and existing structures. In this thesis, various SHM strategies are adopted to monitor and retrofit early-age masonry structures at the construction site. At one end, a detailed experimental and simulation study is conducted to evaluate the early-age masonry

prisms that can be used to set up the design guidelines of the temporary bracing and prevent the failure of newly constructed masonry walls at the job site. On the other hand, an autonomous crack detection method is developed to identify the onset of faults or anomalies in the early-age masonry walls at the construction site. The following section discusses the existing experimental and modeling techniques to determine early-age masonry properties as well as the state-of-the-art crack detection techniques for structural systems.

1.2 Literature Review

1.2.1 Material Properties of Early-age Masonry

To design safe, long-lasting, and stable structures, extensive information must be known about the material properties of both mature and early-age structure. Without any well-defined material properties, one will result in an oversimplified design, which may lead to catastrophic failures, causing economic damages and loss of human life. However, it is often not viable to run laboratory simulations on scaled models to accurately determine the correlation between different material models and stress conditions due to the cost. Therefore, the development of accurate numerical models using Finite Element Modeling (FEM) techniques becomes another timely and cost-effective alternative that is explored in this thesis.

1.2.1.1 Experimental Evaluation of Early-age Masonry Properties

Hamid and Chukwunve (1986) performed various experimental studies to quantify the influence of various parameters on the compression behavior of masonry prisms. It was concluded that significant behavioral difference is exhibited for face shell and full-bedded hollow mortar prisms. Additionally, the height-to-thickness ratio showed an influence on the failure behavior of prisms. Ewing and Kowalsky (2004) investigated the elastic compressive behavior of confined clay-brick masonry assemblages. The elastic and plastic compressive behavior and strength parameters were investigated using 15 masonry prisms with varying confinement ratios and compared with the modified Kent-Park model for

confined masonry. They concluded that the addition of confinement plates significantly increased the compressive strength of the masonry assemblages.

The previous research concluded that in most circumstances for masonry structures, the mortar joints act as planes of potential weakness between the blocks. Primarily, this is contributed by the low strength properties of mortar when compared to the block. Moreover, the variability of mechanical bonding between the mortar and block across the interface during curing results in variable bonding strength. As such, significant research has been conducted to quantify the variability of masonry bond strength. The bond strength characteristics for pressed earth block masonry was extensively studied by Walker (1999). Combinations of earth blocks with variable material properties and cement-lime and cement-soil mortars were tested using a bond wrench test to quantify flexural strength. It was concluded that bond strength is directly proportional to block strength and that minimal change in flexural bond strength occurs after one day of curing. Moreover, clay and moisture content of the mortar has a direct influence on the available bond strength of the masonry assemblages.

Reddy and Gupta (2006) studied the tensile bond strength of masonry couplets constructed from soil-cement blocks with cement-soil mortars. The influence of initial moisture content of the block, block characteristics, clay fraction, and cement ratio and workability of the mortar were assessed with respect to the impact on tensile bond strength. They concluded that there is optimal block moisture content that produces the highest tensile bond strength, which is influenced by the composition of the block. Additionally, the tensile bond strength increases with increased flow and cement content present in the masonry block. Reddy *et al.* (2007) further investigated the influence of surface roughness, geometric properties of frogs, and the type surface coating applied to the soil-cement blocks on the shear-bond strength, compressive strength, and stress-strain relationship of soil-cement assemblages constructed using various mortar types. They concluded that the introduction of roughness, coatings, or inclusion of frogs on the block surface leads to an increase in shear-bond strength when compared to blocks with smooth surfaces. A similar study was conducted that studied the influence of shear bond strength on the compressive strength of masonry for varying strength ratios of masonry prisms by Reddy and Vyas (2008). They concluded

that masonry compressive strength increases with increased shear bond strength for modular ratios of block-mortar less than one.

However, the complexities of defining masonry behavior are not limited to the development of accurate constitutive models but the variety of materials that are defined as “masonry” constituents. As such, many studies have been conducted to quantify the influence of independent material and geometric properties on the strength behaviors of masonry. Groot and Larbi (1999) applied numerical models of microscopic movement of water in cementitious materials available in the literature to evaluate the influence of water flow on block-mortar bond strength. Their experimental results supported the conclusion that for each block-mortar combination, there is an optimal initial absorption rate (IRA) that results in the maximum bond strength. Moreover, it was concluded that both directions of water flow across the block-mortar influence had a significant influence on the developmental bond strength. Moreover, it was further concluded that the IRA had a predominant influence over the compressive strength of clay-brick masonry assemblages by Kaushik *et al.* (2007). Moreover, the compressive strength of masonry assemblages is proportional to the compressive strength of the individual components, provided a high brick-mortar strength ratio exists.

Costigan and Pavia (2009) investigated the effects of curing duration on compressive, flexural, and bond strength of masonry assemblages constructed using a lime-based mortar. They concluded that increased curing time results in increased compressive and flexural strength of mortars. Furthermore, increased mortar compressive strength and bond strength has minimal influence on the compressive strength of masonry assemblages with high brick-mortar strength ratios. The Young’s modulus and compressive strength of masonry assemblages comprised of clay bricks and pure lime-sand mortars were quantified by Drougkas *et al.* (2016). Compression and flexural tests were conducted on cored clay brick samples, mortar bricks, and stack-bonded masonry assemblages to determine the strength parameters. It was concluded that though the masonry assemblages performed better than the estimate by European codes, the relatively low strength and increased curing time required for lime-based mortars do not make them appropriate for construction.

Sarangapani *et al.* (2005) conducted a similar study to investigate the influence of independent parameters on block-mortar bond and, subsequently, the compressive strength of masonry assemblages. For low-cement ratio mortars, the addition of surface treatments, and composite mortar materials (such as lime and soil) increases the flexural bond strength while high-cement ratio mortars exhibit higher flexural bond strengths. Moreover, an increase in bond strength was proven to have a proportional increase in the compressive strength of masonry assemblages. The influence of the variation in material, elastic, and plastic properties of brick-mortar interfaces under uniaxial compressive loads were further investigated by Vermeltfoort *et al.* (2007). Moisture-based material properties such as block absorption, shrinkage, and mortar workability in addition to block roughness were discussed with regards to the impact on overall brick-mortar interface strength. Moreover, the properties of the brick-mortar interface heavily influenced the overall compressive behavior of masonry assemblages. As such, models developed based on separate testing of block and mortar showed substantial inaccuracies with respect to compressive behavior.

Lumantarna *et al.* (2014) compared the compressive behavior of masonry assemblages extracted from historic masonry structures and those constructed in a laboratory setting. From the experimental data, a numerical model was developed to represent the compressive behavior of the assemblage based on the strength of the masonry components. It was concluded that there was significant agreement between compressive strength parameters of the laboratory and real work masonry assemblages. Similar experimental testing on masonry assemblages was conducted by Barbosa *et al.* (2010) with four varying block/mortar arrangements with different strength properties to ascertain their compressive strength and compared numerical method strategies. The elastic and inelastic properties of the mortar and block were extracted from three sets of axial compression conducted on masonry prisms, cylindrical samples, and beams. Overall, 3D numerical modeling most accurately predicted the ultimate load and failure pattern of masonry assemblages comparing with simplified 2D plane-stress and –strain models, though some inaccuracies were present for deformation approaching the ultimate load. A hybrid method to characterize the shear behavior of lightweight masonry assemblages using optimized experimental parameters in a numerical model was proposed by Sousa *et al.* (2013). Diagonal tension tests were conducted on a small set of masonry assemblages with the

addition of values provided by European codes to develop a microscopic 3D FEM, which was calibrated to optimize the experimental parameters. Though the simplified model accurately captured the shear behavior of the samples pre-failure, the addition of interface properties would improve post-failure performance.

1.2.1.2 Numerical Evaluation of Early-age Masonry Properties

Sarhosis and Sheng (2014) identified material properties for low bond strength masonry and developed a numerical model using the Universal Distinct Element Code (UDEC). Several masonry walls with openings were constructed to develop a constitutive model to be implemented in a numerical model. The parameters were further optimized using least square and moving square regressions in addition to evolutionary algorithms to minimize discrepancies between experimental and numerical results. An excellent agreement was observed between experimental results and the UDEC model. Previously, masonry was described as an anisotropic and heterogeneous material with the properties dependent on the directionality of the analysis conducted. As such, defining an accurate Finite Element Modelling (FEM) of masonry is often complex and requires several parameters that are derived from experimental testing. Extensive research has already been conducted on this subject to quantify both the failure behavior and material parameters of masonry constituents. As demonstrated, there are several parameters to be considered for the numerical modeling of masonry structures.

FEM of masonry are typically grouped into two categories based on the method employed by the researchers to represent the material properties as follows:

- Homogeneous models assume the material properties are averaged across the entire continuum of the numerical element; mortar and block are represented by the weighted properties (Zucchini and Lourenco 2009).
- Heterogeneous models assume the material properties of each constituent are represented by individual material properties.

Furthermore, the classification may depend on the complexity by which each material property is geometrically represented in the modeling space:

- Microscopic models assume all masonry constituents (mortar, block, grout, and reinforcement) are modeled as discrete continuum elements while interactions between components are represented by contact interface between slave and master nodes. Though these models require high computational capacity, they can capture local behavior and failure of masonry with reasonable accuracy (Ghosh *et al.* 1994, Sirajuddin *et al.* 2011, Bolhassani *et al.* 2015, Abdulla *et al.* 2017).
- Mesoscopic models, similarly, assume that the masonry elements are extended such that the element represents the masonry block and half the thickness of the mortar. Interaction between elements is again represented by contact interface interactions (Casolo 2004).
- Macroscopic models assume all masonry constituents are modeled as a singular element with an averaged representation of the geometric parameters. Though these models can only capture the global behavior of the masonry structure, they are computationally inexpensive to analyze (Dhanasekar and Haider 2007, Caddemi *et al.* 2017).

Dhanasekar and Haider (2007) applied an explicit FE analysis to a macro model for unreinforced masonry and wide-spaced reinforced masonry. The stress behavior of the model was defined by a Von Mises failure surface with a Rankine type tension cut-off, implementing smeared crack elements, and plasticity-based interface elements for the masonry units and mortar, respectively. The authors concluded that the explicit FE model successfully predicted the global behavior of both types of shear masonry walls. An improved interpretation of the ultimate failure behavior of three-course masonry prisms under uniaxial compression using a 3D nonlinear FEM analysis was provided by Koksall *et al.* (2010). The failure mechanism of the prisms was shown to have a significant correlation to the compressive strength of the grout. Furthermore, weaker grout strength creates increased lateral tensile stress in the top block leading to failure, while when the grout strength was comparable to the block, the failure was centralized in the prism. The

nonlinear behavior of hollow masonry was studied by Sayed-Ahmed and Shrive (2010) through the implementation of a shell-element analysis. While continuum element analysis was unable to capture the failure behavior of these structural elements, the proposed analysis demonstrates the web splitting and buckling typical of this nonlinear behavior.

Bolhassani *et al.* (2015) investigated the behavior of ungrouted and grouted masonry assemblages through FE micro-models developed in ABAQUS. Through experimental testing, failure, and yield criteria, in addition to elastic-plastic behavior was established. The masonry unit and mortar were modeled using the Concrete Damaged Plasticity model, with the plastic behavior of the mortar joints defined using traction-separation in addition to pre-defined damage initiation and evolution criteria. An excellent agreement was found between the experimental studies and the numerical model based on the methodology described. In conclusion, grouted masonry assemblages depicted higher compressive and diagonal tensile strengths due to the reinforcement of the weak mortar joints by the grout.

For masonry walls, additional modeling techniques that equate full-scale walls to equivalent struts or frames are also implemented by the researchers as they are less complex than traditional models and give accurate predictions of the global behavior under various loading conditions. Al-Chaar *et al.* (2003) demonstrated that the eccentric equivalent strut method applied to fully infilled masonry panels are transferable to those with openings. An empirical relationship for the in-plane reduction of the struts was developed through a comparison of FE models developed in ANSYS and pushover analyses conducted on full-scale reinforced concrete infilled frames. Moreover, this technique was accurately demonstrated to predict the ultimate strength of reinforced concrete (RC) infill structures with openings. A reduction factor proposed by Mondal *et al.* (2008) applied to a Single Equivalent Diagonal Strut method to calculate the initial stiffness of the infilled frame with a central opening. Through several parametric studies, it was demonstrated that the strut width reduction factor proposed showed reasonable agreement with experimental data.

Typically, the development of FEM for various types of masonry walls is directly related to the type of load the structure. Extensive research has been conducted on in-plane loading with respect to masonry walls. This category of loading includes loads due to gravity,

concentrated vertical loads, and the transference of lateral loads from support systems attached to these walls. Ghosh *et al.* (1994) employed ABAQUS to model masonry walls under vertical and/or horizontal loads. The authors used a micro-modeling approach in which both the brick and mortar are modeled as separate continuum elements. The basis of this approach is on an inelastic constitutive model commonly used for concrete in ABAQUS, assuming elastic-plastic material behavior with predominate tensile failure mode. Moreover, a smeared crack model was implemented to determine the origin and orientation of the cracking in the mortar and masonry units. Extended capabilities of a previous homogenized micro-mechanical quarter cell masonry model to a full periodic cell to represent the structural response of masonry walls under in-plane loads were developed by Zucchini *et al.* (2009). Furthermore, basic failure modes such as tensile and compression crack, diagonal crack, and masonry crushing were captured by this technique. Through extensive research has been conducted on this loading category, it did not consider the critical loading type for masonry walls. Out-of-plane loading created by strong winds and earthquakes creates large nonlinear structural responses for these structures resulting in severe cracking and both local and global failure.

Aref and Dolatshahi (2013) developed a robust approach to model structural responses of masonry structures under 3D loading. A comprehensive material model was implemented in ABAQUS to simulate the combinations of in-plane and out-of-plane monotonic and cyclic loading. Varela-Riveria *et al.* (2011) investigated the out-of-plane behavior of confined masonry walls with two different simply supported conditions; four-sided and three-sided using various numerical techniques. By investigating the experimental results of six confined masonry walls, it was concluded the maximum pressure and cracking pattern for each support condition were similar due to the top confining element acting as fourth support for the three-sided support condition. Moreover, this element restricts the maximum pressure the wall can support and therefore is critical to overall structural design. Implementing the FEM in SAP2000, the cracking pressures determined by this approach showed significant agreement with the experimental results.

A FEM developed for unreinforced masonry walls that accounted for both the in-plane and out-of-plane behavior of the structure to quantify the dependency of out-of-plane capacity

on in-plane damage due to cyclic loads were developed by Agnihotri *et al.* (2013). Moreover, the relationship between the out-of-plane capacity and geometric properties of the wall, aspect, and slenderness ratios was investigated. Upon validation of the FEM, it was concluded there was a strong correlation between in-plane damage and reduction in out-of-plane capacity. Additionally, it was found that the out-of-plane capacity was inversely proportional to the aspect ratio and slenderness ratio, though the maximum reduction was found to be independent of both these properties. Korkmaz *et al.* (2007) conducted a nonlinear structural analysis to determine the stability of RC structures with masonry infill walls subjected to earthquakes. Five 3-story RC frame structures with various masonry infill configurations were investigated, and the nonlinear responses were analyzed through static pushover technique. Though masonry infill walls provide increased stiffness and enhanced stability of RC frames, irregular distributions of these infills may cause significant displacements or base shears. A calibrated FEM technique for analyzing the nonlinear load-deformation behavior and failure mechanism of masonry infilled RC frames was offered by Stavridis and Shrive (2010). Addressing the inadequacies of smeared-crack elements for predicting the brittle shear behavior of RC members and mixed-mode fractures mortar joints, the authors combined discrete and smeared-crack modeling for a novel approach. This modeling technique was shown to have significant robustness with respect to identifying failure mechanisms and nonlinear load-deformation of the infilled RC frames.

Another underrepresented topic in the research conducted is the response of masonry walls under cyclic loading. Cyclic loads are defined by a continuous repetitive force that is applied to a structure. The repetitive nature of this load causes structural fatigue as the material properties deteriorate with each load cycle. Moreover, once fatigue occurs, there is a significant possibility that the structure will fail at a smaller load increment or time interval. Kanit and Donduren (2010) investigated the capability of the FEM software ANSYS to simulate the out-of-plane behavior of masonry walls under cyclic loading. A full-scale model was developed in ANSYS to represent the experimental masonry test wall under cyclic loads. Comparison of the displacements, stress distribution, and material strength of experimental and numerical models depict excellent agreeability between results.

Numerous FEM techniques were applied to simulate the response of the RC frame with masonry infill wall under both monotonic and cyclic loadings by Allouzi *et al.* (2010). Using ABAQUS, the masonry constituents of the model were simulated using a Concrete Damaged Plasticity model with cohesive interfaces with a linear damage evolution law to represent the brick and mortar, respectively. The proposed model showed good agreement with the experimental data of previously published research by Mehrabi and Singh (1997), implying this model has the potential to be implemented for the development of hysteresis responses under earthquake ground motion. Karapitta *et al.* (2010) developed a smeared-crack model to investigate the cyclic loading response for unreinforced masonry walls. Through experimental validations, it was demonstrated the model developed on strain-based constitutive relationships provided an accurate prediction of hysteretic behavior under these loading conditions. However, several areas of future development were suggested by the authors to improve these FEM with regards to cyclic loading. This included defining material relationships, such as tensile and compressive damage coupling, shear strength, and vertical compressive stress dependency and the variation of Poisson's ratio in the post-cracking range.

Caddemi *et al.* (2017) developed a novel macroscopic numerical modeling technique for simulating nonlinear behavior of historic masonry structures. This approach improved upon available simplified in-plane models in literature through the inclusion of an additional degree of freedom (DOF) to capture the out-of-plane behavior of masonry walls. Moreover, geometric enhancements were implemented for the modeling of curved masonry elements. Moreover, the FEM technique was validated through further development by the authors. From the results, this model shows significant robustness with respect to the simulation of nonlinear behavior of historic masonry structures.

1.2.2 Identification of Cracks in Early-age Masonry structures

Structural Health Monitoring (SHM) has been an invaluable tool for the assessment of existing damaged structures. Similar to aging structures, SHM techniques could be applied to early-age structures under construction to prevent premature damages (e.g., crack or any other anomalies) that would result in economic loss, structural damage, or physical harm.

Traditionally, these structural inspections have been conducted manually by trained engineers; however, numerous drawbacks have been addressed with the human-based inspection. Such inspections are often susceptible to human-based error, time-consuming, and the logistics of inspecting all elements of tall buildings or long-span bridges are often difficult. Therefore, automated techniques such as image processing (IP) and Artificial Intelligence (AI) techniques have been implemented for the autonomous detection of damages in various structures. Mohan and Poobal (2018) conducted a critical review of various IP techniques for engineering structures. Though most image processing techniques presented significant accuracy for crack detection, generally, it is difficult to determine any physical information about the cracks such as length, width, depth, and type. Additionally, the resolution of the images taken for the crack identification correlates to the accuracy of the crack detection for image-based techniques (Zakeri *et al.* 2017).

For masonry structures, digital image correlation (DIC) is an effective image processing technique that has been extensively studied for crack detection. The displacement measurements of masonry walls under uniaxial compression using DIC were analyzed by Shih *et al.* (2006). The authors concluded that the initial cracking of the masonry walls could be located by using DIC on the displacement field. Moreover, Tung *et al.* (2008) further refined this method and determined that the strain concentrations from the von Mises strain can better localize cracking in masonry walls using DIC. Didier *et al.* (2018) computed a probabilistic model to determine damage states of plastered unreinforced masonry walls using DIC of displacement measurements. The strains and displacements of several plastered URM walls were tested under quasi-static cyclic loads that were tracked using DIC to quantify normalized crack length and area. This data was implemented in developing a probabilistic damage model to assess the probability of no damage, cracking, or plaster loss occurring for a given wall displacement.

Additional IP techniques based on grayscale binarization, edge detectors, wavelet transforms, and various filters have also been used to classify damages of masonry structures. A smartphone application developed using a grayscale binarization image processing technique to determine the percentage of the cracked area in masonry, and concrete images were presented by Martins *et al.* (2013). A comparative study was

conducted between traditional manual and digital measurement techniques and the proposed mobile platform. The authors concluded that the proposed method was more accurate, time-efficient, and allowed for results to be determined in the field when compared to manual inspection techniques. Ellenberg *et al.* (2014) investigated the application of IP techniques for the detection of masonry cracks using unmanned aerial vehicles (UAVs). Various methods were outlined, including edge detection, percolation, fractal method, and tensor voting to implement them with regards to crack detection. The authors concluded that the majority of these methods have a significant correlation between background noise and accuracy. Moreover, UAVs present unique challenges for SHM as they are extremely susceptible to environmental factors such as wind.

Pereira and Pereira (2015) compared Sobel filter and Particle filters for crack detection of masonry structures using UAVs with embedded image processing algorithms. Particle filters were found to be less accurate than Sobel filters for crack detection, they are more time-efficient and, therefore, more compatible with UAV-based SHM. Sankarasrinivasan *et al.* (2015) used hat transform, Hue Saturation Value thresholding, and grayscale thresholding to localize efflorescence and cracks on masonry surfaces. By combining hat transform and HSV thresholding allowed for superior detection of cracks via UAVs using binary images to prevent erroneous noise. However, environmental effects such as wind speed resulted in errors; therefore, mechanical stabilizers and advanced flight controls should be implemented with UAV inspections. Though these methods provide significant accuracy, image processing techniques are extremely susceptible to noise and require the user to pre-define the features they wish to extract from the images, where AI techniques such as deep learning methods can offer attractive solutions.

Therefore, deep learning techniques, in particular Convolutional Neural Networks (CNNs), have been applied for the autonomous inspection of masonry structures as they obtain features inherently and have high classification accuracy. Chaiyasarn *et al.* (2018) applied a hybrid CNN-SVM algorithm for crack detection of historic masonry structures. The addition of support vector machines (SVMs) as the classifier for CNN improved the binary classification accuracy when compared with traditional CNNs. However, the accuracy of the classification is dependent on the quality of images; for example, mortar lines were

often shown to have been incorrectly classified as cracks due to their feature similarities. Similar research conducted by Chaiyasarn *et al.* (2018b) showed that SVM provided the most accurate classification compared to softmax and random forest classifiers. Additionally, the merit of generating 3D models of damaged historical masonry structures using UAVs was discussed. A modified *ZF-net* for a proposed Faster Region CNN was implemented by Ali *et al.* (2019) to localize and detect damages in masonry structures. After training on a dataset of 1000 sub-images taken from UAV and smartphones, the mean average precision was 96.5%, concluding the proposed method is robust with respect to the real-time detection of masonry cracks. Further increasing the database size for training could potentially increase the accuracy of the faster R-CNN classification.

Brackenbury *et al.* (2019) investigated the effect of separating mortar joints from images obtained through visual inspection of defective masonry on the accuracy of damage classification using CNNs. Numerous sub-images of various surface damages were captured from a multi-span masonry arch bridge in Cambridge and used to train the existing *GoogLeNet Inception V3* architecture through transfer learning. The authors concluded that separating mortar and block regions before classification results in a more accurate prediction of undamaged masonry areas and improved classification of noisy masonry images. Wang *et al.* (2019) applied a Faster R-CNN model based on *ResNet 101* to detect spalling and efflorescence of historic masonry structures. The smartphone and camera-based platforms developed using this architecture showed significant precision with respect to damage classification irrespective of lighting and image size. However, expanding the database to include additional damage types and addressing differences in image angles and distances may contribute to improved precision of the model.

1.3 Gap Areas

Based on the above literature reviews, the following gap areas are found:

- There has been no research to investigate the behavior of early-age masonry during the initial 72-hour period of curing. Therefore, no standardized design procedure can be developed for temporary external bracing based on actual early-age material

properties, often resulting in oversimplifications that contribute to ineffective systems and, ultimately, failure.

- There exists no 3D FEM that represents the uniaxial tensile behavior of early-age masonry assemblages. Though many models have been developed for masonry, none of them are representative of the behavior of early-age masonry at various curing times. Moreover, there is a lack of adequate modeling strategies of cohesive-based interaction surface that would represent the debonding failure of masonry structures under tensile loads.
- Monitoring systems for potential construction damages are limited to anemometers to measure wind speeds and designing restriction zones and guidelines based on these wind speeds. There exist no robust autonomous techniques for the detection of cracks on masonry structures under construction. Though IP techniques can localize cracks accurately, they are extremely susceptible to noise due to environmental conditions. Conversely, though the existing deep learning techniques are more robust with respect to environmental noise, localization of cracks at the pixel level is time extensive.

1.4 Research Objectives

To address the above gap areas, the following objectives are identified to be met through this thesis:

- Extensive experimental studies will be conducted on two-course concrete masonry assemblages to determine early-age strength properties of masonry prisms.
- A robust material model will be explored to design 3D numerical models in ABAQUS to study and predict the behavior of early-age masonry assemblages.
- A novel hybrid monitoring system based on image processing and deep learning will be developed to detect masonry cracks in early-age masonry structures.

In this thesis, **Chapter 1** provides a general introduction to the topic and presents the relevant background literature, gap areas, and research objectives of this thesis. **Chapter 2** discusses the experimental evaluation of the early-age properties of masonry prisms. Using

these material properties, **Chapter 3** presents the numerical development of a 3D early-age masonry model in ABAQUS and a comparison of numerical and experimental results. **Chapter 4** discusses the accuracy of a novel hybrid model for the identification of cracks in early-age masonry structures. Finally, **Chapter 5** concludes with the research contributions and the future work of this research. **Figure 1.3** shows a brief flowchart and organization of the thesis.

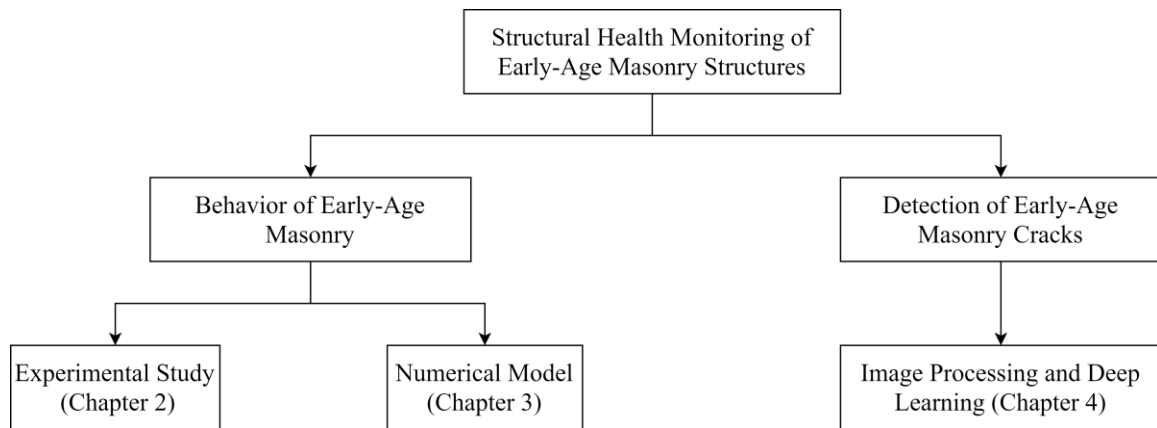


Figure 1.3: Flowchart of the thesis.

1.5 References

Abdulla, K., Cunningham, L. and Gillie, M. (2017), “Simulating masonry wall behavior using a simplified micro-model approach,” *Engineering Structures*, 151, 349-365.

Agnihotti, P., Singhal, V. and Rai, D. (2013), “Effect of in-plane damage on out-of-plane strength of unreinforced masonry walls,” *Engineering Structures*, 57, 1-11.

Ali, L., Khan, W. and Chaiyasarn, K. (2019), “Damage detection and localization in masonry structure using faster region convolutional networks”, *International Journal of GEOMATE*, 17(59), 98 – 105.

Allouzi, R., Irfanoglu, A. and Haikal, G. (2010), "Nonlinear finite element modeling of RC frame-masonry wall interaction under cyclic loadings," *Tenth U.S. National Conference on Earthquake Engineering*, Anchorage, Alaska.

Aref, A. and Dolatshahi, K. (2013), "A three-dimensional cyclic meso-scale numerical procedure for simulation of unreinforced masonry structures," *Computers and Structures*, 120, 9-23.

Barbosa, C., Lourenco, P. and Hanai, J. (2010), "On the compressive strength prediction for concrete masonry prisms", *Materials and Structures*, 43, 331-344, DOI 10.1617/s11527-009-9492-0.

Bolhassani, M., Hamid, A., Lau, A. and Moon, F. (2015), "Simplified micro modeling of partially grouted masonry assemblages," *Construction and Building Materials*, 83, 159-173.

Brackenbury, D., Brilakis, I. and DeJong, M. (2019), "Automated defect detecting for masonry arch bridges", *International Conference on Smart Infrastructure and Construction (ICSIC): Driving data-informed decision-making*, 3 – 9.

Caddemi, S., Calio, I., Cannizzaro, F. and Panto, B. (2017), "New frontiers on seismic modeling of masonry structures," *Frontiers in Built Environment*, 3(39), 1-16.

Casolo, S. (2004), "Modelling in-plane micro-structure of masonry walls by rigid elements," *International Journal of Solids and Structures*, 41, 3625-3641.

Cawley, P. (2018), "Structural health monitoring: Closing the gap between research and industrial deployment". *Structural Health Monitoring*, 17(5), 1225 - 1244.

Chaiyasarn, K., Khan, W., Ali, L., Sharma, M., Brackenbury, D. and DeJong, M. (2018), "Crack detection in Masonry Structures using Convolutional Neural Networks and Support Vector Machines", *35th International Symposium on Automation and Robotics in Construction (ISARC)*, Berlin, Germany.

Chaiyasarn, K., Sharma, M., Ali, L., Khan, W. and Poovarodom, N. (2018), “Crack detection in historical structures based on convolutional neural network”, *International Journal of GEOMATE*, 15(51), 240 – 251.

Costigan, A. and Pavia, S. (2009), “Compressive, flexural and bond strength of brick/lime mortar masonry”, *Proceedings of PROHITEC 09 – Mazzolani editor*, Taylor and Francis Group, London, 1609-1615.

Dhanasekar, M. and Haider, W. (2007), “Explicit finite element analysis of lightly reinforced masonry shear walls,” *Computers and Structures*, 86, 15-26.

Didier, M., Abbiati, G., Hefti, F., Broccardo, M. and Stojadinovic, B. (2018), “Damage quantification in plastered unreinforced masonry walls using digital image correlation”, *10th Australasian Masonry Conference*, Sydney, Australia.

Drougkas, A., Roca, P. and Molins, C. (2016), “Compressive strength and elasticity of pure lime mortar masonry”, *Materials and Structures*, 49, 983-999, DOI 10.1617/s11527-015-0553-2.

Ellenberg, A., Kontsos, A., Bartoli, I. and Pradhan, A. (2014), “Masonry Crack Detection Application of an Unmanned Aerial Vehicle”, *Computing in Civil and Building Engineering*.

Ewing, B. and Kowalsky, M. (2004), “Compressive Behaviour of Unconfined and Confined Clay Brick Masonry”, *Journal of Structural Engineering*, 130(4), 650-661.

Ghosh, A. K., Made, A. M. and Colville, J. (1994), “Finite Element Modeling of Unreinforced Masonry,” *Proceedings of the 10th International brick/block masonry conference*, Calgary, 61-70.

Groot, C. and Larbi, J. (1999), “The influence of water flow (reversal) on bond strength development in young masonry”, *HERON*, 44(2), 63-78.

Hamid, A. and Chukwunenye, A. (1986), “Compression Behaviour of Concrete Masonry Prisms,” *Journal of Structural Engineering*, 112(3), 605-613.

Hatzinikolas, R. (1995), "Temporary Wind Bracing of Masonry Structures," Canadian Masonry Research Institute, Edmonton.

Institute, I. M. (2013), "Internal Bracing Design Guide for Masonry Walls Under Construction."

Jin, Z. and Gambatese, J. (2020), "Exploring the Potential of Technological Innovations for Temporary Structures: A Survey Study", *Journal of Construction Engineering and Management*, 146.

Kanit, R. and Donduren, M. (2010), "Investigation of using ANSYS software in the determination of stress behaviours of masonry walls under out of plane cycling load," *International Journal of the Physical Sciences*, 5(2), 97-108.

Karapitta, L., Mouzakis, H. and Carydis, P. (2010), "Explicit finite-element analysis for the in-plane cyclic behavior of unreinforced masonry structures," *Earthquake Engineering and Structural Dynamics*, 40, 175-193.

Kaushik, H., Rai, D., and Jain, S. (2007), "Stress-Strain Characteristics of Clay Brick Masonry under Uniaxial Compression", *Journal of Materials in Civil Engineering*, 19(9), 728-739.

Koksal, H., Karakoc, C. and Yildirim, H. (2010), "Compression behavior and failure mechanisms of concrete masonry prisms," *Journal of Materials in Civil Engineering*, 17(1), 107-115.

Korkmaz, K., Demir, F. and Sivri, M. (2007), "Earthquake assessment of RC structures with masonry infills walls," *International Journal of Science and Technology*, 2(2), 155-164.

Lang, D. (2005), "Bracing Masonry Walls", Mason Contractors Association of America, <https://www.masoncontractors.org/2005/07/25/bracing-masonry-walls/#newsletter>.

Lumantama, R., Biggs, D. T. and Ingham, J. (2014), “Uniaxial Compressive Strength and Stiffness of Field-Extracted and Laboratory-Constructed Masonry Prisms”, *Journal of Materials in Civil Engineering*, 26(4), 567-575.

Martins, A. P., Pizolato Jr., J. C. and Belini, V. L. (2013), “Image-based method for monitoring of crack opening on masonry and concrete using mobile platform”, *Ibracon Structures and Materials Journal*, 6(3), 414 – 435.

MCAA (2012), “Standard Practice for Bracing Masonry Walls Under Construction”.

Mehrabi, A. and Shing, P. (1997), “Finite element modeling of masonry-infilled RC frames,” *Journal of Structural Engineering*, 123(5), 604-613.

Mohan, A. and Poobal, S. (2018), “Crack detection using image processing: A critical review and analysis”. *Alexandria Engineering Journal*, 57(2), 787 – 798.

Mondal, G. and Jain, S. (2008), “Lateral stiffness of masonry infilled reinforced concrete (RC) frames with central opening,” *Earthquake Spectra*, 24(3), 701-723.

Pereira, F. C. and Pereira, C. E. (2015), “Embedded Image Processing Systems for Automatic Recognition of Cracks using UAVs”, *IFAC-PapersOnLine*, 48(10), 16 – 21.

Rao, V. M. K., Reddy, V. B. and Jagadish, K. (1996), “Flexural bond strength of masonry using various blocks and mortars”, *Materials and Structures*, 29, 119-1124.

Reddy, V. B. and Gupta, A. (2006), “Tensile Bond Strength of Soil-Cement Block Masonry Couplets Using Cement-Soil Mortars”, *Journal of Materials in Civil Engineering*, 18(1), 36-45.

Reddy, V. B., Lal, R. and Rao, N. K. (2007), “Enhancing Bond Strength and Characteristics of Soil-Cement Block Masonry”, *Journal of Materials in Civil Engineering*, 19(2), 164-172.

Reddy, V. B. and Vyas, U. C. (2008), “Influence of shear bond strength on compressive strength and stress-strain characteristics of masonry”, *Materials and Structures*, 41, 1697-1712.

Sankarasrinivasan, S., Balasubramanian, Karthik, K., Chandrasekar, U. and Gupta, R. (2015), “Health Monitoring of Civil Structures with Integrated UAV and Image Processing System”, *Procedia Computer Science*, 54, 508 – 515.

Sarangapani, G., Reddy, V. B. and Jagadish, K. (2005), “Brick-Mortar Bond and Masonry Compressive Strength”, *Journal of Materials in Civil Engineering*, 17(2), 229-237.

Sarhosis, V. and Sheng, Y. (2014), “Identification of material parameters for low bond strength masonry”, *Engineering Structures*, 60, 100-110.

Sayed-Ahmed, E. and Shrive, N. (2010), “Nonlinear finite-element model of hollow masonry,” *Journal of Structural Engineering*, 122(6), 683-690.

Shih, M. H., Tung, S. H., Kuo, J. C. and Sung, W. P. (2006), “The Application of a Digital Image Correlation Method for Crack Observation”, *Proceedings of the Eighth International Conference on Computational Structures Technology*, Stirlingshire, Scotland.

Sirajuddin, M., Potty, N. and Sunil, J. (2011), “Nonlinear seismic analysis of masonry structures,” *Journal of Design and Built Environment*, 9, 1-16.

Sousa, R., Sousa, H. and Guedes, J. (2013), “Diagonal compressive strength of masonry samples – experimental and numerical approach”, *Materials and Structures*, 46, 765-786.

Stavridis, A. and Shing, P. (2010), “Finite-element modeling of nonlinear behaviour of masonry-infilled RC frames,” *Journal of Structural Engineering*, 136(3), 285-296.

Tung, S. H., Shih, M. H. and Sung, W. P. (2008), “Development of digital image correlation method to analyse crack variations of masonry wall”, *Sadhana*, 33(6), 767 – 779.

Varela-Rivera, J., Navarrete-Macias, D., Fernandez-Bqueiro, L. and Moreno, E. (2011), “Out-of-plane behaviour of confined masonry walls,” *Engineering Structures*, 33, 1734-1741.

Vermeltfoort, A., Martens, D. and van Zijl, G. (2007), “Brick-mortar interface effects on masonry under compression”, *Canadian Journal of Civil Engineering*, 34, 1475-1485.

Walker, P. (1999), “Bond Characteristics of Earth Block Masonry”, *Journal of Materials in Civil Engineering*, 11(3), 249-256.

Wang, N., Zhao, X., Zhao, P., Zhang, Y., Zou, Z. and Ou, J. (2019), “Automatic damage detection of historic masonry building based on mobile deep learning”, *Automation in Construction*, 103, 53 – 66.

Zakeri, H., Nejad, F. and Fahimifar, A. (2018), “Image Based Techniques for Crack Detection, Classification and Quantification in Asphalt Pavement: A Review”, *Archives of Computational Methods in Engineering*, 24, 935 – 977.

Zucchini, A. and Lourenco, P. (2009), “A micro-mechanical homogenisation for masonry: Application to shear walls,” *International Journal of Solids and Structures*, 33, 871-886.

2 Experimental Evaluation of Early-age Masonry

Material properties are essential for accurate design calculation to ensure the stability of structures over their design lifespans as well as develop temporary measures to maintain the stability of structures during construction. In this chapter, the linear elastic behavior of early-age masonry prisms is investigated through a detailed experimental program. An overview of sample preparation, testing mechanism, and the experimental procedure is presented first, followed by the evaluation of stress-strain behavior at different early-ages of masonry prisms. Finally, statistical relationships are proposed to establish the variation of different material properties (i.e., modulus of elasticity (E), de-bonding strain (ϵ_d), and de-bonding stress (σ_d)) of masonry prisms with their early ages. These relationships are then used to define the material properties and failure mechanisms of the numerical simulation, as presented in Chapter 3.

2.1 Preparation of Test Specimens

All sample construction and experimental testing were conducted in an outdoor Quonset hut located at the Canadian Masonry Design Centre (CMDC) in Mississauga, Ontario. The masonry block used was a standard 8” Concrete Block Stretcher with a minimum compressive strength of 15 MPa, maximum absorption of 175 kg/m³ and a minimum density of 2000 kg/m³ as per CSA A165.1 (CSA Group 2014) manufactured by Brampton Brick (Brampton Brick 2020). The surface area of each block that was to be bonded was cleaned using a wire brush to ensure the surfaces were clear of any contaminants. To ensure the bonded surface area of the mortar to block remained consistent in specimens, mechanical bonding occurring on the face shells was limited. Depths of 44.45 mm were measured with a leveled ruler on each face shell, and two parallel lines were drawn with a permanent marker. Painters’ tape was applied behind these lines to prevent mechanical bonding occurring on the remainder of the face shell. As such, the bonded surface area of the mortar was kept consistent at 0.0034671 m² for each test to reduce uncertainties in the resulting stresses across various specimens, as shown in Figure 2.1.

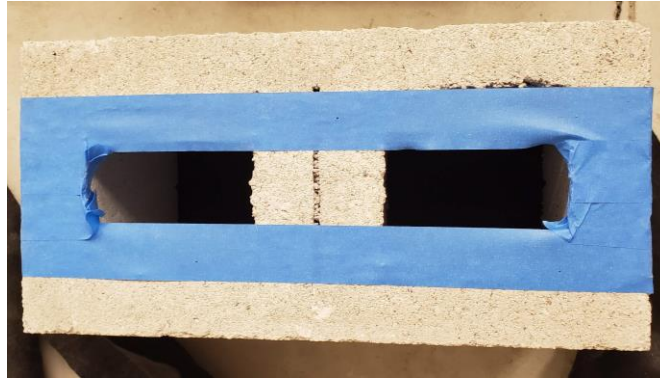


Figure 2.1: Prepared concrete masonry block with painters' tape.

Construction of the masonry assemblages was conducted by a certified mason, as shown in Figure 2.2. The same mason was used for all samples to reduce variability resulting from differences in workmanship between masons. Type S Spec Mix as per CSA-A179-04 (CSA Group 2014) was used as the mortar for all samples. The mortar was mixed with water to the appropriate workability as per CSA-A179-04 (CSA Group 2014) in a Readyman 100 Portable Mortar mixer, as shown in Figure 2.3. The prepared mortar was transferred to a mortarboard and applied to the clean face shells of the concrete block using a trowel. The top block was placed on top of the mortar; a level was used to ensure a perfect horizontal orientation of the samples. A mallet was used to tap the top block into place and ensure the depth of the joint was equal to 10 mm. Finally, a jointer was used to smooth the surfaces of the mortar joint, and the time was recorded on the block to allow for accurate recording of the curing time. Figure 2.4 (a) – (c) depicts the process of constructing the masonry assemblages.



Figure 2.2: A certified mason constructing samples for experimentation.



Figure 2.3: Mechanical mixing of Type S Spec Mix mortar.



(a)



(b)



(c)

Figure 2.4: Preparation of the masonry prism; (a) prepared mortar, (b) applied mortar, (c) finished joint.

Proceeding the first 30 minutes of curing, a surcharge load of 4 additional concrete blocks equivalent to 970 N was placed on each sample, as shown in Figure 2.5. This was done to simulate normal stresses experienced by the mortar on a real construction site while a masonry wall is being constructed. Though the effect of a surcharge load was not extensively studied, 3 unconsolidated and 16-hour consolidated prisms were compared to

the average load required to cause the failure of the sample. It was determined that there was a 27% increase in the load required to cause failure in the consolidated sample when compared to an unconsolidated sample. Additionally, those samples that were unconsolidated were more susceptible to premature failure due to transportation or accidental jarring of the samples before actual experimentation.



Figure 2.5: Finalized construction of a masonry assemblage for testing.

2.2 Proposed Test Setup

An innovative testing mechanism was developed to test two-course masonry prisms under uniaxial tensile loads. The apparatus, as shown in Figure 2.6, consisted of a primary square-shaped steel frame constructed from HSS sections that support two L-shaped brackets connected by steel threaded rods and nuts on either side of the centerline at the base. These brackets and rods secured the bottom block of the masonry assemblages while testing was

conducted, establishing a fixed base condition. Moreover, the top block was supported by two steel plates that were aligned perpendicular to the face shells of the units. To prevent any slippage between the block and plates during the testing, threaded steel rods with nuts on either end ran along the length of the block and through each plate, allowing for the appropriate contact pressure to be established. The plates were connected to a secondary steel frame, which was supported by a bottle jack and load cell used for applying and monitoring the load.

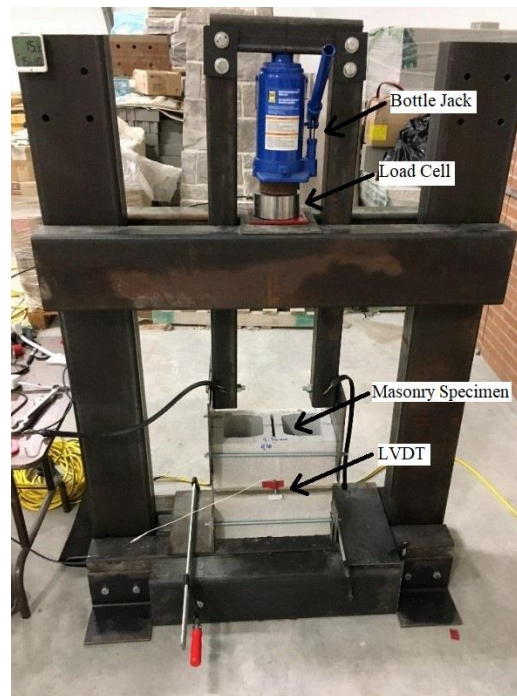


Figure 2.6: Apparatus configuration for uniaxial tensile testing.

2.3 Data Acquisition and Wireless Data Transmission

The load cell monitored the load applied by the bottle jack using the software ‘*OMEGA Digital Transducer Application*’. During testing, the load was monitored continuously with a sampling rate of 8 Hz, and individual tests were exported into readable files. Two linear variable differential transformers (LVDTs) (sensor #1 and #2 on each side, respectively), as shown in Figure 2.7, were used to monitor the displacement at the mortar joints. Each gauge was placed below the mortar joint using double-sided tape such that the probe extended across the depth of the joint. A small metal bracket was attached to the bottom

block below the mortar joint, similarly to act as a surface for the probe to make intact contact. This allows the LVDTs to record the extension of the mortar joint when subjected to the load.



Figure 2.7: Attachment of LVDTs to a two-course masonry prism.

To capture the microscopic displacement expected with the elastic deformation, two high-resolution LVDT packages, and a wireless data acquisition (DAQ) were acquired from *MicroStrain*®, as shown in Figure 2.8. The high-resolution LVDTs (LORD MicroStrain Sensing, 2019) has a maximum linear stroke length of 6 mm with a resolution capable of recording the thousandth of a millimeter and an accuracy of $\pm 2\%$ with linear model calibration. The LVDTs were connected to a low-noise signal conditioner via a 4-pin input cable to ensure high precision and accuracy of the micro displacements. The signal conditioner was connected to an external power source via a 12V DC adapter. The output of the raw voltage readings via an H-BNC to 2-wire connection occurs from the signal conditioner to the wireless data acquisition (DAQ). The two-wire output must be manually hardwired into the single-channel pin connection of the DAQ. Voltage data was transferred from the wireless DAQ to the base station.



(a)



(b)



(c)



(d)

Figure 2.8: Individual components of the displacement sensing and data acquisition system; (a) DAQ, (b) LVDT, (c) signal conditioner, and (d) base station.

The typical setup of the sensing and acquisition equipment is depicted in Figure 2.9, where the components are as follows:

1. Signal conditioner
2. 4-pin input cable
3. LVDTs connecting to masonry prisms

4. H-BNC to 2-pin output cable
5. 12V DC power adapter cable
6. DAQ
7. Base station

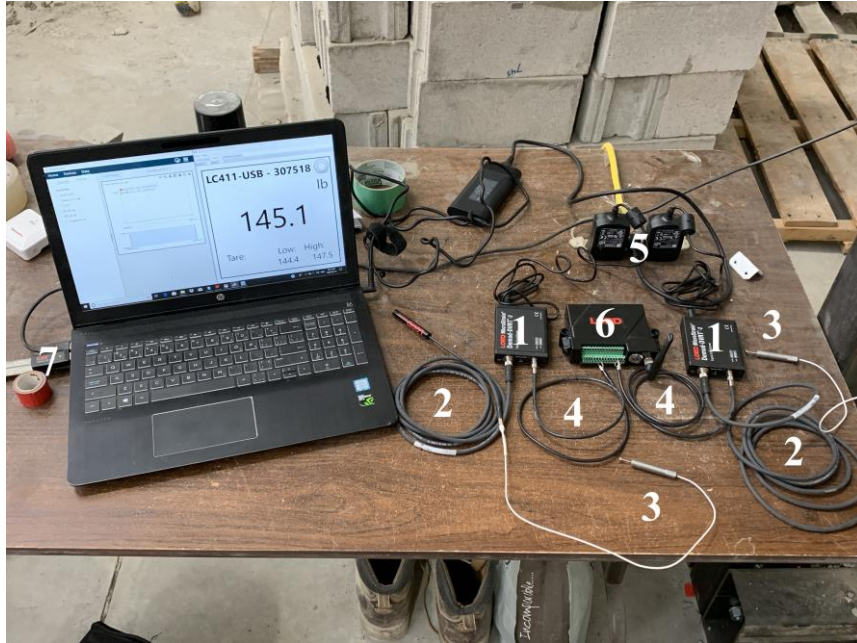


Figure 2.9: A typical data acquisition setup of the LVDT.

2.4 Details of the Experiments

To assess the elastic behavior of early-age masonry prisms at various curing periods, the normal stress and axial strain of the samples were recorded during each test. Moreover, approximately 10 -15 samples were constructed for each curing period as it was anticipated there would be significant variability of elastic strength parameters due to the heterogeneous nature of the material. Due to the susceptibility of premature failure of those samples that had only been cured for 3 to 4 hours, a hand cart was used to transport the samples from the construction site to the testing apparatus. To securely attach the samples, the threaded rods on the bottom brackets and top plates were tightened such that the sample would not move in the transverse or longitudinal directions during testing, as shown in Figure 2.7. The applied load was monitored during the tightening process to ensure that a tensile pressure was not inadvertently applied during the process. As the samples had

already experienced a surcharge load during construction, small compressive pressures applied to the sample were deemed acceptable, and the bottle jack was adjusted to bring the load to balance before testing commenced.

2.4.1 Evaluation of Tensile Stress

For the tensile testing, the weight of the second frame and bottle jack must be accounted for as the load cell recorded not only the load applied by the jack but a portion of the weight of the test setup as well. As such, a set of 1000 data points were recorded by the load cell, and the mean value of those data points was taken as the weight of the frame with no load applied at the start of each testing day. This value was used to normalize the readings during the tests conducted such that the value of the load applied can be determined. Table 2.1 depicts the calibration value used for each day of tensile testing due to the weight of the testing apparatus.

Table 2.1: Mean calibration weight of the test setup for tensile testing.

Test #	1	2	3	4	5	6	7
Mean Apparatus Weight (lbs)	172.1	172.5	172.8	171.7	172.4	171.8	173.2

After completion of the testing, the load vectors contained in the readable files were converted to normal stress vectors through the following equation:

$$\sigma = \frac{4.45(P_i - P_o)}{A_m} \quad (2.1)$$

$$\sigma = \frac{4.45(P_i - P_o)}{34.671 \cdot 10^{-3}}$$

$$\sigma = 128.349P \quad (2.2)$$

Where σ is the normal tensile stress in Pascal (Pa), P_i is the tensile load in lbs, at time step ' i ', P_o is the initial tensile load at the beginning of the test, 4.45 is the conversion factor between force-pounds and newtons and A_m is the surface area of the mortar bonded to the face shell of the blocks equivalent to 0.0034671 m^2 as discussed in Section 2.2.

2.4.2 Evaluation of Uniaxial Tensile Strain

The LVDTs implemented quantified the axial displacements of the masonry prisms under compression and tensile loading. As the ratio between the strength of the block and mortar is significantly high, it is assumed that the significant portion of the deformation occurs in the mortar rather than the blocks themselves. As such, the strain under uniaxial tensile loads can be quantified for a time step in the experiment by the following equation:

$$\varepsilon_{t,i} = \frac{\delta_i - \delta_o}{D_m} \quad (2.3)$$

Where, $\varepsilon_{t,i}$ is the elastic tensile strain at time step “ i ”, δ is the displacement of the assemblage at time step “ i ” in mm, δ_o is the initial displacement of the assemblage at the start of the test and D_m is the depth of the mortar joint; for all samples, this value has been set to 10 mm by the mason.

Voltage acquisition for displacement readings was performed using the commercially available software ‘*SensorConnect*’ (LORD MicroStrain Sensing 2020). The single-input channels on the DAQ were configured to transmit raw voltage data in a range of 0 to 10.24V to the wireless base station. The voltage was acquired continuously at a sampling frequency of 256 Hz as defined by the user, where increased sampling frequencies utilize a greater percentage of the available wireless network. User-defined data ranges were then extracted based on specified periods where testing occurred and saved in readable files. Calibration equations based on a linear model was provided by *LORD MicroStrain*® and was applied to each sensor such that the voltage data can be converted to displacement measurements as follows:

$$\delta_1 = 0.62098V - 3.10136 \quad (2.4)$$

$$\delta_2 = 0.62248V - 3.10932 \quad (2.5)$$

Where δ_1 and δ_2 are the absolute displacements of the LVDTs in mm, and V is the raw voltage data in volts. Once the displacements were known, Equation 2.3 was implemented to convert the displacements to uniaxial strain readings.

2.5 Early-Age Masonry Properties

In this section, the early-age material properties (modulus of elasticity, de-bonding stress, and de-bonding strain) were extracted from the stress-strain curves derived from the experimental data.

2.5.1 Extraction of Stress-Strain Curves

Following the experimentation, the raw displacement and loading data had to be processed to extract the stress-strain curves and E values of the assemblage samples. As previously discussed in Sections 2.3 and 2.4, the displacement data were sampled at a frequency of 256 Hz, while the loading rate was only sampled at a frequency of 8 Hz. Therefore, the final displacement data were resampled at a rate of 8 Hz, such that the displacement and loading vectors are of equal lengths. It was ensured that this technique did not affect the magnitude or distribution of the data, rather the number of points chosen for the analysis. Moreover, as both software for the displacement and loading data require the user to manually start/terminate the recording of data, there was excessive data at the beginning and end of the displacement and loading vectors. This is represented by a series of constant loading and displacement at the beginning of the test, and an abrupt increase in displacement and decrease in loading at the moment of tensile failure is depicted in Figure 2.10.

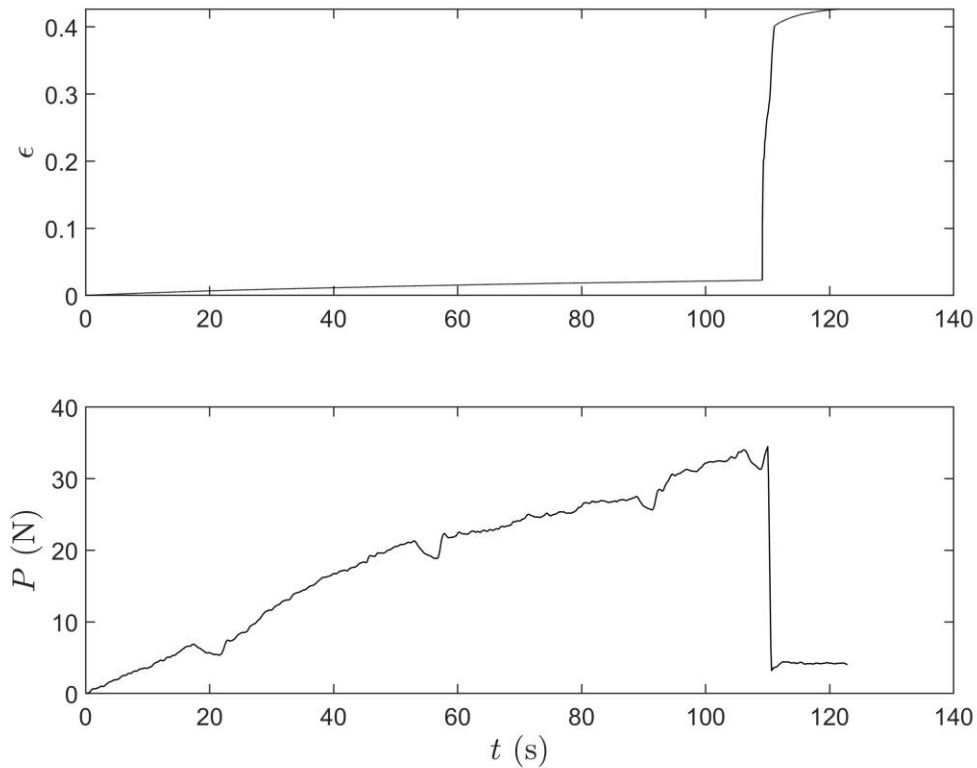


Figure 2.10: Raw strain and applied load.

Therefore, the approximately linear portion of each dataset was extracted to represent the stress-strain behavior that occurred during the uniaxial testing. σ_d and ε_d before the failure of each curve were manually chosen to allow for the synchronization of the linear stress and strain data. These values for σ_d and ε_d were tabulated for all samples to establish statistically significant relationships for curing time, as discussed in Section 2.6. For each sample, two sets of stress-strain data are processed, one for each LVDT attached to the masonry assemblage; the stress vector remains to constrain for both strain readings. The stress-strain curves for each LVDTs were then averaged to obtain the representative variation of the stress-strain behavior for a given sample. Figure 2.11 represents the individual and averaged stress-strain data of each sensor after the post-processing has been completed.

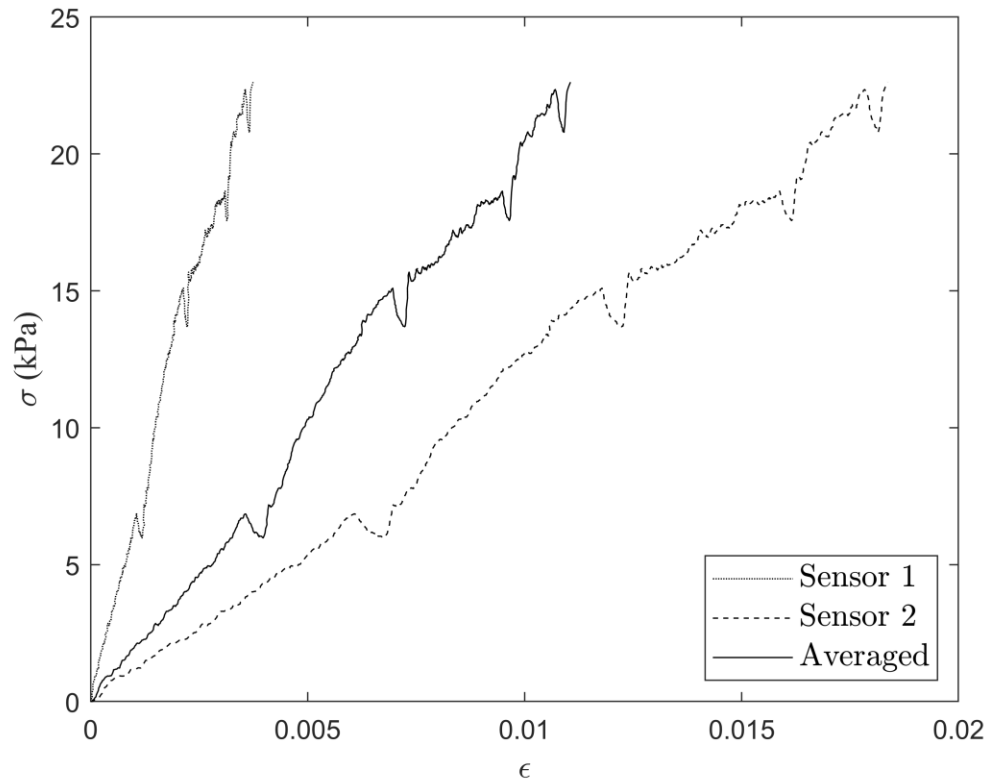


Figure 2.11: Individual and averaged stress-strain curves of a typical test.

In Figure 2.11, several portions of the stress-strain curve show a spontaneous decrease in load as the strain continues to increase. This has been attributed to slippage occurring between the top block of the assemblages and the plates that apply the loading to the sample. As the load increases beyond the confinement pressure applied by the plates due to the tightening of the nuts, the plates begin to slip and move upwards without coming full contact with the top block. This results in a decrease in the applied load; though the strain continues to increase as a portion of the load is still being applied to the sample. Due to the rough surface of the masonry block, eventually, the slippage is reversed as the plates regain full contact due to the friction between the plates and the blocks; therefore, the load begins to increase again gradually. Moreover, there were those samples where the plates disengaged completely from the block resulting in a ‘rigid’ shift of the stress-strain curves, as shown in Figure 2.12. As such, these samples were not included in the statistical analysis of the sample population. To address these challenges, the plates were optimally tightened

such that the confinement pressure prevents significant slippage, however not significant enough to apply tensile stress to the sample before testing begins. Approximately 30% of constructed samples were lost due to premature failure of samples before experimentation or poor data results, as depicted in Figure 2.12.

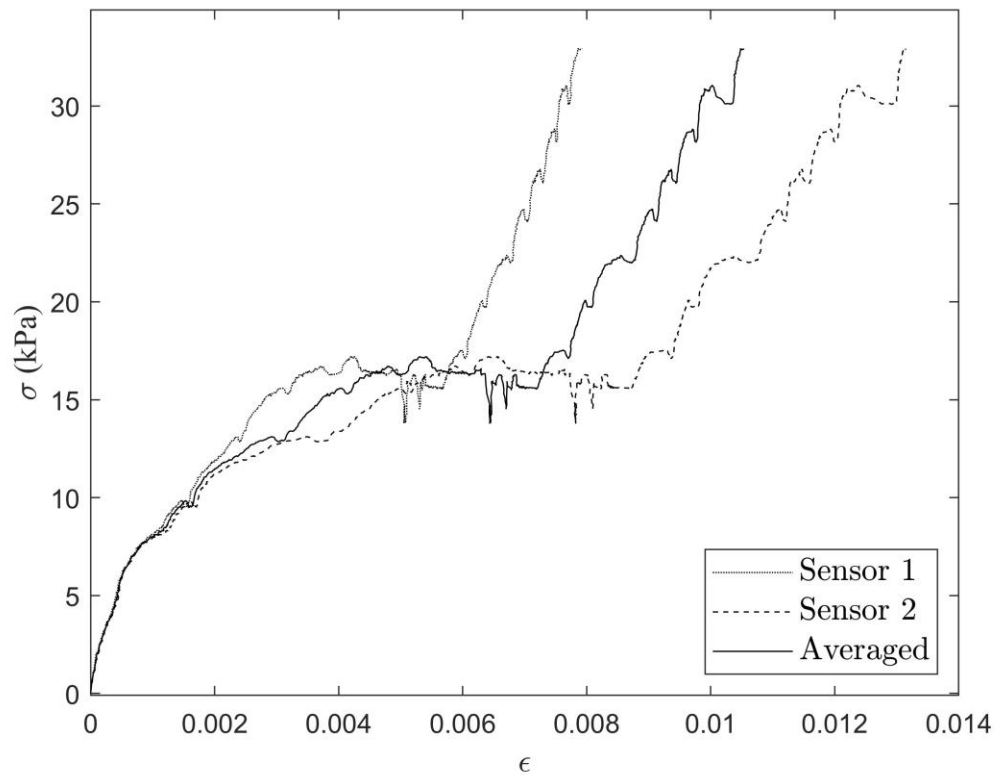


Figure 2.12: Rigid shift of the stress-strain curve.

2.5.2 Modulus of Elasticity of Early-age Masonry

From experimentation, it was observed that the early-age masonry prisms behaved in a completely elastic manner under tensile loading. From Figure 2.11, it can be observed that the stress-strain curves extracted from experimentation show an almost completely linear trend. Therefore, neither the concrete masonry blocks nor the mortar experience significant enough stress to exceed the individual yield stress of the materials and development of plastic behavior. Though the mortar has significantly reduced strength due to length of curing time, the mechanism by which the assemblage fails is due to the de-bonding of the

mortar from the block, not the failure of the mortar itself. Once the debonding stress of the masonry prism was reached, there was significant delamination observed between the mortar from the surface of the masonry block resulting in a de-bonding failure of assemblage as depicted in Figure 2.13. As such, due to the failure of the bond before the failure of the material, the behavior of the prism remains in the linear portion of the stress-strain curve.



Figure 2.13: Typical de-bonding failure of early-age masonry.

Therefore, proceeding the extraction of the stress-strain curves from the experimental data, E value was determined for each sample. E value is defined as a material's resistance to elastic deformations due to the application of stress. For a completely elastic material; where the deformation rebounds after the load is no longer applied, E value can be represented by Hooke's Law of Elasticity:

$$\sigma = E\epsilon \quad (2.6)$$

Where σ is the stress in Pa, ε is the strain, and E is the modulus of elasticity. Therefore, the slope of the stress-strain curve is representative of the E value. Moreover, when the assemblage is in a zero-stress state, no deformation occurred. As such, a zero-intercept linear regression model (Seltman 2018), was implemented to determine E value.

For an independent vector, Y_i and dependent vector, X_i the equation of a zero-intercept linear regression model is as follows (Othman 2014):

$$\hat{Y}_i = BX_i + e_i \quad (2.7)$$

Where, \hat{Y}_i is the prediction of the dependent variable, X_i is the independent variable, B is the regression parameter representing the slope of the line, and e_i is the value associated with the random error. Using the method of least squares, B can be estimated using the Y_i and X_i with the following equation (Othman 2014):

$$B = \frac{\sum_{i=1}^n X_i Y_i}{\sum_{i=1}^n X_i^2} \quad (2.8)$$

To qualify the fit of the linear model on the experimental data, the Coefficient of Determination (R^2) was determined for each model. The following equation represents the R^2 value for a zero-intercept model (Naomi Altman 2015):

$$R^2 = 1 - \frac{SSR}{SST} = 1 - \frac{SSR}{SSE + SSR} \quad (2.9)$$

Where SST is the sum of the total errors as shown in Equation 2.9. SSR is the sum of the squared residuals, and SSE is the sum of the squared errors as calculated by the following equations, respectively:

$$SSE = \sum_{i=1}^n (Y_i - \hat{Y}_i)^2 \quad (2.10)$$

$$SSR = \sum_{i=1}^n (\hat{Y}_i - Y^*)^2 \quad (2.11)$$

Where, Y^* is the mean value of the real independent variable, Y_i . Based on Equations 2.7 – 2.11, E value and their respective R^2 values were calculated for each of the early-age samples. Table 2.2 summarizes the regression parameters calculated to attain the zero-intercept linear model for the average data, as plotted in Figure 2.11. The zero-intercept linear regression model is plotted against the experimental data, as depicted in Figure 2.14.

Table 2.2 Summarization of regression parameters for a 3-hour sample.

Regression Parameter	B_1	SSR	SSE	SST	R^2
Value	$2.019 \cdot 10^6$	$3.736 \cdot 10^{10}$	$4.188 \cdot 10^8$	$3.777 \cdot 10^{10}$	0.99

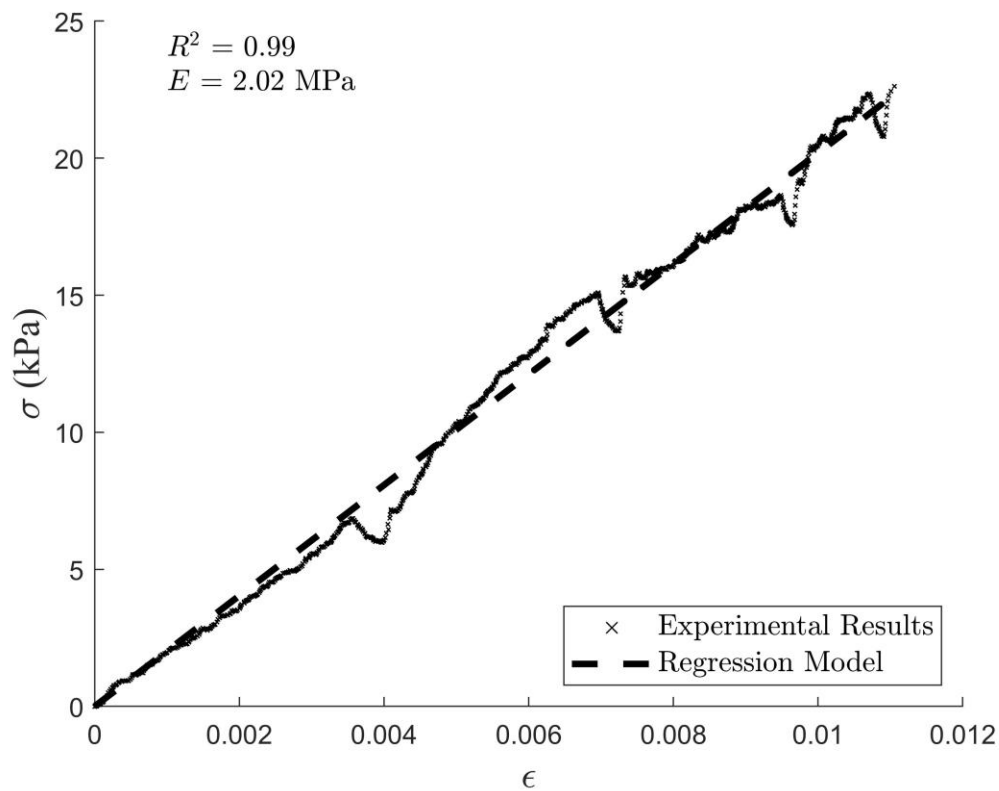


Figure 2.14: Comparison of the linear regression model and experimental data.

For material testing of masonry constituents, a certain degree of variability is expected across those samples that comprise a given population of data. In this instance, those samples that have similar curing times are expected to have varying E values, σ_d , and ϵ_d .

As strength parameters are used in design equations, the amount of variation in these values must be quantified. Therefore, the coefficient of variation (COV) is used to represent the variation of the strength parameters; the higher the percentage, the more variable the quantity is:

$$COV = \frac{\bar{\sigma}}{\mu} \quad (2.12)$$

Where μ is the mean value of all samples within a given curing period for E , peak strain and peak stress and $\bar{\sigma}$ is the corresponding standard deviation for E , σ_d , and ε_d .

2.5.3 Summary of Strength Parameters for Early-age Masonry

Appendix A.1 – A.9 summarizes the results of the debonding stress and strain recording during the experimental testing. Furthermore, E values quantified by the zero-intercept linear regression model are presented along with the corresponding R^2 value. The average and COV of the strength parameters are recorded to depict the variability of the samples within a given population based on the curing period recorded at the time of testing. From the following tables, it can be observed that there is a significant amount of variability in the elastic behavior, particularly maximum strain, even though the curing period varied minimally between samples of the same population. There were several factors noted about the environment, sample preparation, and testing procedure that could have attributed to the variability of the results:

1. Testing was conducted in an outdoor facility throughout the year; the temperature and humidity that the samples were exposed to could only be controlled to an extent. In the winter, the facility would be heated to 16°C with a relative humidity of 40 – 50%, while in the summer temperatures could reach 30°C with a relative humidity of 75 – 85%. Previous research on the effect of curing temperature and relative humidity has concluded that high-temperature environments may lead to higher early-age but diminished long-term compressive strength (Wajahat 1991), while low relative humidity can greatly decrease the flexural strength of mortars (Baradan 2011). Moreover, the initial absorption rate of the block is influenced by

relative humidity; both initial absorption rate and water flow reversals have been shown to influence bond strength (Groot 1999; Kaushik 2007).

2. The same concrete blocks were reused for various samples over the extent of the experimentation. Even though they were cleaned off using wire brushes, there is a possibility that the microscopic pores of the concrete block were previously filled, reducing mechanical interlocking between mortar and concrete block, leading to reduced bond strength. Similarly, the act of brushing the blocks may have decreased the surface roughness compounding the effect of decreasing the bond strength.
3. In some samples, it was noted that the upper frame did not remain plumb during the entirety of the experiment. Often that frame had to be readjusted such that it was at a perfect 90° to the block. Slight variations in the orientation of the frame may have applied flexural stresses to the masonry assemblage, rather than uniaxial tensile stresses, resulting in variation in results. As such, Section 2.6 demonstrates how various statistical methods were used to enhance the data such that the variability of the results could be reduced, and a correlation between elastic strength parameters and curing period could be established.
4. An assumption was made that the mortar depth was kept at 10 mm for each sample by the mason. If there were fluctuations with the depth of the mortar, the calculated strain would have errors associated with its value. Additionally, the E values would be affected.
5. Slippages of the confinement plates during loading lead to an abrupt decrease in the load, as shown in Figure 2.11. These spikes in the data could reduce the linearity of the applied load resulting in the least significant linear correlation when fitted with the model to determine E .

2.6 Outlier Analysis

As discussed in Section 2.5.3. many environmental and mechanical factors contribute to the variability of the strength parameters quantified through experimentation. Therefore, to establish a meaningful correlation between curing time and strength parameters the data must be organized such that (1) the variability of the data decreases, (2) the individual samples within the data have good correlations with each other, (3) the overall sample sizes

are not greatly affected by the statistical enhancement. As such, methodologies were investigated for statistically enhancing the data obtained from the experiments and mathematical modeling. Outlier analysis is implemented employing the use of the Interquartile Range Technique (IQRT) to remove those datasets whose values fall outside a defined range. IQRT was conducted on E values, σ_d , and ε_d .

An outlier of a dataset may be defined as a value that falls outside the acceptable range of values. In statistics, one popular method to determine those points that fall outside of an acceptable range for a given dataset is the IQRT (Vinutha 2018). For a given independent dataset Y with N samples, the first quartile ($Q1$) and third quartile ($Q3$) can be determined. If $0.25N$ and $0.75N$ are both whole numbers, then $Q1$ and $Q3$ are equal to:

$$Q_1 = Y(0.25N) \quad (2.13)$$

$$Q_3 = Y(0.75N) \quad (2.14)$$

If this condition is not met, then $Q1$ and $Q3$ are equal to:

$$Q_1 = \frac{Y(\text{rounded down}(0.25N)) + Y(\text{rounded up}(0.25N))}{2} \quad (2.15)$$

$$Q_3 = \frac{Y(\text{rounded down}(0.75N)) + Y(\text{rounded up}(0.75N))}{2} \quad (2.16)$$

The interquartile range is defined as:

$$IQR = Q_3 - Q_1 \quad (2.17)$$

Therefore, those ranges of values of Y that are defined as ‘Weak’ or ‘Strong’ outliers are as follows:

Weak Outliers

$$Y < Q_1 - 1.5IQR \mid Y > Q_3 + 1.5IQR \quad (2.17)$$

Strong Outliers

$$Y < Q_1 - 3.0IQR \mid Y > Q_3 + 3.0IQR \quad (2.18)$$

A MATLAB script was created to generate a figure to show the IQRT for E values, σ_d , and ε_d of each prism. Figure 2.15 depicts an example of the figure generated for the debonding stress of a 3-hour sample.

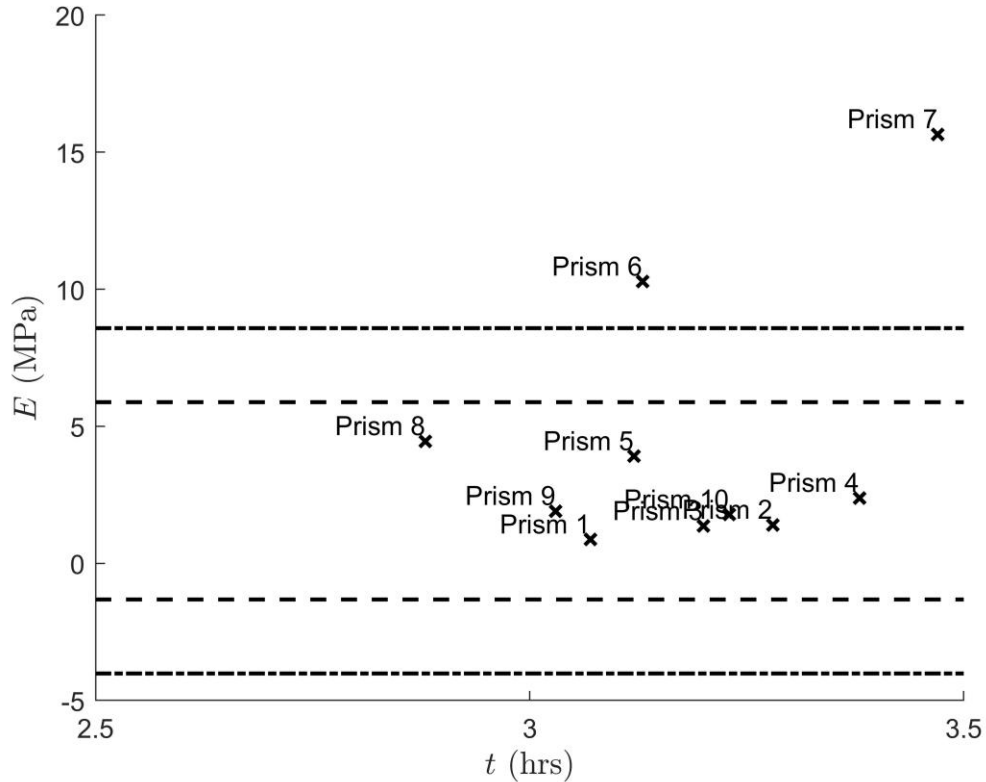


Figure 2.15: IQRT of the peak strain of a 4-hour dataset.

The dashed line represents the upper and lower boundaries for the weak outliers, while the dotted dashed lines represent the upper and lower boundaries for the strong outliers. As such, for this example, prism 6 and 7 would be considered strong outliers for E for the 3-hour dataset. Similarly, this technique was used for all curing periods for σ_d values. Once all outliers were removed, the COV was recalculated to determine the impact of this technique on the variability of the experimental results. Table 2.3 shows the summary of the COV data from the IQRT for all curing periods for E and σ_d for N samples. The μ of the samples was tabulated with the COV values in brackets.

Table 2.3: Summarization of the effect of IQRT on parameter COV.

Curing Period (Hrs)	IQRT	σ_d (kPa)		E (MPa)	
		μ (COV)	N	μ (COV)	N
3	None	13.0 (21.6%)	10	4.40 (109.6%)	10
	Yes	13.0 (21.6%)	10	2.26 (56.4%)	8
4	None	13.8 (29.2%)	11	2.77 (50.2%)	11
	Yes	13.8 (29.2%)	11	2.83 (17.5%)	7
6	None	19.6 (38.6%)	7	3.27 (53.7%)	7
	Yes	19.6 (38.6%)	7	3.27 (53.7%)	7
7	None	18.4 (34.1%)	10	6.57 (63.0%)	10
	Yes	18.4 (34.1%)	10	6.88 (45.3%)	7
13	None	33.7 (14.1%)	7	7.53 (52.9%)	7
	Yes	34.3 (6.3%)	5	7.53 (52.9%)	7
18	None	37.1 (30.8%)	14	11.53 (66.4%)	14
	Yes	32.0 (14.1%)	11	9.89 (10.9%)	9
24	None	40.4 (16.4%)	10	5.98 (40.6%)	10
	Yes	40.4 (16.4%)	10	6.10 (9.0%)	3
48	None	43.6 (27.8%)	11	12.26 (74.8%)	11
	Yes	43.6 (27.8%)	11	6.49 (41.9%)	7
72	None	51.6 (28.5%)	12	9.47 (67.6%)	12
	Yes	51.6 (28.5%)	12	8.14 (57.3%)	11

On average, the variability of the samples across all ages decreased by 18% due to the outlier analysis. The removal of these outliers greatly decreased the variability of the strength parameters for some ages, as much as a 50% reduction in several cases. However, this technique decimates the number of samples used to determine a representative value for the parameter. Overall, those datasets that used IQRT to improve the dataset variability had a loss of 20% on average of the samples contained. Therefore, though this method greatly improved the variability of sample datasets, increased sampling would allow the sample number to stabilize, increasing the confidence that the average value of the samples is representative of the real elastic strength parameters.

2.6.1 Correlation Between Material Properties and Curing Times

Proceeding the dataset enhancement conducted in Section 2.6, a correlation was established between E values and σ_d , with respect to the curing time. The remaining individual strength

parameters are grouped in their respective dataset based on their associated curing times; +/- 30 minutes from the whole hour. The grouped strength parameters with their variation were plotted against curing time to observe and discernable trends in the data, showing the distributions of the individual and grouped samples of E and peak stress with respect to the curing period.

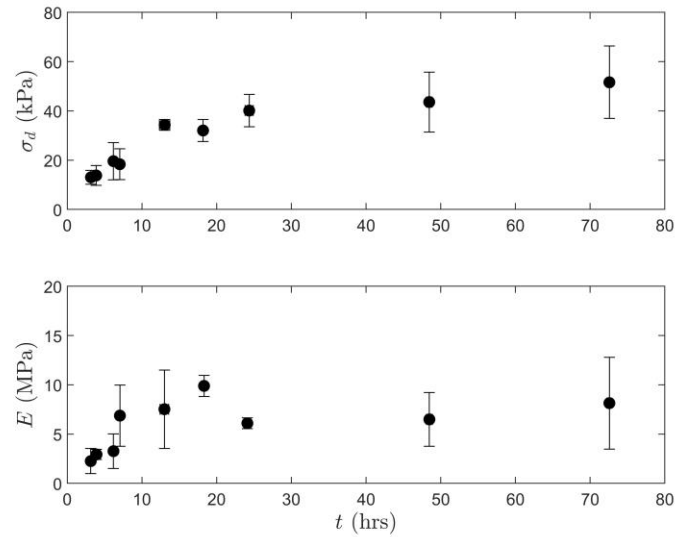


Figure 2.16: Variation of E and σ_d with the curing period.

From Figure 2.16, it can be observed that the distribution of the data has a pseudo-logarithmic trend. Therefore, nonlinear regression was performed on the grouped data points, assuming a natural logarithmic model for the regression function. The following equations represent the variation of E values and σ_d with respect to the curing period.

$$\sigma_d = 12.6 \ln(t) - 2.7 \quad (2.19)$$

$$E = 1.72 \ln(t) + 1.47 \quad (2.20)$$

Where σ_d is the de-bonding stress at the point of failure for the masonry assemblage in (kPa), and t is the curing period in (Hrs). R^2 value for Equations 2.19 and 2.20 are 0.96 and 0.51, respectively, suggesting a reasonable correlation between bond strength and curing

period. However, the E value shows a slightly weaker correlation for the curing period. In Section 2.5.3, the details were given about possible environmental, mechanical, and material factors that could have contributed to the increased variability of the E value.

The preceding equations only represent the median of all the individual data points. From a design standpoint, these equations would not be representative of the behavior of early-age masonry structures. As such, a safety factor of 0.6 has been applied to equations to account for the material variability and to ensure that these equations are representative of the material behavior to a high level of confidence. These variabilities could be further reduced through increased sample testing and more stringent testing methods based on the variables highlighted in Section 2.5.3. The proposed equations are, therefore, as follows:

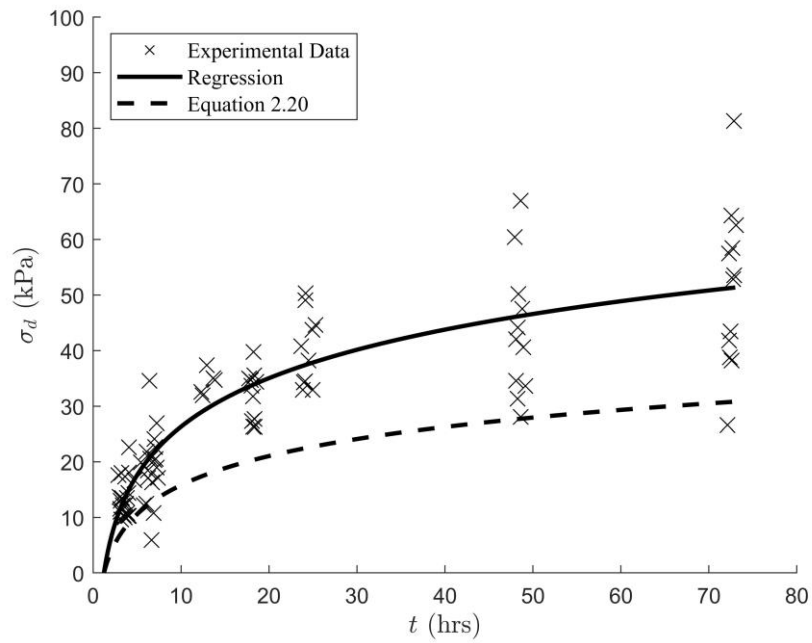
$$\sigma_d = 0.6(12.6 \ln(t) - 2.7)$$

$$\sigma_d = 7.56 \ln(t) - 1.62 \quad (2.20)$$

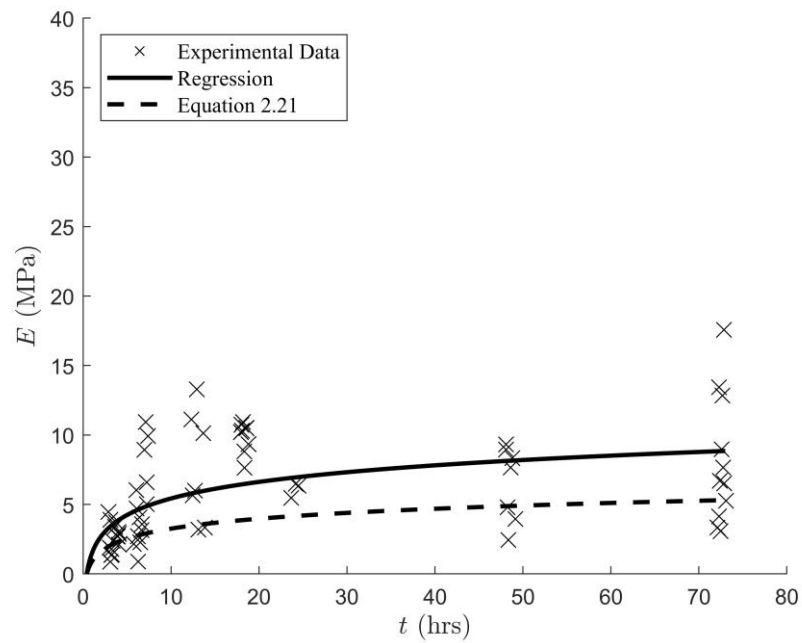
$$E = 0.6(1.72 \ln(t) + 1.47)$$

$$E = 1.03 \ln(t) + 0.88 \quad (2.21)$$

Figure 2.17 (a) – (b) demonstrates that the equations 2.20 and 2.21 are representative of a statistically significant portion of the data collected during experimentation.



(a)



(b)

Figure 2.17: The proposed equation for variation of (a) debonding stress and (b) E with the curing period.

2.7 Conclusions

This chapter summarized the experimental process used to investigate the linear elastic behavior of early-age masonry constituents. Sample preparation, the testing apparatus, and the experimental protocol were presented. Experimental data are fitted using a zero-intercept linear regression model to determine E at various curing periods. A detailed explanation of variables contributing to the significant scatter of the experimental data was summarized. Outlier analysis using IQRT was shown to effectively decrease the data variance but affecting the sample size of different curing periods. Additional experimental samples would need to be conducted to decrease the variability of peak strain with respect to the curing period. Lastly, nonlinear relationships are proposed for the variation of E values and σ_d to curing time with the addition of a safety factor to account for material and testing variability. Further testing in the future could reduce the variability and assist in establishing a more statistically significant trend. Furthermore, these equations are the only representative of the behavior of material that constitutes the mortar and block as defined in Section 2.1, for curing periods between 3 to 72 hours. These relationships are used in the following chapter to define the material properties and failure mechanisms of the numerical simulation in Chapter 3.

2.8 References

- Baradan, H. U. (2011). The effect of curing temperature and relative humidity on the strength development of Portland cement mortar. *Scientific Research and Essays*, 6(12), 2504-2511.
- Brampton Brick. (2020). *Standard and Lightweight Block*. Retrieved from Brampton Brick: <https://bramptonbrick.com/products/block/standard-and-lightweight>
- CSA Group. (2014). *CAN/CSA-A179-14*. CSA Group.
- CSA Group. (2014). *CSA A165 Series-14 (R2019) (5th ed.)*. CSA Group.
- Groot, C. (1999). The influence of water flow (reversal) on bond strength development in young masonry. *HERON*, 44(2), 63-78.

Kaushik, H. (2007). Stress-Strain Characteristics of Clay Brick Masonry under Uniaxial Compression. *Journal of Materials in Civil Engineering*, 19(9), 728 - 739.

LORD MicroStrain Sensing. (2019). *DEMODO-DVRT-2 Displacement Sensor Signal Conditioner*. Retrieved from LORD Sensing DATASHEET:

https://www.microstrain.com/sites/default/files/demod-dvrt2_ds_c_8400-0086.pdf

LORD MicroStrain Sensing. (2019). *LORD Sensing DATASHEET*. Retrieved from V-Link-200 Wireless 8 Channel Analog Input Sensor Node:

https://www.microstrain.com/sites/default/files/applications/files/v-link_200_datasheet_8400-0097_rev_j.pdf

LORD MicroStrain Sensing. (2019). *SG-LVDT Subminiature Gauging Displacement Sensor*. Retrieved from Lord Sensing DATASHEET:

https://www.microstrain.com/sites/default/files/sg-lvdt_series_datasheet_8400-0112_rev_b_0.pdf

LORD MicroStrain Sensing. (2020). *LORD MicroStrain Sensing*. Retrieved from SensorConnect: <https://www.microstrain.com/software/sensorconnect>

Naomi Altman, M. (2015). Simple Linear Regression. *Nature Methods*, 12, 999-1000.

Othman, S. (2014). Comparison between Models With and Without Intercept. *General Math Notes*, 21(1), 118-127.

Seltman, H. (2018). *Experimental Design and Analysis*. Carnegie Mellon University, 2018 [Online]. Available: <http://www.stat.cmu.edu/~hseltman/309/Book/Book.pdf>

Vinutha, H. (2018). Detection of Outliers Using Interquartile Range Technique from Intrusion Dataset. *Advances in Intelligent Systems and Computing*. 701. Singapore: Springer.

3 Finite Element Study of Early-age Masonry

Numerical models such as finite element models allow rapid, accurate, and iterative design processes for the engineering structures. Though extensive experimental studies were conducted in Chapter 2, there were many curing periods for which the uniaxial stress-strain behavior of two-course early-age masonry assemblages were not studied. As such, the material models and subsequent correlations as demonstrated by Equations 2.20 and 2.21 developed can be applied to numerical models to study the stress-strain behavior of early-age masonry for samples that fall in an untested interval; for example, those cured at 10 hours. Furthermore, developing accurate modelling techniques allow for inexpensive parametric studies to be conducted on early-age masonry structures with varying material and geometric properties.

In this chapter, ABAQUS was used to simulate a two-course masonry block prism as used in the experiments conducted in Chapter 2. Details are provided about the development of the material models that were used in the rendering of a 3D solid model. Various methods were implemented in the pre-processing stages to improve the overall accuracy with respect to the experimental results. Numerical and experimental results were compared to assess the robustness of the proposed modeling technique. Finally, a case study is conducted to evaluate current early-age design practices with the evaluated experimental results under wind loading. These models will be implemented in future full-scale parametric studies of early-age masonry walls, which will allow for accurate simulation while avoiding time-intensive experimentations.

3.1 Model Parameters of the Masonry Prism

To develop an accurate numerical model, extensive experimental studies were conducted on early-age masonry assemblages to extract material properties. In this chapter, the strength parameters and failure criteria of early-age masonry were applied to a 3D solid finite element model (FEM) developed in ABAQUS. The material properties for this model were estimated and designed based on the experimental results, as summarized in Chapter

2. A significant number of preliminary FEM models were investigated in a parametric study to determine the most accurate modeling techniques and parameters. The density (ρ), Poisson's ratio (ν), and E values were implemented to define the strength behavior of the concrete masonry blocks and mortar. As mentioned in Section 2.1, the minimum density of the concrete blocks was 2000 kg/m^3 ; therefore, this value was used to represent ρ for the concrete block. Furthermore, the same value is used to represent the ρ of the mortar. The ν of the concrete masonry block and mortar is assumed to be 0.25. From Equation 2.20 and 2.21, the σ_d and E value calculated from the experimental data can be quantified for each curing period. Table 3.1 represents the σ_d and E values estimated through the experimental study for different curing periods.

Table 3.1: Variation of σ_d and E with the curing period.

Curing period (Hrs)	3	4	6	7	13	18	24	48	72
E (MPa)	2.01	2.31	2.73	2.88	3.52	3.86	4.15	4.87	5.28
σ_d (kPa)	6.69	8.86	11.93	13.09	17.77	20.43	22.41	27.65	30.71

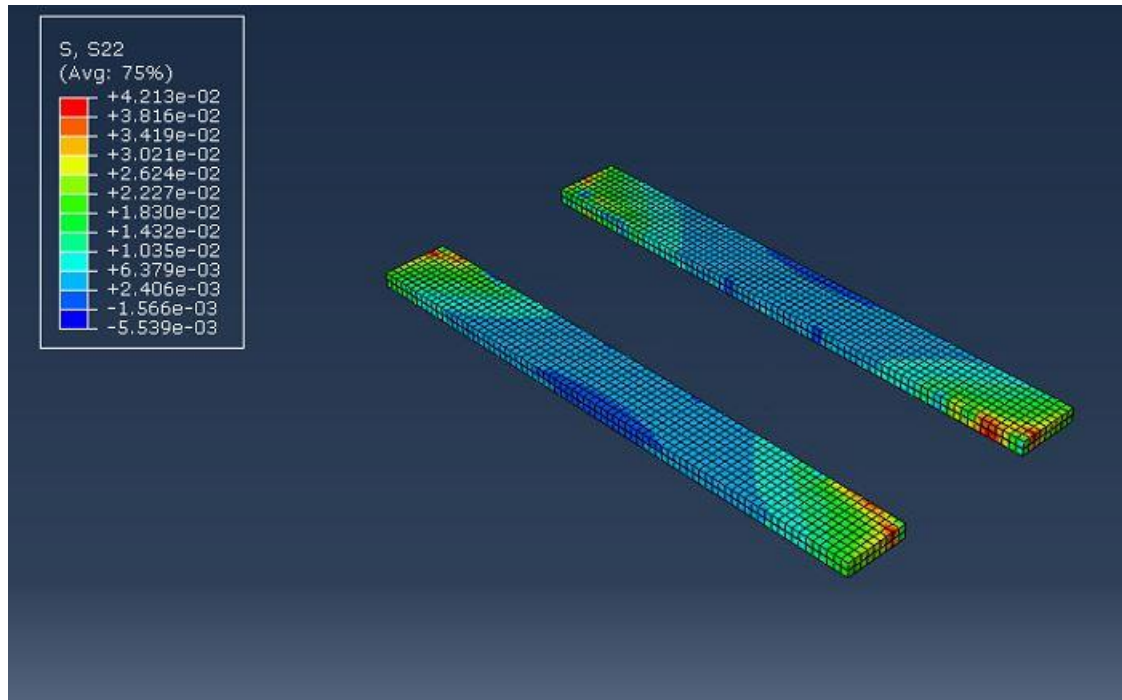


Figure 3.1: Stress concentration of the simulated mortar.

3.1.1 FEM of the Mortar

For the masonry blocks, E values defined in the model were assumed to equal to those provided in Table 3.1 for a given curing period. However, for the mortar, the E values defined in the model was assumed to be equivalent to 0.87 times the values presented in Table 3.1. Berlo (2009) concluded that increasing the modulus ratio of two separate materials greater than 1 (surface stiffening effect) reduced the maximum stress concentration under the load. This reduction of stiffness in the mortar was to mitigate the development of stress concentrations. For this model, Figure 3.1 shows the localization of the stress concentrations that occurred at the corners of the mortar due to high-stress gradients. High-stress gradients occur in FEM models where rapid changes in the cross-sectional area occur, such as holes or sharp corners, creating stress concentrations and, therefore, higher stress (Hodhigere, 2018). This results in higher average stresses across the mortar in the FEM when compared to those obtained through experimentation. A stress

concentration factor (K_t) can be calculated to quantify the magnification of stress at a location when compared to the nominal stress (Hodhigere, 2018):

$$K_t = \frac{\sigma_{max}}{\sigma_n} \quad (3.1)$$

Where σ_{max} is the maximum normal stress in MPa in the mortar of the FEM due to the application of the load for a given time step in the simulation and σ_n is the nominal stress in MPa which is assumed to be the average stress in the mortar of the FEM due to the application of the load for a given time step in the simulation. The average stress concentration was taken across the steady-state variation of the stress concentration, as shown in Figure 3.2. The stress concentration factor fluctuates drastically when failure of the mortar-block interface has occurred; otherwise, it remains stable throughout the simulation. Table 3.2 shows the stress concentrations for the various curing periods that were simulated in ABAQUS:

Table 3.2: Variation of stress concentration factor with the curing period.

Curing Period (Hrs)	3	4	6	7	13	18	24	48	72
K_t	4.69	4.69	4.69	4.6	4.69	4.69	4.69	4.69	4.69

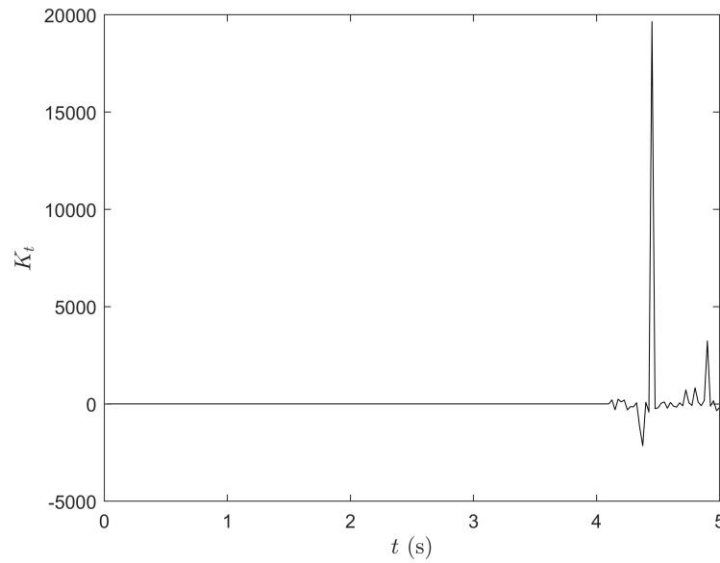


Figure 3.2: Variation of stress concentration factor over the simulation period.

Therefore, the stress concentration factor was taken as 4.69 for all models as there was no variation in the stress concentration factor with different early-ages (i.e., curing periods). Table 3.3 provides the material model inputs used in ABAQUS for a 3-hour curing period. The model was developed using units of N, kg, and mm; as such, the values in the table have been adjusted to reflect these units. Appendix B.1 – B.8 summarizes the strength parameters for the remaining curing periods.

Table 3.3: Strength parameters of a 3-hour cured sample in ABAQUS.

Parameter	Concrete Masonry Unit (CMU)	Type S Mortar 3-Hours Cured
ρ (ton/mm ³)	2.00e-09	2.00e-09
ν	0.25	0.25
E (MPa)	2.01	1.75

To define the debonding failure pattern experienced by early-age masonry under uniaxial tensile load, cohesion-based contact elements with defined damage initiation and evolution criteria were created. Previous modeling techniques have used cohesion-based contact elements for the mesoscopic simulation of 3D cyclic loads of unreinforced masonry structures (Aref, 2013). Moreover, these interface elements have been used to create a micro model of partially grouted masonry assemblages (Bolhassani, 2015). These elements

allow surfaces to be defined by a general traction-separation law where the damage initiation criteria have not been met, and the traction will continue between the two surfaces. For a linear elastic behavior, the traction-separation behavior is defined by the following matrix (Dassault Systemes Simulia Corp, 2011):

$$t = \begin{Bmatrix} t_n \\ t_s \\ t_t \end{Bmatrix} = \begin{bmatrix} K_{nn} & K_{ns} & K_{nt} \\ K_{ns} & K_{ss} & K_{st} \\ K_{nt} & K_{st} & K_{tt} \end{bmatrix} \begin{Bmatrix} \delta_n \\ \delta_s \\ \delta_t \end{Bmatrix} = K \delta \quad (3.1)$$

Where t is the traction stress vector containing elements t_n , t_s , and t_t , which represent the traction stress in the normal, longitudinal shear and transverse shear directions, respectively, in MPa. K is the traction stiffness vector where K_{nn} , K_{ss} , and K_{tt} represent the uncoupled traction stiffnesses in the normal, longitudinal shear and transverse shear directions in N/mm³. K_{ns} , K_{nt} , and K_{st} represent the coupled traction stiffness elements. However, these elements are zero-elements due to the uncoupled nature of the pure normal separation experienced in uniaxial tensile loads. Lastly, δ is the separation vector where δ_n , δ_s , and δ_t are the separations in the normal, longitudinal, and transverse directions in mm. Based on the definition provided for Equation 3.1, the K_{nn} of the experimental data can be calculated from the following equation:

$$K_{nn} = \frac{P_f}{A_m * \varepsilon_d} = \frac{E}{D_m} \quad (3.2)$$

Where P_f is the load at failure in N and D_m is the depth of mortar, which was assumed to be 10 mm for all samples as dictated by the mason. For this model, it is assumed that $K_{nn} = K_{ss} = K_{tt}$ as no experimentation has been conducted on the shear behavior of early age masonry. This assumption is justified as the model has defined only the behavior of the uniaxial normal stresses; therefore, shear stress will not contribute to the behavior and failure pattern of this simulation. The damage initiation at the moment the mortar-block interface fails is defined using a maximum stress criterion such that (Dassault Systemes Simulia Corp, 2011):

$$\max \left\{ \frac{\langle t_n \rangle}{t_n^o}, \frac{\langle t_s \rangle}{t_s^o}, \frac{\langle t_t \rangle}{t_t^o} \right\} = 1 \quad (3.3)$$

Where t_n^o , t_s^o , and t_t^o are the peak values of the traction stress in the normal, longitudinal, and transverse shear directions along which the initial damage occurs and begins to separate. Likewise, the maximum traction stress for all three categories is assumed to be equivalent. Ideally, the t_n^o is assumed to be the recorded stress at the time of failure during the experiments. However, through preliminary modeling, it was found that assuming the maximum normal stress was equal to the debonding stress resulted in a model that failed at a substantially lower load. Similarly, assuming the product of the stress concentration and debonding stress to be equivalent to the maximum normal stress results in a model that fails at higher stress than recorded experimentally. This occurs due to the fact that at the maximum stress concentration value, only a few elements meet the requirements of damage initiation, which does not result in a complete failure of the mortar-block interface. By reducing the stress concentration slightly, more elements meet the proposed damage initiation, and therefore the surface debonding occurs as observed during experimentation. Therefore, t_n^o can be calculated using the proposed equation:

$$t_n^o = \varphi K_t \sigma_d \quad (3.4)$$

Where φ is a reduction factor applied obtained from hyper tuning t_n^o such that the error between the load applied, σ_d , ε_d , and E values are optimized to obtain a minimal error. It was determined through model hyper tuning that a value of φ equivalent to 0.95 provided the most accurate results. Therefore, it can be concluded that stress concentration factors have a significant impact on the accuracy of defining the damage initiation criteria for this model. For damage evolution, a displacement-based failure with linear softening was chosen. From the experiments, it was observed that the failure was instantaneous, and therefore the displacement of the sample after damage initiation has occurred can be assumed to be zero. However, defining the total/plastic displacement after damage initiation to be zero in ABAQUS creates convergence issues within the software, which may lead to inaccurate solutions. As such, a significantly small displacement can be used to represent the zero plastic displacement state; a value of 0.00001 mm was chosen for this model. Table 3.4 provides the material model for the cohesion-based contact elements used for a 3-hour curing period. The model was developed using units of N, kg, and mm; as such the values in the table have been adjusted to reflect these units. Appendix C.1 – C.8

summarizes the material model for cohesion-based contact elements for the remaining curing periods.

Table 3.4: Material model for cohesion-based contact elements for a 3-hour curing period.

Parameter	Mortar Joint
Cohesive Stiffness	
K_{nn} (N/mm ³)	0.175
K_{ss} (N/mm ³)	0.175
K_{tt} (N/mm ³)	0.175
Damage Initiation	
t_n^o (MPa)	0.019
t_s^o (MPa)	0.019
t_t^o (MPa)	0.019
Damage Evolution	
Total/plastic Displacement	0.00001

3.2 Finite Element Modeling of Masonry Assemblage

Based on the model parameters presented in Section 3.1, a 3D numerical model that is representative of the experimental samples conducted in Chapter 2 was developed using the commercially available FEM software ABAQUS.

3.2.1 Definition of the Simulation Model

Initially, *3D Deformable Solid* parts that represent the concrete masonry blocks and Type S mortar were defined in the model space. Figure 3.3 represents the planar sketches and 3D deformable solids of the masonry blocks and mortar, respectively. From the actual dimensions of the masonry prisms, 2D sketches were drafted to represent the cross-sectional area of each masonry constituent. Once the 2D sketch was defined, the cross-section was extended to *3D Deformable Solid* by defining the depth of the solid. Two separate sketches were created for both top and bottom concrete masonry blocks, similar to the mortar. Moreover, the mortar was comprised of two separate solids, each with a depth of 5 mm to represent the 10 mm depth achieved in the experiments, as noted in

Section 2.1. A cut at the midpoint of the mortar was to allow for a planar surface where the crushing failure due to uniaxial compression can be defined, though this was not the focus of the current study. As such, four separate parts were created, *CMU_Bottom*, *CMU_Top*, *Mortar_Bottom*, and *Mortar_Top*.

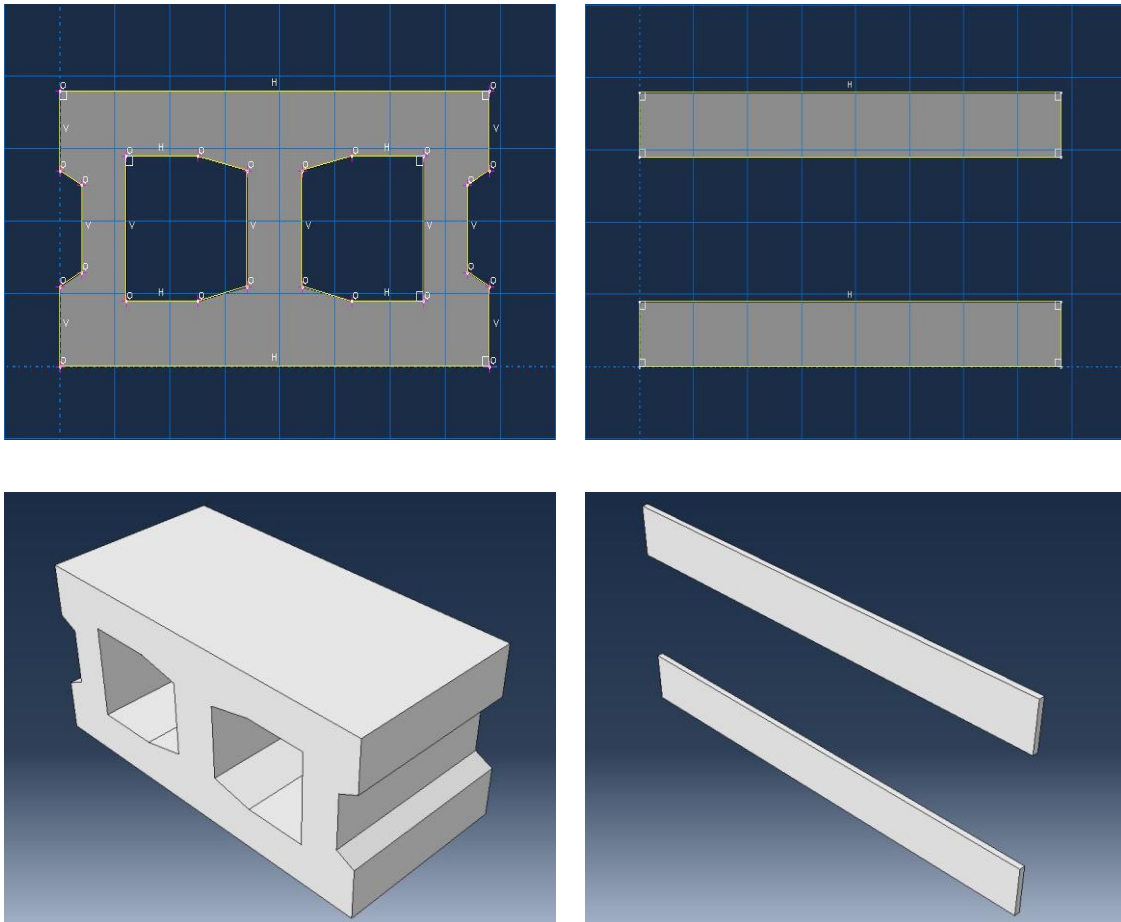


Figure 3.3: 2D planar sketches and 3D solids of masonry blocks and mortars.

Material properties were assigned to the rendered parts using the section assignment tool. Two separate solid homogenous sections classified as '*CMU_Sect*' and '*Mortar_Sect*' were created using the material data typical of that defined in Table 3.3 of Section 3.1 for concrete masonry block and mortar. Though masonry constituents are heterogeneous, no experimentation was conducted to investigate the variation of material properties with respect to directionality. Therefore, a homogenous material model was assumed. Table 3.5

shows the section assignment of each part and the material model associated with the section.

Table 3.5: Section assignment and the associated material model.

Part	Section Assignment	Material Model
<i>CMU_Top</i>	CMU_Sect	Concrete Masonry Unit (CMU)
<i>CMU_Bottom</i>		
<i>Mortar_Top</i>	Mortar_Sect	Type S Mortar – 3 Hours Cured
<i>Mortar_Bottom</i>		

Proceeding section assignment, a preliminary 3D assemblage structure was modeled in ABAQUS, as shown in Figure 3.4. The parts were used to create an assemblage in the model space. Individual parts were imported as '*instances*' into the model space where they were translated and rotated to build an '*assemblage*' structure typical of those samples used in experimentation. All instances generated from the unique parts defined above were made independent of each other as this allowed for further partitioning of each instance to allow for the creation of mesh transitions, as discussed in Section 3.2.2. After the assemblage was modeled, contact surfaces were created to simulate mortar debonding through a user-defined surface interaction. The interaction properties consisted of two distinct properties:

1. A global property assignment of a '*hard contact*' which created normal behavior to prevent elements from penetrating surfaces of other elements due to compressive forces.
2. A local property assignment based on the mortar debonding failure properties as specified in Table 3.4, was applied to the two surfaces at the top and bottom of the mortar. This allowed for debonding to occur once the criteria defined by Equation 3.3 were satisfied during the simulation.

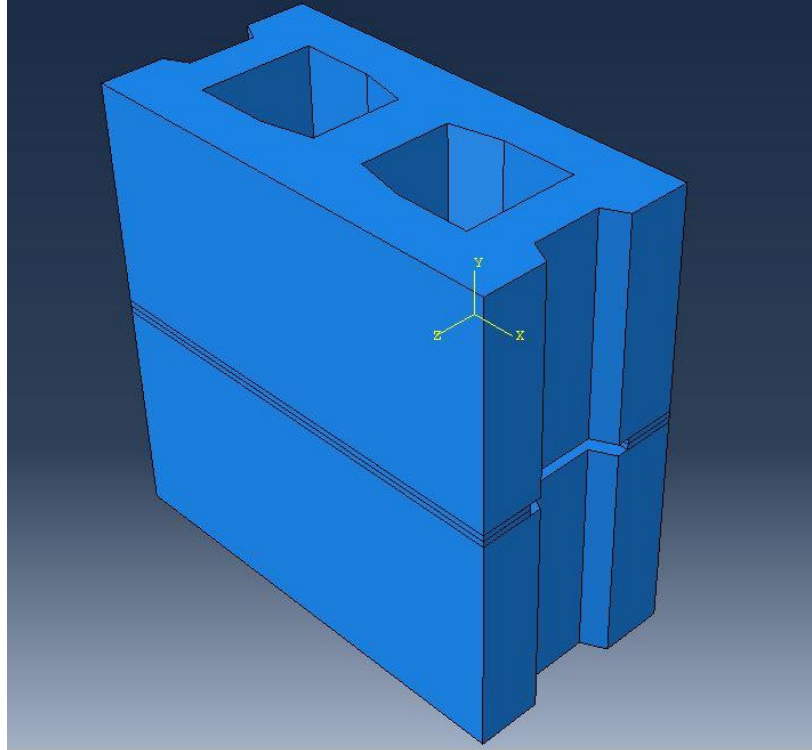


Figure 3.4: Preliminary assemblage structure in ABAQUS.

Once the physical solid model was assembled in ABAQUS, a preliminary mesh size was chosen to discretize the model. A standard, linear 8-node 3D stress element type classified as *C3D8* was used to mesh the assemblage. Elements with linear shape functions were chosen as the cohesion-based contact elements are only available for a linear geometric order, though quadratic elements may have produced more accurate results due to the higher-order shape function. Though reduced integration could be used for efficient computational times with regards to simulation, the potential of reduced stiffness and, therefore, flexible elements may have resulted in displacement mode shape distortion due to the phenomenon of '*hourglassing*'. Additionally, the use of reduced integration elements causes sudden inaccurate spikes in kinetic energy, which can be mitigated using full integration or viscous damping (Bayley 2016).

To simulate the application of a uniaxial tensile load on the structure, a '*step*' must be created within the problem history of *ABAQUS*. As cohesion-based contact elements are used to define the failure mechanism of the early-age masonry sample, a dynamic explicit

solver was used. However, the dynamic condition of the simulation was not representative of the static behavior of the experimentation. As such, the internal and external energies of the simulation were monitored during the application of the load to determine if a 'quasi-static' state was achieved using the explicit solver as described in detail in Section 3.2.2. Initially, the time step for the tensile loading simulation was set to 5 seconds, with NLGEOM turned on to account for geometric nonlinearity. A duration of 5 seconds was chosen to allow for the load to be applied slowly to reduce the kinetic energy of the model as discussed in Section 3.2.2. Additionally, the last second of the simulation provided increased loading such that the simulation could capture the masonry assemblage failing at loads higher than those determined in the experiments conducted.

The load and boundary conditions of the model were defined as displayed in Figure 3.5. As per Section 2.2, the bottom block experienced a 'fixed' base condition due to the tightening of threaded rods and the applied confinement pressure to the block through steel plates. As such, the displacement and rotation in all three global directions of the bottom cross-sectional surface of *CMU_Bottom* were set fixed to zero. During experimentation, the load was applied to the top masonry blocks through the use of two steel plates located parallel to the block's web. Therefore, to simulate the transference of the load from the steel plates to the masonry block, the load was defined as surface traction occurring on the ears of *CMU_Top*. The magnitude of the stress applied during loading was equivalent to the maximum force applied to the ears of the masonry blocks determined by the following equation:

$$\sigma_a = \frac{P_f}{A_e} \quad (3.5)$$

Where σ_a is the applied tensile stress on the ears of the top masonry block in the simulation in MPa, P_f is the load at debonding failure in N and A_e is the area of the ears of the top masonry block calculated as 41,800 mm².

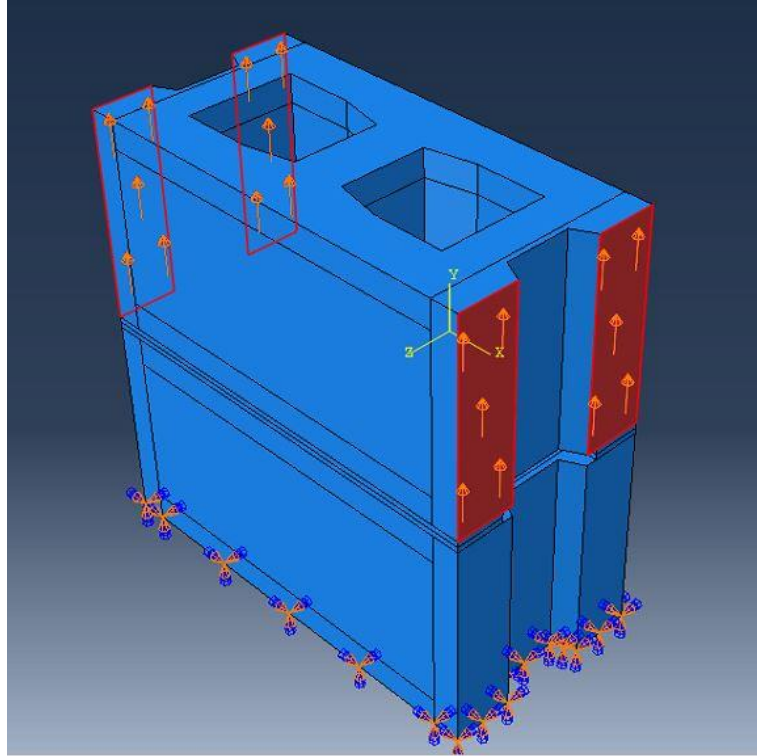


Figure 3.5: Application of loading and boundary conditions.

3.2.2 Quasi-static Condition

As stated previously, although the uniaxial tensile load applied during the experimental testing is considered static, a dynamic analysis must be used in *ABAQUS* to simulate contact surface for debonding failure. Moreover, the following conditions regarding the energy of the system must be met to consider a 'quasi-static' condition when performing the dynamic analysis (MIT, 2017):

1. The external energy (W) applied to the model due to various forces must be nearly equivalent to the internal energy (E_I) of the system for a given time instance of the simulation.
2. The total energy (E_T) of the simulation should be significantly small when compared to the internal and external energies.
3. The kinetic energy (E_K) should be approximately 5-10% of the total internal energy for the duration of the experiment.

These energies were monitored throughout the simulation to ensure a quasi-static simulation was achieved, as shown in Figure 3.6. Though the internal and external energies remained relatively equivalent throughout the initial simulation, the kinetic energy was a significant percentage of the internal energy, especially at the beginning of the simulation. As such, the simulation under the current parameters behaved as a dynamic analysis rather than a quasi-static analysis. This was primarily due to the fact the load was applied over an extremely short time period of one second. Due to the rapid application of the load, the transition of kinetic to the internal energy of the elements in the vicinity of the load does not occur. Moreover, there is a tendency at the beginning of the simulation for the model to behave as a rigid body with a velocity rather than a body that is deforming, which accounts for increased kinetic energy.

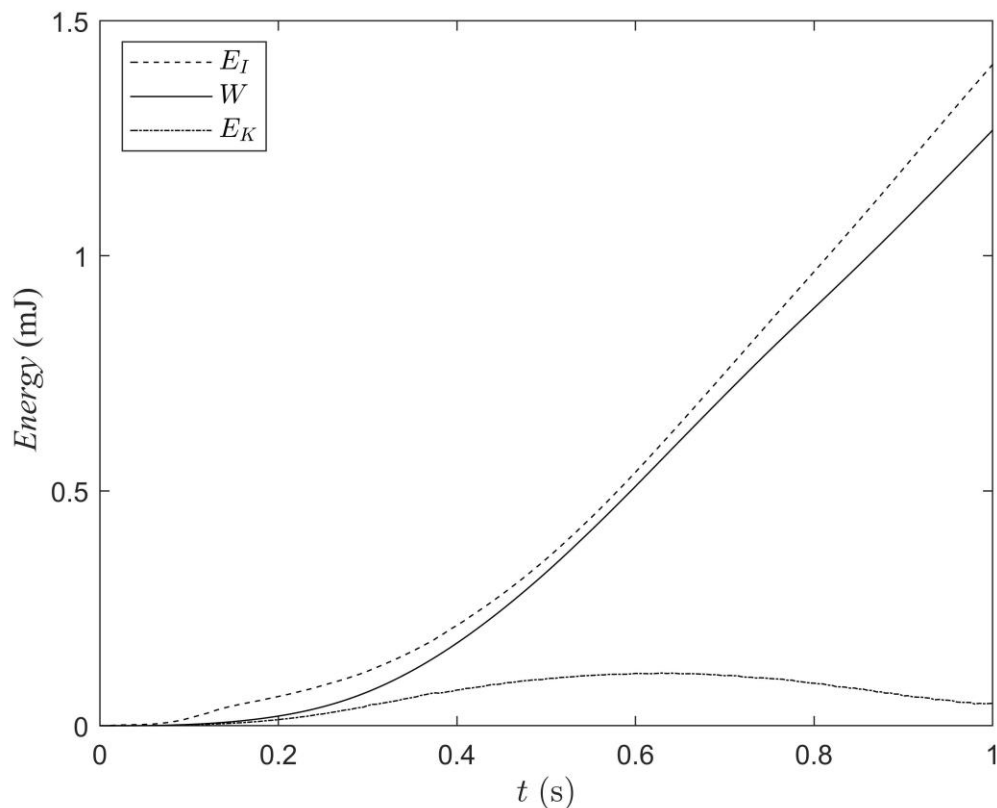


Figure 3.6: Variation of the kinetic, internal, and external energy.

As such, to reduce the overall kinetic energy during simulation, the load must be applied over a larger period of time. This allows for the elements in the model to adjust to the application of the load, thus reducing the kinetic energy. Figure 3.7 shows the variation of kinetic energy as a percentage of the internal energy with respect to time for various loading curves. Four loadings curves with a time interval of 1, 2, 3, and 4 seconds were used for comparison. As the loading time increased, the overall slope of the curve and, therefore, the magnitude of the load that was applied decreased as per Table 3.6.

Table 3.6: Loading curves for varying time intervals

Load Duration (s)	1	2	3	4
Loading Rate (kPa/s)	1	0.5	0.33	0.25

From Figure 3.7, it can be observed that for a loading duration of 4 seconds that the kinetic energy as a percentage of the internal energy has reduced significantly enough that we can consider the analysis to be “quasi-static”. As such, a load rate occurring over 4 seconds was used for the applied load.

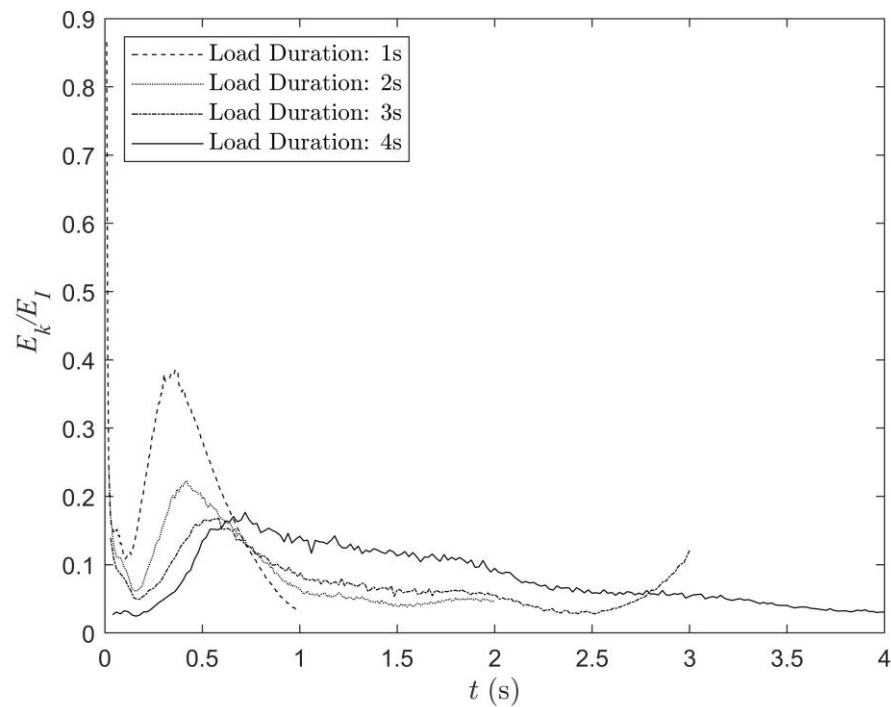


Figure 3.7: Variation of the percentage of kinetic energy with load duration.

3.2.3 Mesh Sensitivity Analysis

As mentioned in Section 3.2.1, a standard, linear 8-node 3D stress element was used to discretize the 3D solid model. A linear interpolation function was used to calculate the variation of displacement between nodes for a singular element. Since strains are the partial integration of this displacement and their shape functions across x, y and z-direction and stress is proportional to strain through Hooke's law, the variation of the stress and strain across the element remains constant. However, the variation of the stresses and strain due to the application of the load, in reality, may vary with respect to a higher-order function. Therefore, the C3D8 elements only approximated the real stress distribution of the simulated masonry course. As such, a detailed mesh sensitivity analysis was conducted on the model to ensure accurate stress, and strain results were obtained. Using a coarse mesh with low element density will result in faster computational times; however, the stress and strain values will have a significant error due to the estimation of the larger elements. Conversely, using a fine mesh with high element density allows for accurate estimation of the stress and strain parameters, but it requires high computational times and may lead to issues with solution convergence (MIT, 2017). Additionally, elements should maintain an aspect ratio (AR) of 3 for stress analysis as stress distortion can occur across elements with a higher aspect ratio. Table 3.7 shows the variation of normal stress, computational time, and the percentage of elements with poor AR.

Table 3.7: Mesh sensitivity analysis of 3D simulated masonry course.

Max Element Size (mm)	40	20	10	5
<i>Stress-22</i> (MPa)	0.00165	0.00136	0.00127	0.00120
Error	--	17.5%	6.6%	5.5%
Simulation Time (Hr)	1.50	5.52	10.21	13.52
AR > 3.0	9.52%	5.71%	0.0%	0.0%

Though a maximum element size of 5 mm gives the best stress accuracy and elements poor element distortion due to high aspect ratios, the simulation takes a very long time to complete (> 13 hours). Mesh transitioning, as shown in Figure 3.8 (a) – (b) is used to reduce the computational time of the simulations while continuing to provide accurate results. A

fine mesh was used in locations where debonding occurred, loads were applied, or stress concentrations due to stress singularities were to occur (such as sharp edges) while coarse mesh was used elsewhere. The assemblage was partitioned into multiple sections to allow for the creation of transition regions from fine to coarse meshes. The final mesh distribution contained 445,000 elements with a stress error of 6.2% and contained 0.02% of elements that had an AR greater than 3.0. Those distorted elements were not in locations that were critical to the analysis of the simulation.

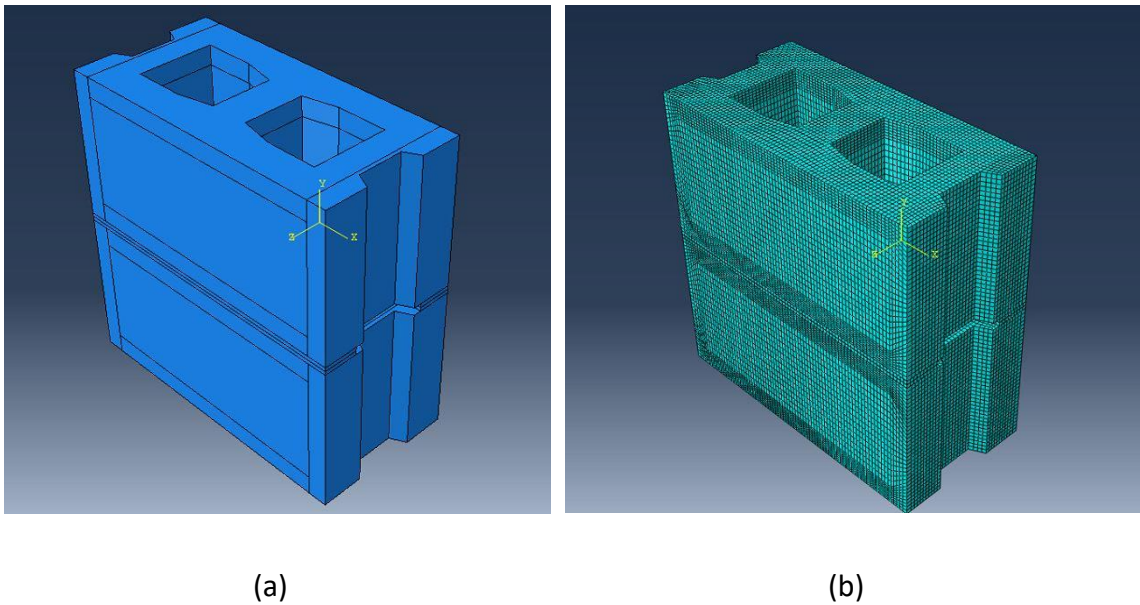
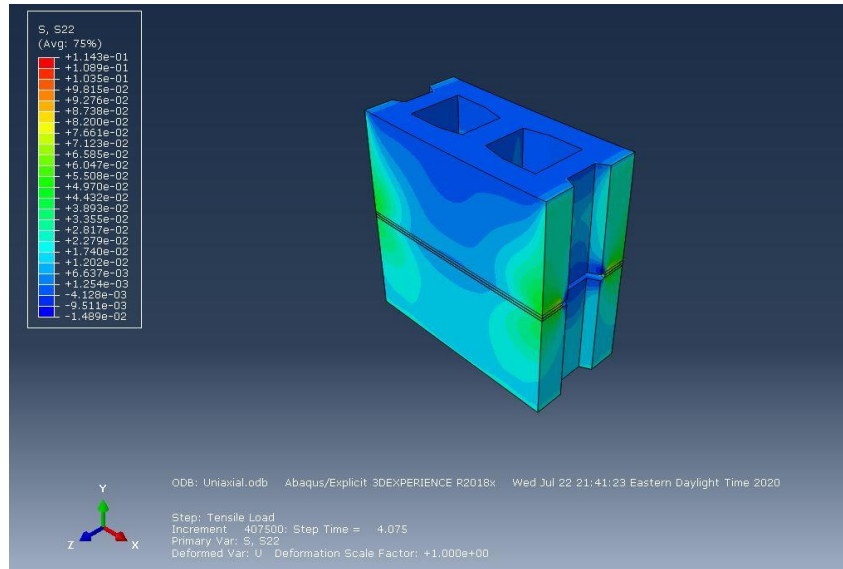


Figure 3.8: (a) Final assemblage partition and (b) mesh distribution.

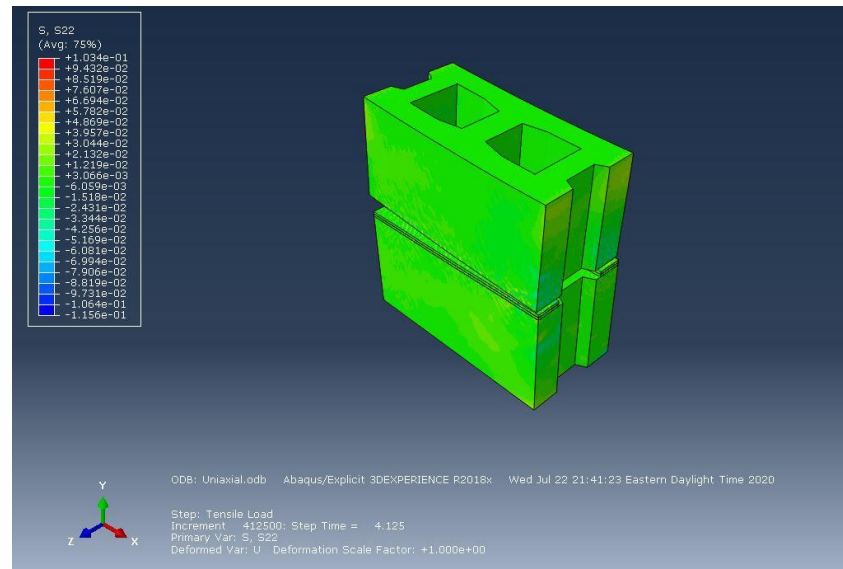
3.3 Comparison of Numerical and Experimental Results

The normal stress of the simulated masonry assemblage under uniaxial tensile load before and after debonding failure is shown in Figure 3.9 (a) – (b). The dissipation of the normal stress gradients, in addition to the separation of the top masonry block, depicted an accurate representation of the failure behavior observed during experimentation. Moreover, this failure occurs instantaneously; over a time interval of 0.025s, similar to the brittle nature typical of the debonding failure. Once the simulation was completed, the simulated mortar strips were isolated from the masonry units by creating a display group, as shown in Figure 3.1. The numerical stress-strain parameters were only based on the elements of the simulated mortar, considering the stress-strain parameters were only quantified across the

depth of the mortar during experimentation. Moreover, by reducing the number of elements, the numerical stress-strain data can be more readily extracted from the elements as there are computational limitations to the number of XY datasets that ABAQUS can extract.



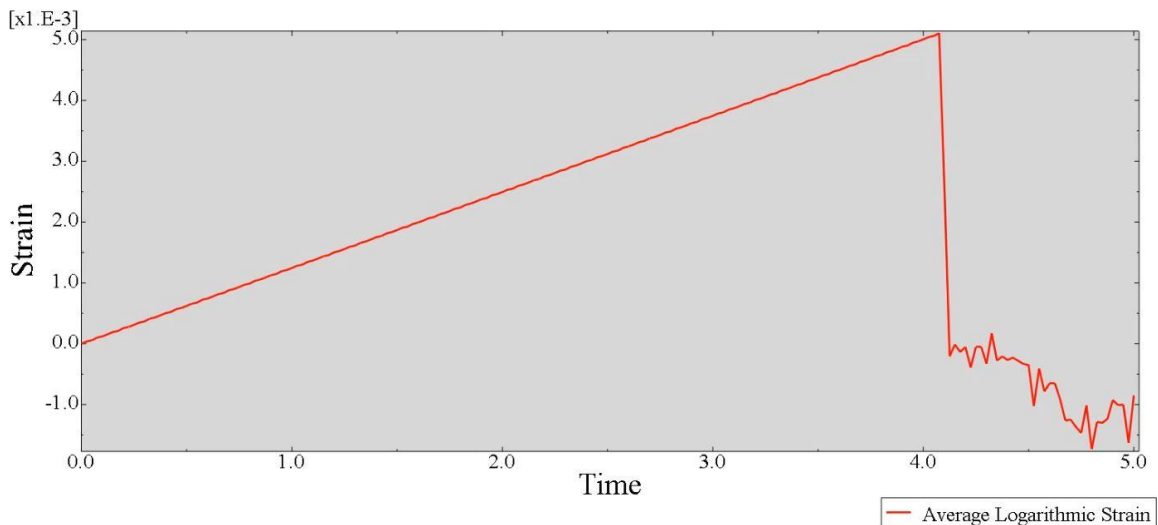
(a)



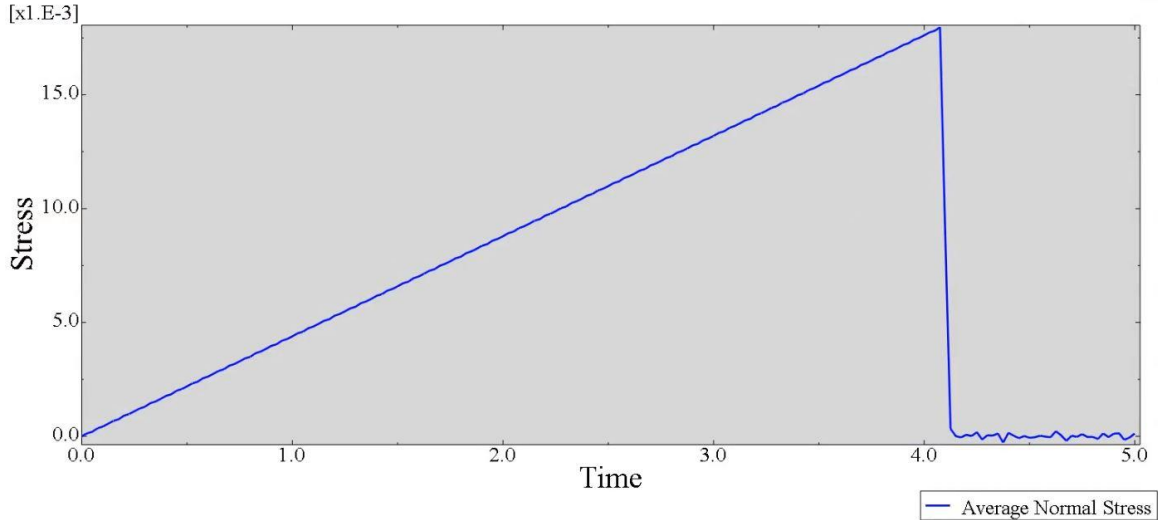
(b)

Figure 3.9: Normal stress gradients (a) before and (b) after the failure.

The variation of average normal stress and average normal logarithmic strain of the mortar elements with respect to simulation time extracted from ABAQUS are depicted in Figure 3.10. Once the mortar display group was created, the XY curve data for the field outputs, normal stress, and normal logarithmic strain were extracted from the elements that represented the mortar. These extracted XY data curves were then mathematically operated on using an available mathematical expression builder in ABAQUS. Expressions were created to determine the average normal stress, average normal logarithmic strain, and maximum normal stress from the extracted XY data. The variation of these variables with respect to simulation time was extracted as ".txt" files such that a comparison to the experimental results summarized in Chapter 2 could be made.



(a)



(b)

Figure 3.10: Average normal stress (a) and average logarithmic strain (b) extracted from ABAQUS.

From the exported data, E value, σ_d , ε_d and tensile stress at failure (σ_f) from the numerical simulation can be quantified. Based on a normalized loading rate of 0.25 kPa/s as discussed in Section 3.2.2, σ_f was determined by calculating the product of the loading rate and the simulated time where the debonding failure occurred. Similarly, the peak average normal stress and average normal logarithmic strain from Figure 3.10 were taken as σ_d and ε_d for the numerical simulation. Furthermore, the logarithmic strain values were converted to engineering strain values for comparison to the experimental results using the following equation (Martin 2015):

$$\varepsilon_{t,i} = e^{\varepsilon_l} - 1 \quad (3.6)$$

Where $\varepsilon_{t,i}$ is the elastic tensile strain at time step 'i' and ε_l is the logarithmic strain at time step 'i'. However, due to the values of the tensile strain to be significantly small, this conversion generates minimal differences between logarithmic and engineering strain. The numerical E value was determined using a zero-intercept linear regression model, as described in Section 2.5.2. Figure 3.11 shows the comparison of the stress-strain behavior of the experimental and numerical results for a 3-hour curing period. Table 3.8 shows the

comparison between numerical and experimental E value, σ_d , ε_d , and σ_f for a 3-hour curing period. The numerical simulation was able to capture the elastic stress-strain behavior of the masonry assemblage with significant accuracy when compared with the experimental results.

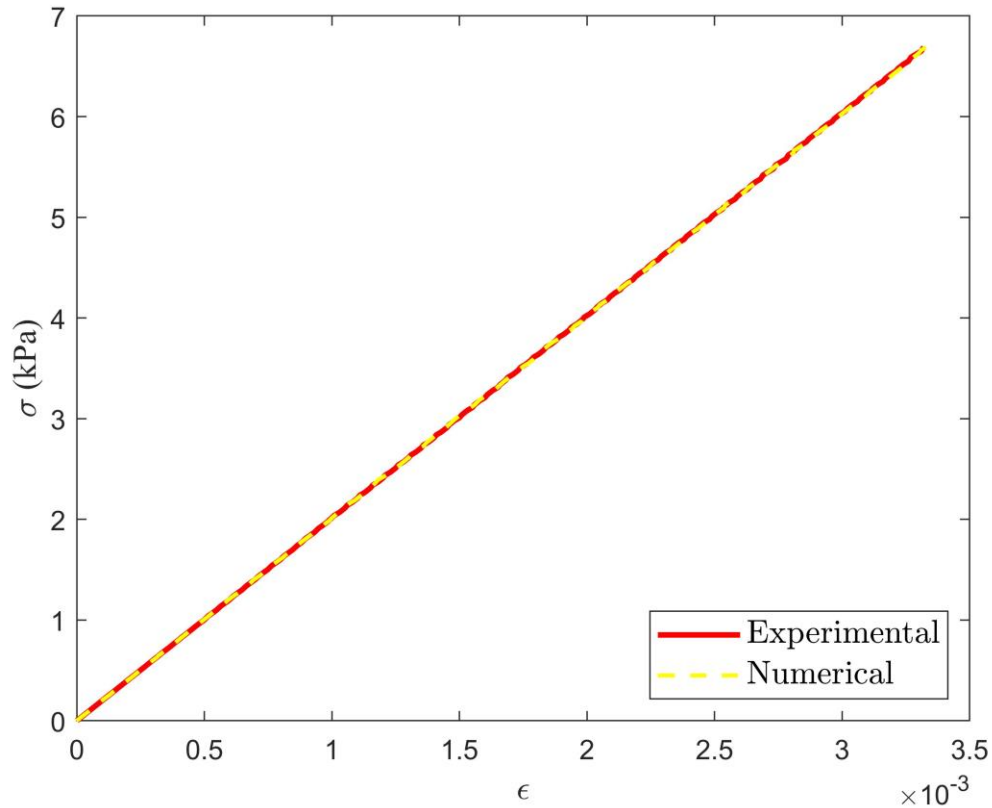


Figure 3.11: Comparison of experimental and numerical E values.

Table 3.8: Comparison of experimental and numerical stress-strain parameters for the 3-hour curing.

Parameter	Experimental	Numerical	Error (%)
E (MPa)	2.012	2.009	0.08
σ_d (kPa)	6.686	6.701	0.23
ε_d	3.324e-03	3.337e-03	0.41
σ_f (kPa)	5.545	5.614	1.25

Furthermore, Table 3.9: Percentage error between experimental and numerical stress-strain parameters across all the curing periods. that show a similar level of accuracy across all

curing times, demonstrating the robustness of the proposed modeling technique. Therefore, the proposed numerical model can accurately quantify the elastic tensile behavior and failure mechanism of two-course masonry prisms that were cured between 3 and 72 hours. Though this model shows significant accuracy for representing the elastic tensile stress-strain behavior and failure mechanism of early-age masonry assemblages, there are still areas in which the improvement could be made. Currently, this model requires the calculation of the K_t value; such the σ_d can be adjusted to accurately simulate the correct debonding failure during the simulation. However, if the damage initiation of the cohesion-based interface was based on the average normal stress of all the elements in the mortar rather than element by element, the need for the K_t factor could be eliminated. Additionally, the model could be further hyper-tuned to improve the accuracy by quantifying the variation of ϕ with respect to curing time such that the accuracy is consistent across all curing periods. Moreover, the proposed modeling technique is only valid for elastic tensile behavior of two-course concrete masonry assemblages, as stated previously. Further experimental testing would need to be conducted to quantify the behavior of masonry assemblages under compression and shear loads such that an accurate numerical model could be developed. The effects of different material properties for the mortar and blocks, variations in the cross-sectional area of masonry block, and the number of masonry courses should also be investigated with respect to defining an accurate numerical simulation.

Table 3.9: Percentage error between experimental and numerical stress-strain parameters across all the curing periods.

Early-ages (Hr)	Error in E (%)	Error in σ_d (%)	Error in ε_d (%)	Error in σ_f (%)
--------------------	------------------	-------------------------	---------------------------------	----------------------------

3	0.08	0.23	0.41	1.25
4	0.08	0.24	0.38	1.25
6	0.17	0.37	0.61	1.88
7	0.14	0.43	0.72	1.88
13	0.22	1.10	1.46	1.88
18	0.24	0.89	1.27	1.88
24	0.24	0.89	1.27	1.88
48	0.27	1.03	1.46	1.88
72	0.28	1.12	1.58	1.88

3.4 Case Study – Masonry Walls under Construction

In Section 3.1 – 3.3, an accurate numerical model was defined for the early-age uniaxial tensile behavior of two-course masonry assemblages. Correlating the numerical properties of a small-scale study to a larger structure such as a masonry wall may present unique challenges, which is further explored in this section. In the proposed numerical model, the properties were modeled microscopically such that the local failure mechanism and contact pressures of the mortar-block interface were accurately quantified. For a large-scale structure such as a masonry wall; however, the global behavior and failure mechanisms are critical to defining the accurate behavior of the wall under out-of-plane lateral loads such as wind and earthquake. Therefore, a macro modeling technique has been presented to accurately capture the global behavior of a masonry wall to accurately quantifying the failure mechanism defined in Section 3.3.

3.4.1 Macro model of the Masonry Wall

As defined in Section 1.2.1.2, the macro modeling technique utilizes the properties of individual elements (mortar, masonry block, etc.) to define an average material model that is represented across a single element. As the mortar and masonry blocks are no longer represented by separate units, an “*expanded unit*” is used to represent them. This approach has been noted as accurately capturing the global behavior of structures while being relatively computational inexpensive to simulate. A recent study by (Abdulla *et al.* 2017) presented a macro modeling technique for expanded units where the adjusted E values were based on several springs that were connected in series; as such, a similar technique has

been adopted for this thesis. For an expanded masonry unit of 195 mm in height, representing the full height of the masonry block plus half the height of the mortar, the equivalent E value (E_{eqv}) can be calculated from the following equation assuming the mortar and block act as springs in series:

$$E_{eqv} = \frac{HE_B E_M}{H_B E_M + H_M E_B} \quad (3.6)$$

Where H is the height of the expanded masonry unit (195 mm), E_B is the Modulus of Elasticity of the block defined in Table 3.1, E_M is the Modulus of Elasticity of the mortar defined in Table 3.3 and Appendix B.1 – B.8, H_B is the height of the masonry block (190mm), and H_M is the height of half of the mortar (5 mm). For the proposed macroscopic model, the units are additionally expanded in the transverse direction to account for half the depth of the head joint. Moreover, the detailed geometry of the masonry blocks and mortar has been simplified to a simple rectangular cross-sectional area. Figure 3.12 shows the proposed geometry of the expanded masonry units and the assemblage of these units in ABAQUS.

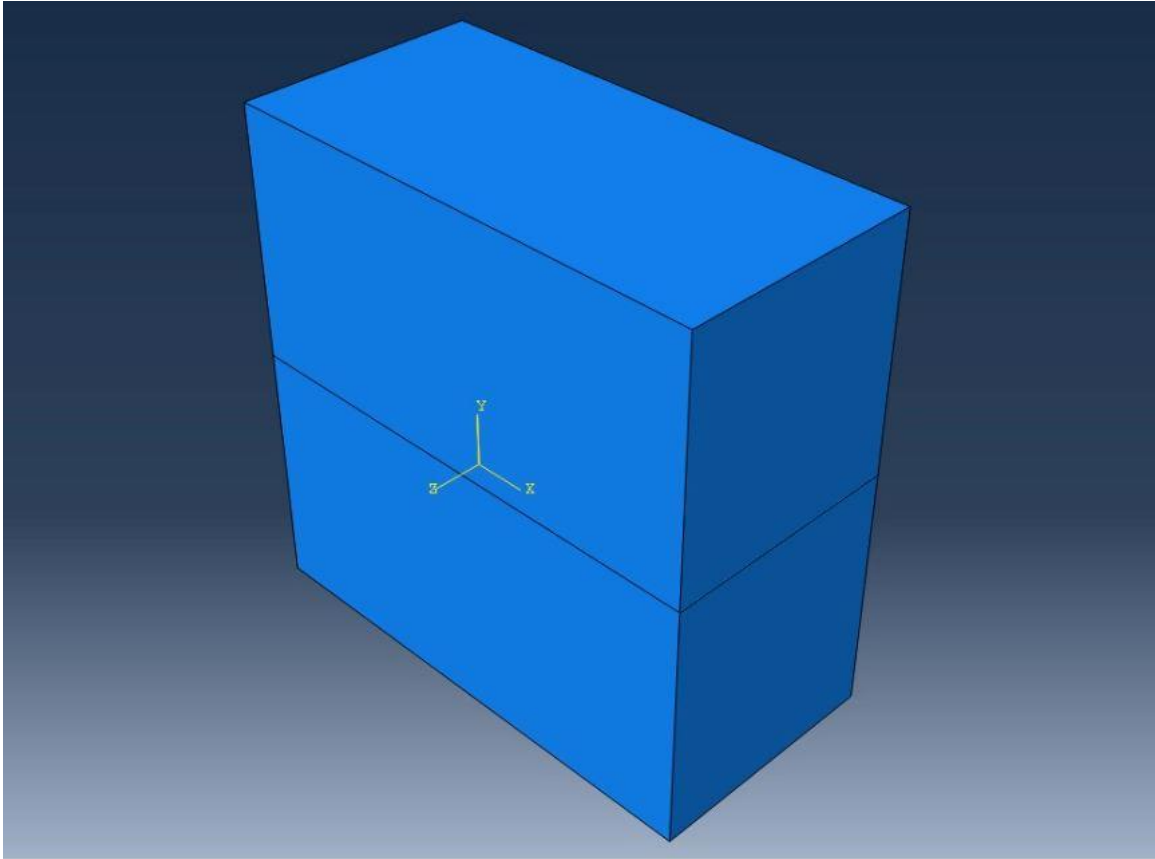


Figure 3.12: Macroscopic model of the expanded masonry prism.

The development of the model and simulation was conducted using the similar techniques outlined in Section 3.2. However, the following adjustments were made to ensure an accurate representation of the experimental results was obtained:

1. The K_t and φ values from Equation 3.4 are 2.90 and 1.08, respectively for this model. It is hypothesized that the reduction in the K_t value compared to the microscopic model is due to decreased geometric complexity of the cross-sectional area of the macro model resulting in decreased stress gradients. Moreover, unlike the microscopic model, φ exceeds unity suggesting the product of K_t and σ_d is a conservative estimate for the numerical debonding stress. The increase in φ may be due to the fact the cross-sectional area is approximately twice as large as the microscopic model resulting in reduced contact stress across the mortar-bond interface.

2. To address the stress concentrations, E_{eqv} is reduced by a factor of 0.91. The reduction is less than the microscopic model (0.87) because of the decreased stress concentrations due to the factors mentioned in (1).
3. The random spikes in E_k were not observed during the simulation of the uniaxial tensile behavior of the macroscopic model. As such, reduced integration elements with stiffness-based hourglass control was used to reduce the computational time of the simulation. The model takes approximately 10 minutes to run using C3D8R elements.
4. Lastly, the mesh was updated such that an approximately 10 mm element size was used over the entirety of the model resulting in 29640 elements with none exhibiting an $AR > 3.0$.

Table 3.10 summarized the strength parameters, cohesion-based interface properties and loading values for all curing periods for the macroscopic model.

Table 3.10: Strength, cohesion and loading parameters for the macro model across all curing periods.

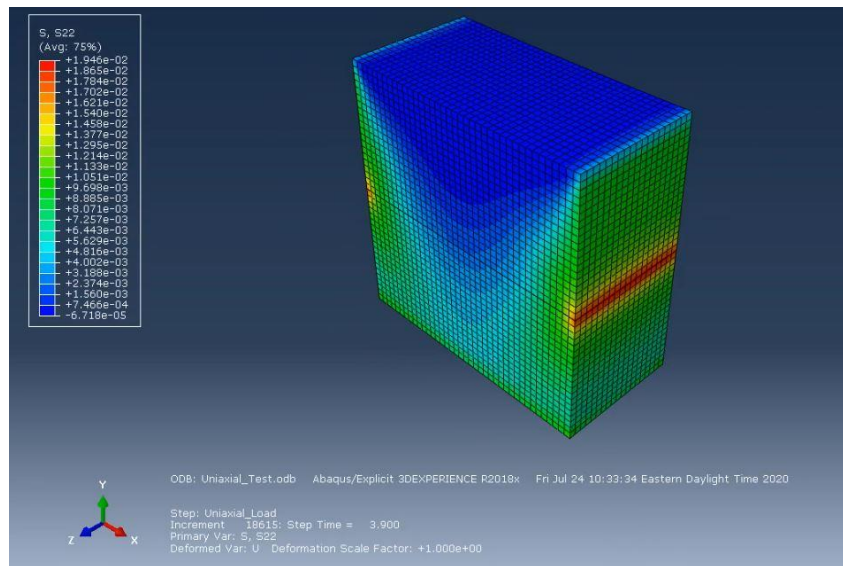
Parameter	Curing Period (Hrs)								
	3	4	6	7	13	18	24	48	72
Strength Parameters									
ρ (ton/mm ³)	2e-09	2e-09	2e-09	2e-09	2e-09	2e-09	2e-09	2e-09	2e-09
ν	0.25	0.25	0.25	0.25	0.25	0.25	0.25	0.25	0.25
E_{eqv} (MPa)	1.824	2.092	2.470	2.614	3.193	3.497	3.765	4.412	4.791
Cohesive Stiffness									
K_{nn} (N/mm ³)	0.182	0.209	0.247	0.261	0.319	0.350	0.377	0.441	0.479
K_{ss} (N/mm ³)	0.182	0.209	0.247	0.261	0.319	0.350	0.377	0.441	0.479
K_{tt} (N/mm ³)	0.182	0.209	0.247	0.261	0.319	0.350	0.377	0.441	0.479
Damage Initiation									
t_n^0 (MPa)	0.021	0.028	0.037	0.041	0.056	0.063	0.070	0.087	0.096
t_s^0 (MPa)	0.021	0.028	0.037	0.041	0.056	0.063	0.070	0.087	0.096
t_t^0 (MPa)	0.021	0.028	0.037	0.041	0.056	0.063	0.070	0.087	0.096
Damage Evolution									
Total/plastic Displacement	1e-05	1e-05	1e-05	1e-05	1e-05	1e-05	1e-05	1e-05	1e-05
Load									
Surface Traction Load (kPa)	6.685	8.860	11.93	13.09	17.77	20.23	22.41	27.65	30.71

3.4.1.1 Results of the Macro Modeling Technique

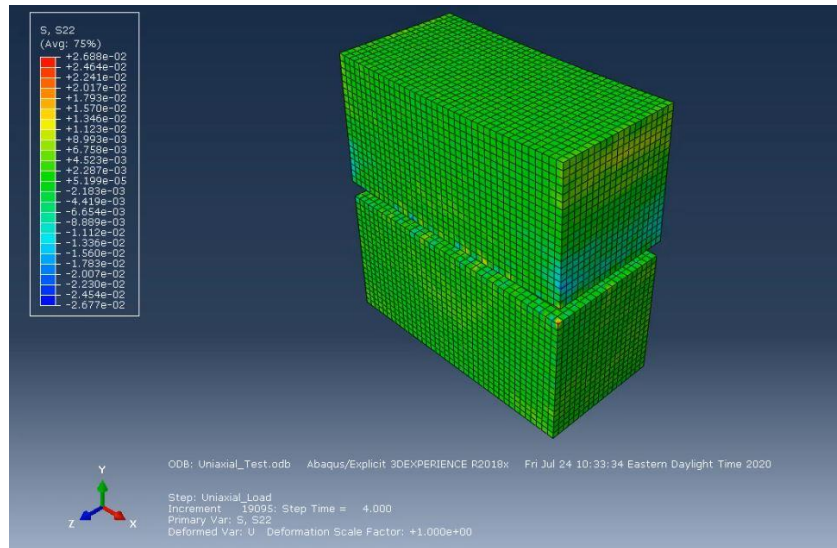
The normal stress of the micromodel under uniaxial tensile load before and after debonding failure is shown in Figure 3.13 (a) – (b). The brittle de-bonding failure observed in experimentation and simulated in the microscopic model is represented similarly accurately by the macroscopic model. Moreover, Table 3.11 shows the error between experimental and numerical stress-strain parameters for the macro model for all curing periods. The results suggest that similar to the micro model proposed, the macro model accurately simulates the elastic tensile behavior of the masonry assemblages in addition to the debonding failure mechanism observed during the experiments.

Table 3.11: Percentage error between experimental and numerical stress-strain parameters for macro model across all curing periods.

Early-ages (Hr)	Error in E (%)	Error in σ_d (%)	Error in ε_d (%)	Error in σ_f (%)
3	0.32	3.95	4.21	2.50
4	0.32	3.48	3.94	2.50
6	0.29	3.63	3.89	2.50
7	0.25	4.49	4.98	3.75
13	0.23	4.55	4.78	3.75
18	0.22	4.50	4.71	3.75
24	0.22	4.82	4.79	3.75
48	0.19	4.60	4.77	3.75
72	0.07	4.50	4.66	3.75



(a)



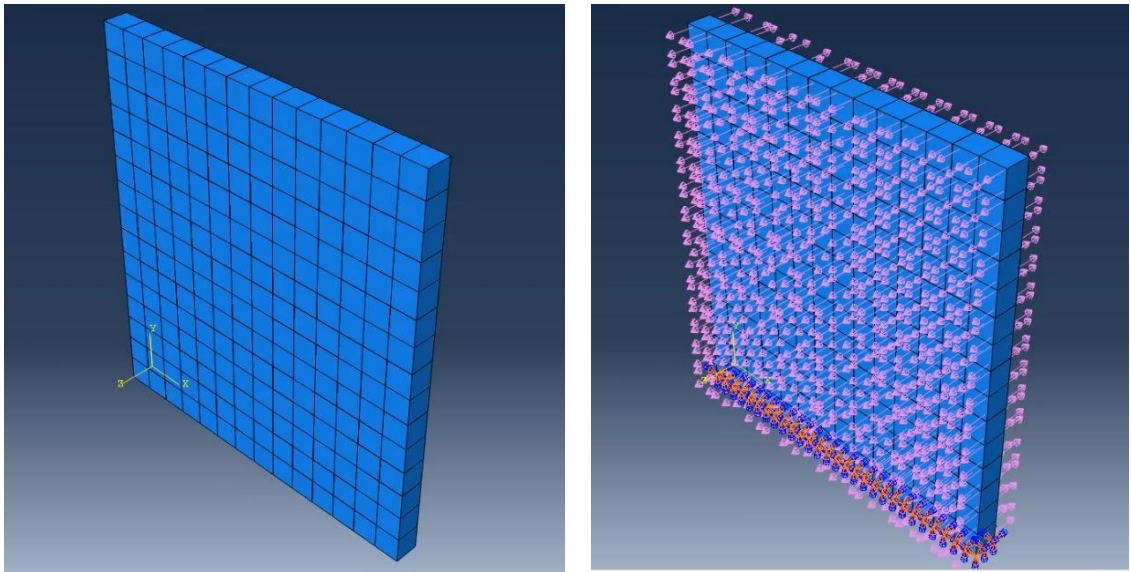
(b)

Figure 3.13: Normal stress gradients (a) before and (b) after the failure of the macro model.

3.4.2 FEM of the Early-Age Masonry Wall

With a macroscopic modeling technique defined for early-age masonry, a preliminary simulation was conducted for a masonry wall under out-of-plane wind loading. This simulation has two primary objectives: (1) to determine the horizontal forces applied to the structure due to wind loads and the temporary bracing and (2) to determine if a failure occurs in the structure with or without temporary bracing. Figure 3.14 (a)-(b) depicts a standard 3m x 2.8 m 12-hour cured masonry wall under wind loading. The material properties were defined using the techniques described in Section 3.4.1 for the macroscopic modeling approach. As the 15-course masonry wall is assumed to be 12 hours in age, the material properties of each layer of the wall based on the curing time since construction has occurred. For example, the bottom layer would have material properties based on a curing time of 12 hours while the next layer's material properties would be based on a curing time of 11.2 hours. Table 3.12 shows the variation of the curing period with respect to the layers of the wall going from the bottom to the top. Since the material properties were only defined for a curing period of 3 – 72 hours, it was assumed that those layers less

than or equal to 3 hours of curing would have equivalent material properties similar to 3 hours of curing.



(a)

(b)

Figure 3.14: (a) Macroscopic model of the early-age masonry wall and (b) applied wind loading.

Table 3.12: Variation of the curing period with height of the masonry wall.

Layer #	Curing Period (Hrs)
1	12.00
2	11.20
3	10.40
4	9.60
5	8.80
6	8.00
7	7.20
8	6.40
9	5.60
10	4.80
11	4.00
12	3.20
13	3.00
14	3.00
15	3.00

The wind load used in the simulation for a masonry wall during construction was defined as per (CSA Group, 2014). From Annex B, article B.3 states that “*The anticipated wind load should be assumed to be 50% of the load based on a probability of one in fifty. A load factor of 1.25 should be used with anticipated wind loads in limit states design*” (CSA Group, 2014). Therefore, the wind load was designed as per the (National Research Council Canada, 2015), Section 4.1.7 “Wind Load”. As per cl: 4.1.7.2. (1) - (3), a preliminary modal analysis was conducted in ABAQUS to determine if the early-age masonry wall requires dynamic or static procedures with respect to the design of wind load. The first fundamental frequency was calculated to be 0.157 Hz, therefore as per cl: 4.1.7.2. (3) (a) this masonry wall was classified as very dynamically sensitive. Therefore, in conjunction with cl: 4.1.7.8 for the dynamic procedure, the internal and external wind loads were calculated using the following equations as per 4.1.7.3.(1) and 4.1.7.3.(3):

$$p = I_w q C_e C_t C_g C_p \quad (3.7)$$

$$p_i = I_w q C_{ei} C_t C_{gi} C_{pi} \quad (3.8)$$

Where p is the specified external wind pressure acting in a normal direction to the surface, p_i is the specified external wind pressure acting in a normal direction to the surface, I_w is the important factor as per Table 4.1.7.3, q is the reference velocity pressure in (kPa), C_e is the exposure factor as per 4.1.7.8.(2) and (3), C_{ei} is the exposure factor for internal pressure as per 4.1.7.3.(7), C_t is the topographic factor as provided in 4.1.7.4, C_g is the gust effect factor as per 4.1.7.8.(4), C_{gi} is the gust effect factor as per 4.1.7.3.(10), C_p is the external pressure coefficient as provided in 4.1.7.5 and 4.1.7.6 and C_{pi} is the external pressure coefficient as provided in 4.1.7.7. Additionally, a gravity load was applied to the structure, and a factor of 1.25 was applied per the load combination for limit states design. Due to the size and intensity of the loads applied to the wall, the simulation duration was increased to 9 seconds, and the loading rate was decreased to 0.125 kPa/s to reduce the concentration of K_e in the model to achieve a quasi-static state. Additionally, to ensure the maximum horizontal force was captured during simulation for the temporary bracing design, the t_n^o , t_t^o , and t_s^o were set to 1 MPa to prevent debonding failure. Therefore, the total duration of the simulation was increased to approximately 24 hours in length to run the combination of gravity and wind load on the structure.

3.4.2.1 Limitations of FEM of Early-age Masonry Walls

Though a preliminary simulation was conducted on the proposed early-age masonry wall, it was observed that the structural response of the wall was significantly inaccurate. Figure 3.15 shows the deflection of the wall after the application of wind and gravity loading. It can be observed that the top of the wall deflects approximately 4.0 m, which is unrealistic for the masonry wall presented in the study.

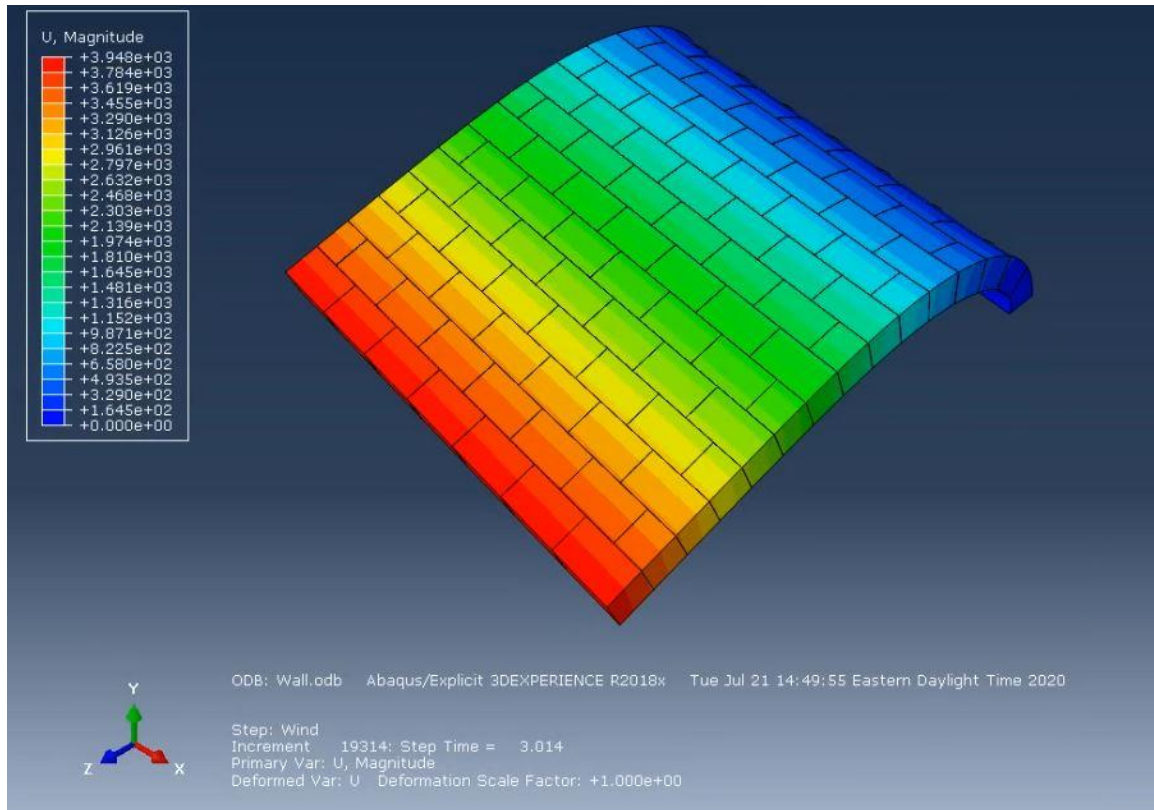


Figure 3.15: Deflection of simulated early-age masonry wall under wind and gravity loads.

Therefore, before accurate simulations of early-age masonry walls can be conducted, the uniaxial compressive behavior of the wall must be determined for early-age masonry through experimentation. Typically, the strength parameters of concrete-based masonry elements are based on the compressive E values (E_c), not tensile. Currently, since the model is based on the E values determined from uniaxial tensile tests, the wall exhibits drastically reduced stiffness resulting in greater deflections, as shown in the previous figure. Though the “Standard Practice for Bracing Masonry Walls Under Construction” (MCAA, 2012) does provide E_c values for unreinforced masonry blocks and Type S mortar cement, these values only apply to the intermediate period, which occurs 24 hours after initial construction has begun. Before this during the initial period, it is assumed that the wall provides no strength with regards to resistance to lateral based loads. However, from the experimental study conducted in Chapter 2, it has been demonstrated that this is misrepresentative, as early-age masonry does in fact, have quantifiable strength and

therefore, may resist a portion of the applied load. Without the stress-strain behavior of early-age masonry under uniaxial compressive loads, the following issues can not be addressed:

1. The modal analysis used to define the wind load is conservative, resulting in an inaccurate wind load used for bracing design. In the study presented, it was determined the first fundamental frequency to be 0.157 Hz. This value is conservative because the stiffness is based on the tensile properties, not the compressive properties of the masonry. As such, the fundamental frequency should be higher, affecting the C_g factor used to calculate the wind load.
2. The stiffness of the walls should be based on the E_c value, not the ones determined from the early-age tensile testing. This results in increased structural responses due to the decreased stiffness of the wall. Therefore accurate elastic responses and failure mechanisms can not be simulated accurately or effectively.
3. There is a possibility that masonry at early-ages could fail under compressive loads. Currently, there are no studies for early-age masonry properties under uniaxial compressive loads. Under wind loading, the wall experiences both compressive and tensile load occurring on either side of the centroidal line of the structure. Therefore, there is potential for the wall to fail under compressive stresses, which is currently not available.

3.5 Conclusions

Though studies on the density of early-age mortar may provide a more accurate model, it would be difficult to accurately define the volume of the mortar at early-age as it is extremely fragile and does not hold shape readily. Moreover, measuring the density would only contribute to the variability of the model due to fluctuating environmental conditions during curing as discussed in Section 2.5.3. Similarly, it was anticipated that a ν equal to 0.25 only represents the average behavior of the assemblages overall curing periods. At early ages (3-4 hours) the mortar would behave more as a fluid and, therefore, would have a higher ν value. As hydration occurs and the solid structure starts to form, the ν would

decrease, resulting in a correlation between v and curing period. The inaccuracies due to the lack of representative data for the compressive behavior of early-age masonry as stated in Section 3.4.2.1 need to be addressed. Lastly, the presented study does not investigate the behavior of early-age masonry with regards to the application of shear loads. Future research would have to be conducted to measure the fluctuation of these parameters and explore the variation of shear strength with respect to curing time.

3.6 References

Abdulla, K., Cunningham, L., and Gillie, M. (2017), "Simulating masonry wall behavior using a simplified micro-model approach," *Engineering Structures*, 151, 349-365.

Aref, A. J. (2013). A three-dimensional cyclic meso-scale numerical procedure for simulation of unreinforced masonry structures. *Computers and Structures*, 120, 9 - 23.

Bayley, J. (2016). Re: What could cause a sudden Kinetic Energy Spike in ABAQUS Quasi-Static Analysis?. Retrieved from: https://www.researchgate.net/post/What_could_cause_a_sudden_Kinetic_Energy_Spike_in_ABAQUS_Quasi-Static_Analysis/571fa0bd404854d53943b7f1/citation/download.

Berlo, S. (2009). *Stress concentration effects in highly localized functionally graded materials*. University of Rhode Island.

Baeker, Martin. (2015). Re: How can I convert Logarithmic Strain to Engineering Strain in Abaqus?. Retrieved from: https://www.researchgate.net/post/How_can_I_convert_Logarithmic_Strain_to_Engineering_Strain_in_Abaqus/559e786b5e9d971b358b45fb/citation/download.

Bolhassani, M. H. (2015). Simplified micro modeling of partially grouted masonry assemblages. *Construction and Building Materials*, 83, 159 -173.

CSA Group. (2014). Annex B Temporary wind bracing of masonry during construction. In *CSA 371-14 Masonry construction for buildings* (p. 62). CSA Group.

Dassault Systemes Simulia Corp. (2011). 35.1.10 Surface-based cohesion behavior. In *ABAQUS/Standard User's Manual*, 6.11. Providence, RI.

Hodhigere, Y. J. (2018), "Finite Element Analysis-Base Approach for Stress Concentration Factor Calculation". *Lecture notes in Mechanical Engineering*,

MCAA. (2012). *Standard Practice for Bracing Masonry Walls Under Construction*. Algonquin: MCAA.

MIT. (2017). *Energy Balance*. Retrieved from <https://abaqus-docs.mit.edu/2017/English/SIMACAEGSARefMap/simagsa-c-qienergybal.htm>

MIT. (2017). *Mesh Convergence*. Retrieved from <https://abaqus-docs.mit.edu/2017/English/SIMACAEGSARefMap/simagsa-c-ctmmeshconverg.htm>

National Research Council Canada. (2015). 4.1.7 Wind Load. In *2015 National Building Code of Canada* (pp. 4-27 - 4-43). Ottawa.

4 Robust Crack Identification Technique for Masonry Structures

In recent decades, structural engineers have implemented various image processing (IP) and deep learning (DL) techniques (such as Convolutional Neural Network (CNN)) as a classification tool to automate the vision-based crack inspection of structures. In this chapter, a hybrid IP-CNN algorithm is proposed for the crack detection of masonry structures. The hybrid method implements CNN to locate sub-areas of images where the cracks appear, followed by an innovative IP technique to detect pixel-level damage. The architecture of CNN and IP algorithms are presented first, followed by the proposed technique, along with the image preparation technique and hyperparameter tuning. Lastly, a case study of a database of a masonry structure is presented to illustrate the validity and accuracy of the proposed technique.

4.1 Implementation of CNN

4.1.1 Basics of CNN

With the integration of Artificial Intelligence (AI) methods in structural health monitoring (SHM) techniques, machine learning (ML) and deep learning (DL) provide structural engineers (Avci *et al.* 2020) with an effective classification technique for 1D vibration measurements and 2D image datasets of cracks and various other types of anomalies such as corrosion, spalling, delamination, and fatigue-induced damages. The basic framework of any DL algorithms is to create a network that is trained on a large database and used to perform automated classifications. In general, the training accuracy is heavily dependent on the size of the database and can be conducted in a supervised, semi-supervised, or unsupervised manner depending on the labeling of the images. Comparing to traditional IP techniques (Mohan and Poobal 2018), ML has been heavily favored for image-based crack detection as they offer high robustness with the extraction of features from images regardless of environmental conditions such as background, wind, and lighting. However, these methods require a user to define appropriate features for classification. To address this challenge, the researchers have recently explored DL algorithms for data-driven damage detection in numerous publications (Azimi *et al.* 2020).

The basis of the DL techniques is rooted in animal biology, where images detected by the eye are conveyed to the brain through a network of neurons. These methods outperform the previous IP and ML techniques as it provides higher classification accuracy and does not require feature extraction; the extraction of key data points that accurately describe the dataset, in the preprocessing stage. DL architectures use layers containing multiple weighted filters to extract features from samples within datasets and predict the probability of each sample belonging to a pre-defined classification. One of the most prevalent types of these DL architectures is the convolutional neural networks (CNN). CNN uses various hidden layers to extract classification probabilities, whether damage occurs or not. Figure 4.1 shows typical layers of a CNN network for data such as image, video, and acceleration.

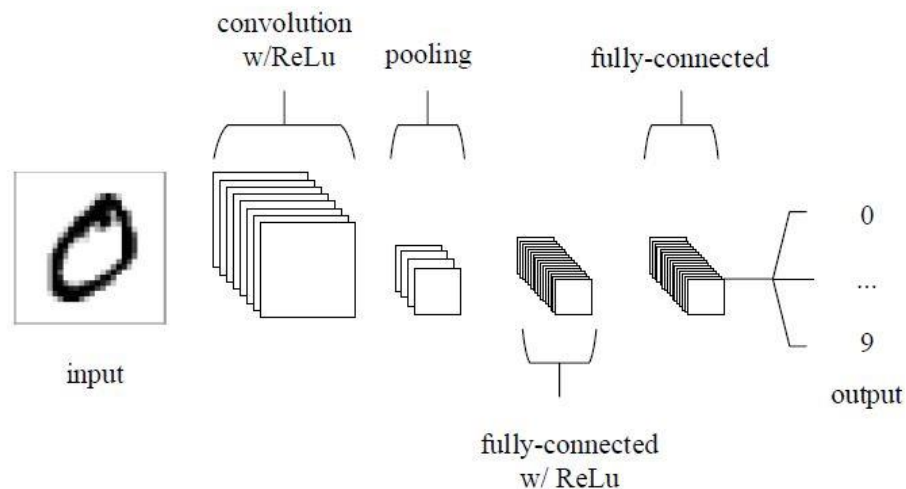


Figure 4.1: Schematic of a simple CNN architecture (O’Shea and Nash 2015).

Typically, the hidden layers are grouped into the following categories:

1. Convolutional layers
2. Batch normalization layers
3. Activation layers
4. Pooling layers

5. Dropout layers
6. Fully-connected layers
7. Softmax layers
8. Classification layers

The basis of all CNNs is the convolutional layer, which is a linear operation responsible for extracting features from input layers followed by an activation function. Convolution is a dot product of a kernel, small sub-set array of the input layer, with the corresponding input tensor to generate a feature or activation map (Yamashita *et al.* 2018). Each element of the feature maps represents a distinct activation of an artificial neuron. The convolutional filters can detect simple geometry such as edges to complex shapes indicative of distinct classifications depending on the depth of the network. The elements of these feature maps, however, are variable, with those features that have a range from 0 to 1 while others have a range from 1 – 100. Implementing batch normalization layers allows for the feature maps to be rescaled based on the variances of the training mini-batch. Previous studies have shown that the inclusion of normalization layers allows for decreased training time and is dependent on the mini-batch size, where smaller batch sizes are harder to normalize (Ren 2017). Regardless of whether normalization layers are used, activation layers proceed with all convolutional layers. These layers introduce nonlinearity into the layers, learning when activations occur for specific features based on a spatial location in the input data and activation function (O’Shea and Nash 2015). The most common activation function used is a rectified linear unit (ReLU); however, sigmoid and hyperbolic tangent functions have also been used in the literature.

Downsampling of the extracted features is conducted using the pooling layer. A sliding window moves over the extracted feature maps and quantifies a value that generalizes all activations within that window. The two most common pooling operations is max and average pooling, where the sliding window summarizes the activation elements based on the pre-defined mathematical operator. Downsampling of the extracted feature maps allows for the (1) reduction of the number of learnable features, (2) isolation of critical features,

and (3) variable input sizes (Yamashita *et al.* 2018). For both convolutional and pooling layers, the dimensionality of the output layers can be calculated using the following formula (Yamashita *et al.* 2018):

$$\frac{I - f + 2P}{S} + 1 \quad (4.1)$$

Where I is the input height or width, f is the height or width of the kernel in the convolutional or pooling layer, P is the number of zero paddings, and S is the stride of the kernel in the convolutional or pooling layer. For 2D data, the third dimension of the output and input sizes represents the number of filters (f_c).

Once the final convolutional and pooling layers occur, a fully connected (FC) layer is used to transform the 2D output layers into a 1D vector for prediction. In particular, for shallow neural networks such as the one presented in Figure 4.1, the number of nodes in the FC layers must be significantly high to obtain better performance (Basha *et al.* 2019). Lastly, a *softmax* layer is used to calculate the probabilities of each classification using a normalized exponential function, where the class with the highest probability (P_c) yields the classification result. However, one of the significant drawbacks of this methodology is the potential for the algorithm to overfit the training data. This occurs when the models extract information on particular features of the input rather than a generalizing over the entirety of the input data (Yamashita *et al.* 2018). As such, when classifying new datasets, the model will lose significant accuracy with respect to validation or testing. Increasing the datasets through data augmentation (as discussed in Section 4.3) and decreasing network complexity and batch normalization can help reduce this effect (O’Shea and Nash 2015, Ren 2017, Yamashita *et al.* 2018). Additionally, dropout layers can be added to CNN, which introduces a probability that an activation element may be set to 0 during training, which helps improve the generalization of the model.

4.1.2 Crack identification using the traditional CNN approach

In this study, a novel 29-layer CNN was proposed for the detection of cracks in masonry courses, as shown in Figure 4.2. Typically, the number of layers are originally assigned

arbitrarily and further adjusted based on the context of the study conducted and the required accuracy level needed. In this study, a sufficiently shallow network was chosen as the training database is sufficiently high. The selected network performed a binary classification of 2D greyscale masonry images to determine if there was a presence of a crack or not. To reduce the computational time and increase the size of the database, the masonry images were divided into 40 x 40 sub-images, as detailed in Section 4.3. Stochastic gradient descent with momentum (SGDM) optimizer was used as the solver for training the network. SGDM updates the gradient of the error function based on each weight and updates those weights that are in the “downhill” direction of the gradient. As this process is time-consuming, momentum was introduced, such that the modification of weight is dependent both on the current and previous gradients (Quan 1999). Though the popular CNN architectures such as *AlexNet* (Krizhevsky *et al.* 2017), *ZF Net* (Zeiler and Fergus, 2013), *VGG Net* and *GoogLeNet* (Szegedy *et al.* 2015) have exceptional accuracy, these networks require significant training data which is often not available in the structural engineering application and take relatively longer time to train on a state-of-the-art GPU. Table 4.1 provides details of the selected CNN architecture used for the current database.

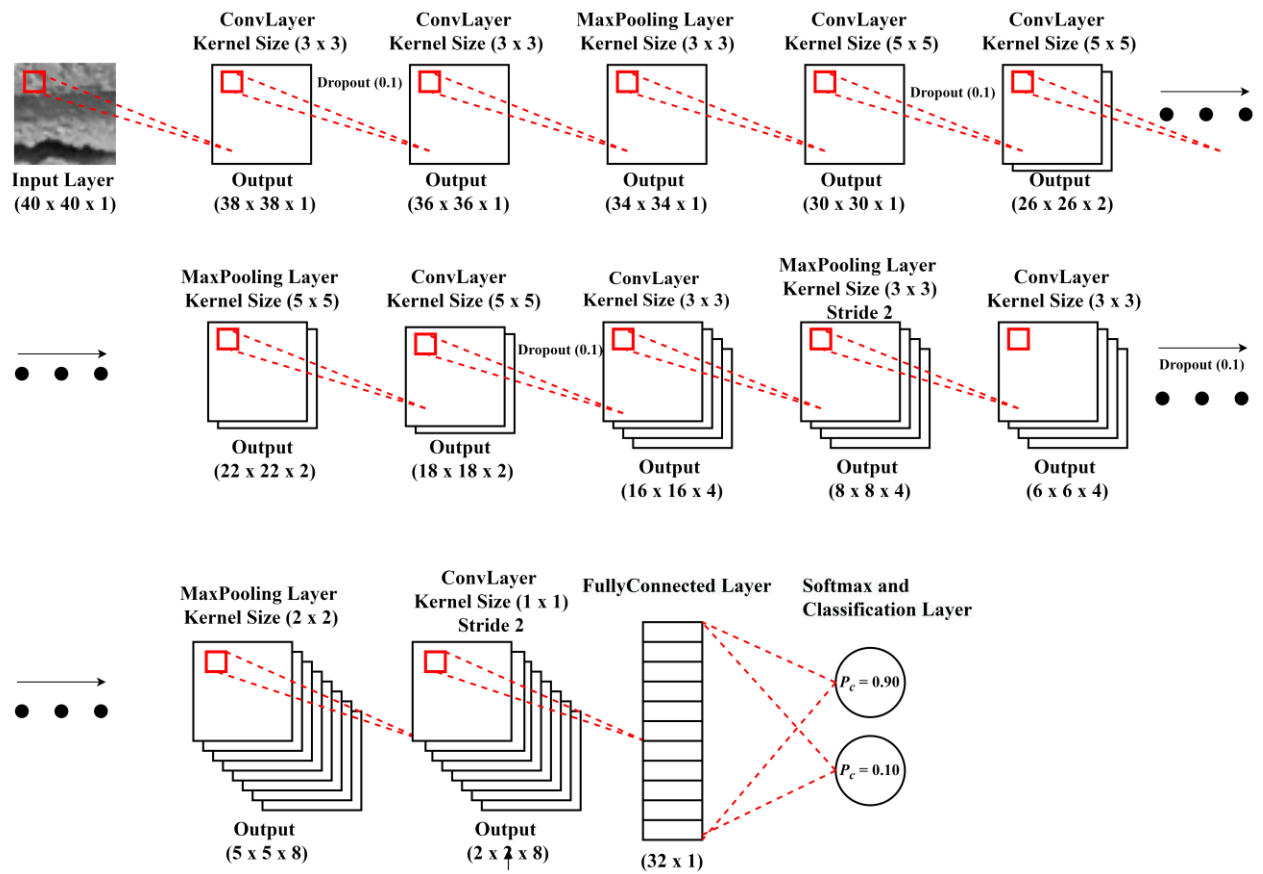


Figure 4.2: The proposed CNN architecture.

Table 4.1: Detailed description of the selected CNN layers.

Layer Name	Input Layer Size	f	S	P	f_c	Output Layer Size
<i>Image_input</i>	40 x 40 x 1	--	--	--	--	--
<i>Conv_1</i>	40 x 40 x 1	3 x 3	1	0	1	38 x 38 x 1
<i>Batchnorm_1</i>	38 x 38 x 1	--	--	--	--	--
<i>Relu_1</i>	38 x 38 x 1	--	--	--	--	--
<i>Dropout_1</i>	10% Dropout					
<i>Conv_2</i>	38 x 38 x 1	3 x 3	1	0	1	36 x 36 x 1
<i>Maxpool_1</i>	36 x 36 x 1	3 x 3	1	0	1	34 x 34 x 1
<i>Conv_3</i>	34 x 34 x 1	5 x 5	1	0	1	30 x 30 x 1
<i>Batchnorm_2</i>	30 x 30 x 1	--	--	--	--	--
<i>Relu_2</i>	30 x 30 x 1	--	--	--	--	--
<i>Dropout_2</i>	10% Dropout					
<i>Conv_4</i>	30 x 30 x 1	5 x 5	1	0	2	26 x 26 x 2
<i>Maxpool_2</i>	26 x 26 x 2	5 x 5	1	0	2	22 x 22 x 2
<i>Conv_5</i>	22 x 22 x 2	5 x 5	1	0	2	18 x 18 x 2
<i>Batchnorm_3</i>	18 x 18 x 2	--	--	--	--	--
<i>Relu_3</i>	18 x 18 x 2	--	--	--	--	--
<i>Dropout_3</i>	10% Dropout					
<i>Conv_6</i>	18 x 18 x 2	3 x 3	1	0	4	16 x 16 x 4
<i>Maxpool_3</i>	16 x 16 x 4	3 x 3	2	0	4	7 x 7 x 4
<i>Conv_7</i>	7 x 7 x 4	3 x 3	1	0	4	5 x 5 x 4
<i>Batchnorm_4</i>	5 x 5 x 4	--	--	--	--	--
<i>Relu_4</i>	5 x 5 x 4	--	--	--	--	--
<i>Dropout_4</i>	10% Dropout					
<i>Conv_8</i>	5 x 5 x 4	2 x 2	1	0	8	4 x 4 x 8
<i>Maxpool_4</i>	4 x 4 x 8	1 x 1	2	0	8	2 x 2 x 8
<i>Dropout_5</i>	75% Dropout					
<i>Fully Connected Layer</i>						
<i>Softmax Layer</i>						
<i>Classification Output</i>						

4.1.3 Image Preparation

An image database was generated containing two classes of images of (a) 7800 cracked masonry, and (b) 7800 uncracked masonry and various testing equipment for the training, validation, and testing of the selected CNN architecture. Images with a size of 1440 x 1440 RGB of cracked masonry walls, as shared by Dr. Sreekanta Das of the University of Windsor, were converted to the grayscale intensity and segmented into 40 x 40 x 1 sub-

images, as shown in Figure 4.3. The segmented images were then sorted into two separate classes labeled as ‘damaged’ and ‘undamaged’ depending on whether the sub-images contained masonry cracks or not from visual inspection conducted by the author. The “true” classifications of the images were generated based on the label of the folders that contained the separated classes. However, as the masonry cracks only composed a minimal percentage of the sub-images that composed the original image, the training data classifications were severely imbalanced. If imbalanced databases are used to train the CNN network, overfitting may occur, where the network only learns to detect the features specific to the training database rather than the general features that could be used to detect the classification. Data augmentation (Bjerrum *et al.* 2017) can be used to manipulate existing images by adding random variations to enhance the training database and prevent overfitting. The existing images were mirrored horizontally and vertically in addition to manipulating the contrast to augment the existing ‘damaged’ training database such that each original image resulted in nine **new** augmented images, as shown in Figure 4.4.

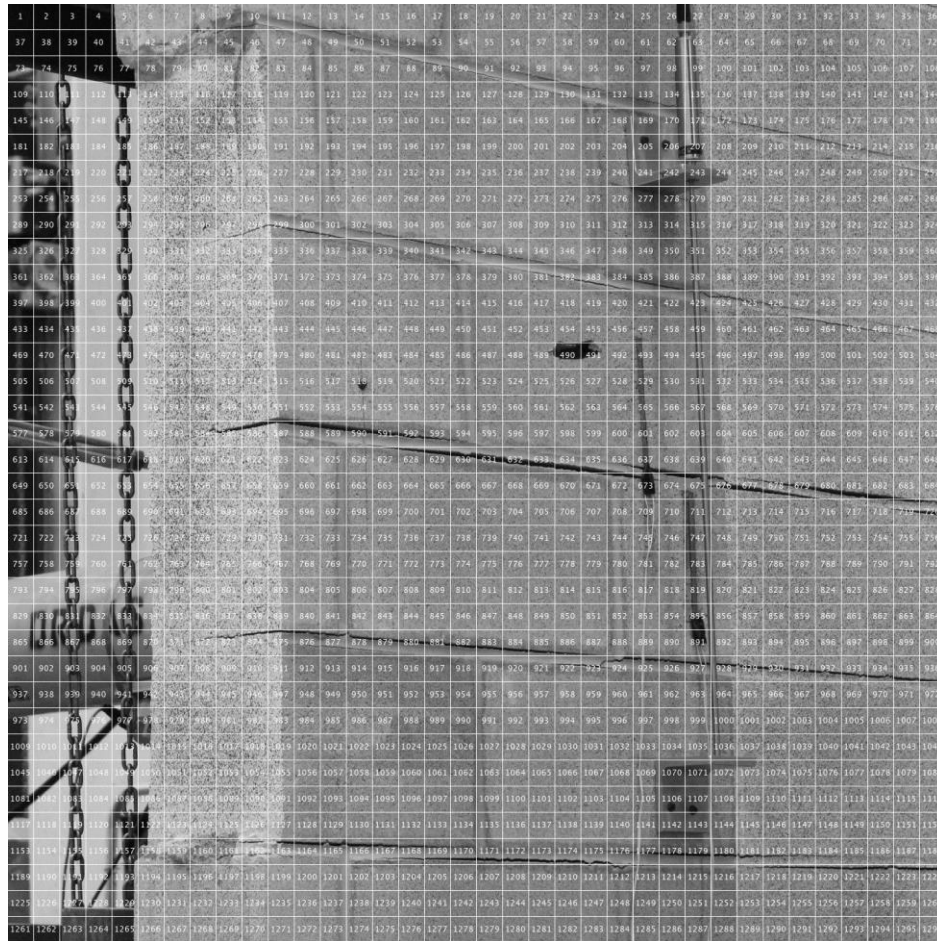


Figure 4.3: Segmented grayscale image for the creation of the training database.

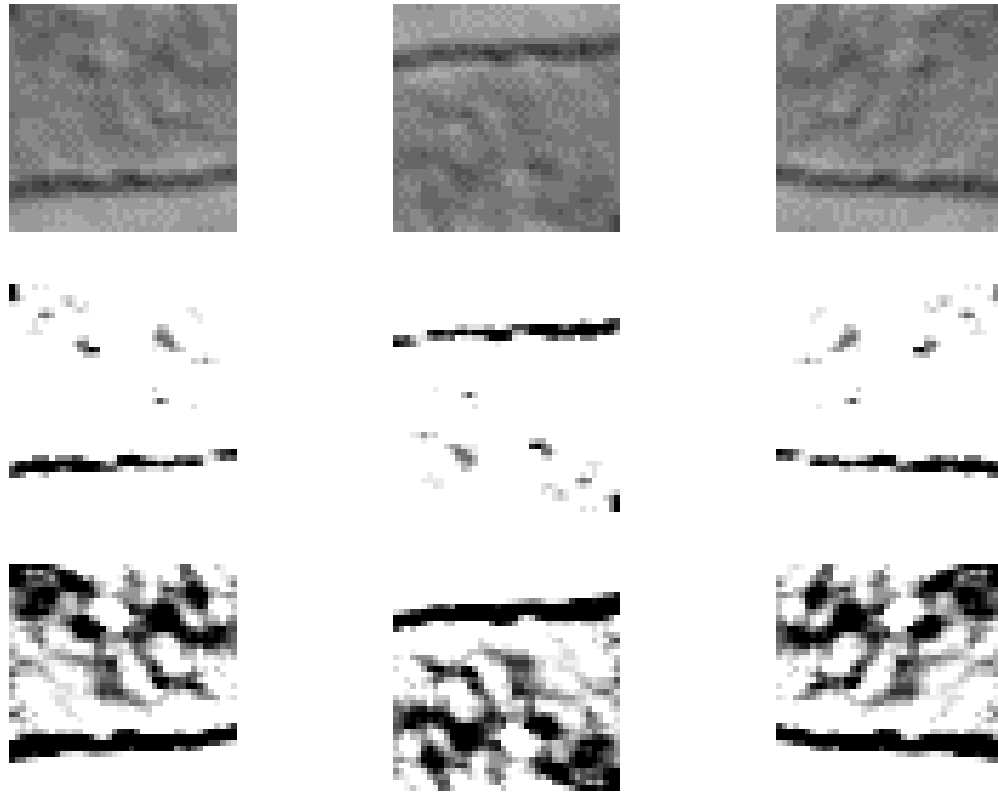


Figure 4.4: Data augmentation of the training database of the damaged specimens.

4.1.4 Performance evaluation of the CNN technique

The split for the training, validation and testing datasets was 70%, 25%, and 5%, respectively, from the 7800 images generated. The initial training, validations, and testing accuracies were determined through confusion matrices generated after completion of the testing dataset. From Figure 4.5, the accuracy for each respective category was calculated using the following equation:

$$Accuracy = \frac{TP + TN}{TP + FP + FN + TN} \quad (4.2)$$

True Class	Damaged	19	8
	Undamaged	7	46
		Damaged	Undamaged
		Predicted Class	

Figure 4.5: Confusion matrix of the testing data.

Where TP is the true positive reading for damage where predicted classification equals the true classification, TN is the true negative reading for non-damage where predicted classification equals the true classification, FP is the false positive reading for non-damage where the predicted classification does not equal the true classification, and FN is the false negative reading damage where the predicted classification does not equal the true classification. For example, the accuracy determined from the confusion matrix for trial 3; consisting of 80 test images, of Table 4.2 in Figure 4.5 was calculated as follows:

$$Accuracy = \frac{TP + TN}{TP + FP + FN + TN}$$

$$Accuracy = \frac{19 + 46}{17 + 7 + 8 + 53}$$

$$Accuracy = 0.813$$

The initial training, validation, and testing accuracy were taken as the average over five trials to account for minor fluctuations in the accuracy over various training trials, as shown

in Table 4.2. Hyperparameter tuning, as summarized in Section 4.4, was used to improve the accuracies of the CNN classification.

Table 4.2: Initial accuracy of the selected CNN architecture.

Trial #	1	2	3	4	5	Average
Training accuracy (%)	84.8	93.4	85.2	80.5	77.7	84.3
Validation accuracy (%)	80.1	86.9	83.9	85.2	77.7	82.8
Testing accuracy (%)	83.8	92.5	81.3	95.0	41.2	78.8
Training duration (s)	1326	1310	1309	1323	1299	1313

4.2 Hyper-parameter Tuning

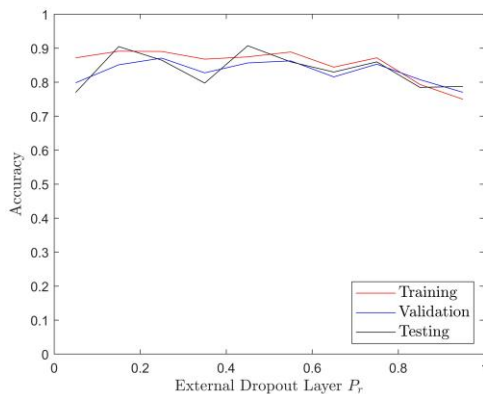
In CNN, different parameters contribute to the overall classification accuracy of the network. Broadly, these parameters can be classified into two categories, (1) those parameters that describe the architecture of the network defined as ‘*Network Parameters*’ and (2) those parameters that define how the architecture learns features from training data defined as ‘*Training Parameters*’. The variation of the parameters can increase, decrease, or have no effect on the training, validation, and testing accuracy of the algorithm. Therefore, hyper-parameter tuning (Aszemi and Selvam 2019) is implemented to optimize the network and training parameters of the algorithm to obtain the best accuracy across all classification categories. Various methods have been developed by the researchers to autonomously determine the optimal network and training parameters such as hybrid genetic algorithms (Aszemi and Selvam 2019), parameter-setting free harmony search (Lee *et al.* 2018) and random search (Bergstra and Bengio 2012). Furthermore, network and training parameters can be optimally tuned by varying one parameter and recording the effect on the overall training, validation, and testing accuracy. For this study, two network parameters and five training parameters were hyper-tuned to achieve an optimized accuracy for the detection of masonry cracks. Ten sample values were chosen to investigate the variation of training, validation, and testing accuracy with each hyperparameter.

Figure 4.6 (a-g) shows the variation in training, validation, and testing accuracy with the hyper-tuned parameters. For network parameters, the probability rate (P_r) of the internal and external dropout layers was investigated. The internal dropout layers are those that occur between convolutional layers or max-pooling layers, while the external dropout

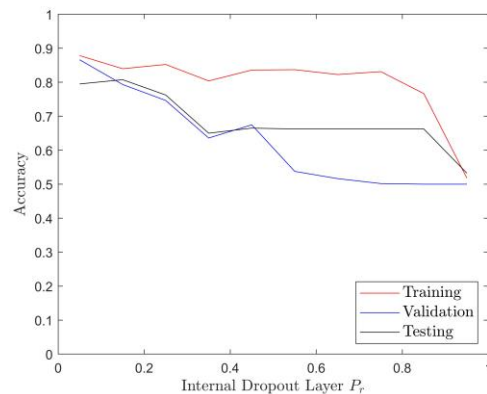
layers occur before the FC layer. For the external drop out layer P_r , the trend of the training, validation, and the testing accuracy is that they decrease with increasing probability rate, as shown in Figure 4.6 (a). Moreover, at low P_r , there are significant differences between the training, validation, and testing accuracies, indicating that the model is overfitting the images during training. This is because as P_r increases, more features are ‘turned off’ and do not contribute to the classification of the images resulting in lower accuracy. Additionally, the more features that are used to classify the image, the less generalized the classification becomes, resulting in overfitting during the testing stage. Therefore, a P_r of 0.75 was chosen as it improved the accuracy across all categories when compared to the original network without causing overfitting to occur. Similarly, for the P_r of the internal dropout layers, the training, validation, and testing accuracies decrease significantly with increasing probability, as shown in Figure 4.6(b). This is because the higher the probability, the more features that are ‘turned off’ during training resulting in the algorithm being unable to determine which features are excited when a classification is present.

For training parameters, the momentum, L_2 regularization (L_2R), learn rate drop factor (LRDF), mini-batch size (MBS), an initial learning rate (ILR) were hyper-tuned. Momentum, as described in Section 4.1.2 is increased with the increase in the training, validation, and testing accuracies, as shown in Figure 4.6 (c). This is because, at higher momentums, the updated weights of the error function are based more heavily on the previous accurate gradients rather than the current erroneous gradients, which results in the network arriving at the optimal error function quickly. L_2R or weight decay is a parameter that forces the sum of squares of all features’ weights of the loss function to become relatively small (Ng 2004). As the L_2R increases, the training, validation, and testing accuracy decreased, as shown in Figure 4.6 (d). This is due to the increased loss as a result of the addition of a significant portion of the feature weights being added to the loss function. LRDF is a factor applied to the learning rate of the network after a set number of epochs has occurred. From Figure 4.6 (e), it can be observed that there is no significant correlation between the learning rate drop factor and the training, testing, and validation accuracy. This lack of correlation is believed to be due to the fact the learning rate drop factor is only applied twice during training and, therefore, does not have a significant effect on the accuracy of the network.

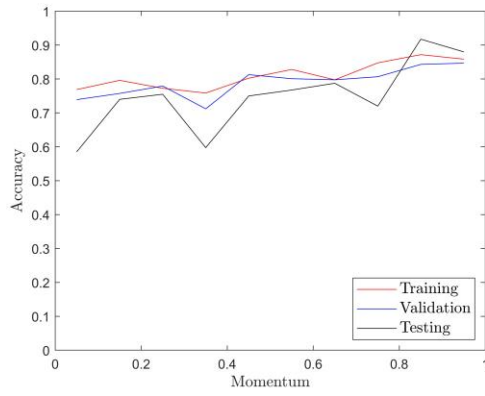
The MBS is the size of the subset of the training data used during each iteration to update the weights and evaluate the gradients of the loss function. At small MBS, the network requires more time to train as the mini-batch is a small fraction of the entire training dataset. The small MBS also implies that the feature extraction is based on a less representative selection for the classification, and therefore there is a tendency for overfitting to occur. For high MBS, network training takes less time, and the samples are more representative of general features of the classification, reducing overfitting; however, large batch sizes are also limited to the number of GPUs a computer has (Nabi 2019). Figure 4.6 (f) shows the variation of training, validation, and testing accuracy with respect to MBS. Lastly, the ILR is hyper-tuned with respect to training, validation, and testing accuracy. The initial learning rate is the rate by which the networks learn the feature weights for image classification. If the learning rate is too low, overfitting occurs due to the lack of generalization of the features, while if the learning rate becomes too large, the training does not properly converge. Figure 4.6 (g) shows the variation of the initial learning rate with respect to training, validation, and testing accuracy. Table 4.3 shows the variation of these hyperparameters from the original network. The hyper-tuned network has training, validation, and testing accuracy of 88.67%, 86.68%, and 89.00%, respectively, which is higher than the original accuracies presented in Table 4.2.



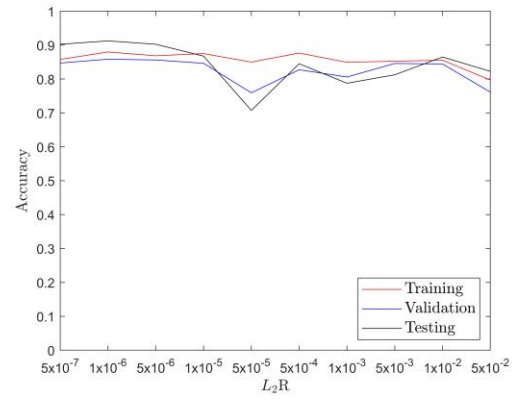
(a)



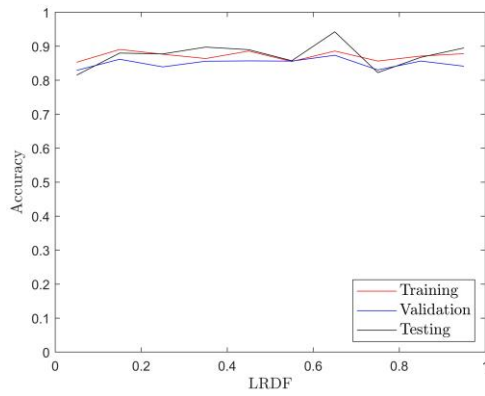
(b)



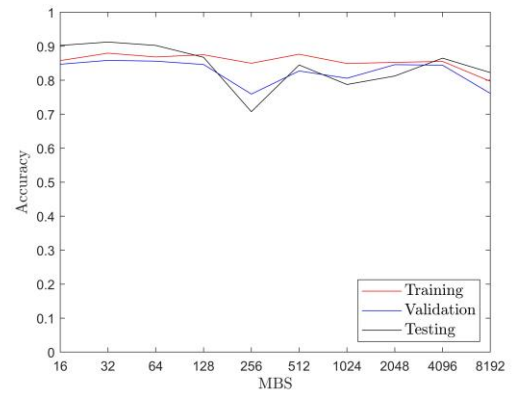
(c)



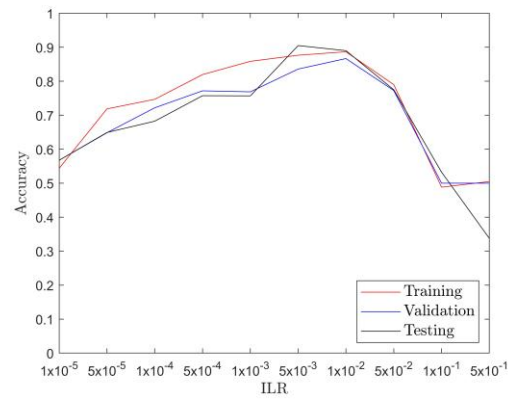
(d)



(e)



(f)



(g)

Figure 4.6: Variation of training, validation and testing accuracy with (a) external dropout layer P_r , (b) internal dropout layer P_r , (c) momentum, (d) L_2R , (e) LRDF, (f) MBS and (g) ILR.

Table 4.3: Hypertuning of the network and training parameters.

Parameter	Original Algorithm	Hypertuned Algorithm
External dropout layer P_r	0.9	0.75
Internal dropout layer P_r	0.1	0.1
Momentum	0.9	0.95
L_2R	0.0001	0.00001
LRDF	0.1	0.15
MBS	128	64
ILR	0.01	0.01

4.2.1 Shortcomings of Standalone CNN technique

Though CNN has an excellent potential to classify 2D images based on the extracted features, significant preprocessing is required to establish and label an image database. Furthermore, depending on the size of the image, CNN takes a longer time to extract the features needed for classification. Additionally, unless training is conducted at a pixel level, CNN can only determine which images have damage, not the location of the damage within the image. Therefore, a standalone CNN may not be suitable for SHM of early-age masonry structures at construction sites where damage can happen rather quickly.

4.3 The Proposed Hybrid Crack Identification Technique

In the past, IP techniques (Mohan and Poobal 2018) have been substantially researched for the detection of cracks in large-scale structural systems. These techniques involve the segmentation of images using filters such as the Otsu's (Otsu 1979) or Sobel-Feldman Operator (Sobel 2014), wavelet transformation techniques such as Haar (Haar 1910), edge detectors (Canny 1986), or other binarization or thresholding techniques, offering a fast computational analysis of images for crack detection. However, they are often susceptible

to environmental factors such as lighting, requiring images with high resolution. They are also unable to provide any physical description of the crack, such as length, width, and depth (Mohan and Poobal 2018), and are typically not as accurate as ML or DL techniques. Additionally, most of the research conducted on IP, ML, or DL algorithms are used primarily for the post-assessment of damaged structures. In this section, a novel IP technique using image thresholding based on matrix density is described.

For a given early-age masonry structure after initial construction at $t = 0$, an image was taken to represent the ‘undamaged’ condition of the structure, as shown in Figure 4.7 (a). 40 x 40 x 1 sub-images and converted to greyscale images where the range of color for each pixel is between 0 (black) to 255 (white) as shown in Figure 4.7 (b). The images were also resized such that the number of pixels along the height and width of the image are equivalent. As such, an image with a resolution of $n \times m$, where n is the height and m is the width of the image, can be represented as an $n \times m$ 2D matrix where each element of the matrix represents the pixel color from 0 – 255.

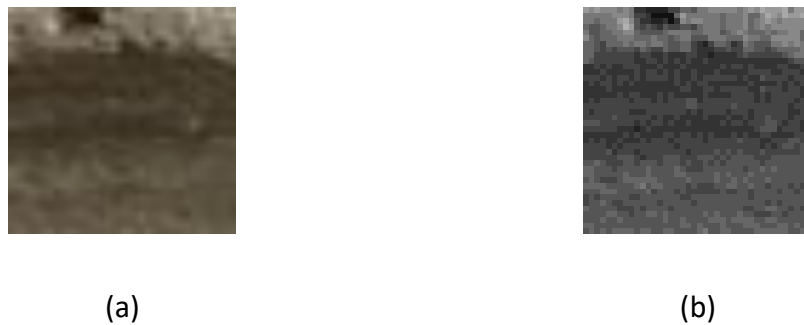


Figure 4.7: (a) RGB, and (b) greyscale image of an undamaged masonry surface.

At an instance of time $t > 0$, damage occurs to the structure, and an image is taken to represent the ‘damaged’ condition of the structure at that time instance, as shown in Figure 4.8 (a). This image was taken at the exact location where the original ‘undamaged’ image was taken. Due to the absence of available images of progressive damage of masonry structures, the commercially available GNU image manipulation program *GIMP 2.10.20*

was used to simulate the images of progressive cracks of two-course undamaged masonry prisms taken from the experiments outlined in Chapter 2 by photoshopping cracks. The assumption is that this algorithm will be used for the continuous monitoring of structures where previous methods have focused primarily on discrete post-damage assessments. The damaged image was resized such that it had square dimensions and converted into a greyscale image, as shown in Figure 4.8 (b). As a result, two separate image matrices were created (1) the undamaged image matrix at $t = 0$ (\mathbf{U}) and (2) the damaged image matrix at $t > 0$ (\mathbf{D}) containing $n \times n$ elements with a range of 0 to 255.



Figure 4.8: RGB (a) and greyscale (b) image of damaged masonry.

Upon the formation of a crack, those pixels belonging to the crack would be consistent with elements whose value was approximately zero and would vary significantly when compared to pixel values in \mathbf{U} with the same spatial orientation. Those elements that experienced no cracks, therefore, would remain approximately between \mathbf{U} and \mathbf{D} with slight variations occurring due to the variations in environmental factors. Therefore, a threshold matrix (\mathbf{T}) was determined from the following equation:

$$\mathbf{T} = |\mathbf{U} - \mathbf{D}| \quad (4.3)$$

The threshold matrix represents the differences between the brightness of the pixels between undamaged and damaged images. There is a potential range for any element of \mathbf{T} to be between 0, where no change has occurred, and 255, where the brightness has changed from black to white. Therefore, \mathbf{T} can be used to locate the damage at a pixel level by setting a threshold value (TH) that is within the range of \mathbf{T} . The damage localization matrix

(\mathbf{L}) can be solved by assessing the following conditions for each element of threshold matrix:

$$\mathbf{L}(n, n) = \begin{cases} 255, & \mathbf{T}(n, n) > TH \\ 0, & \mathbf{T}(n, n) \leq TH \end{cases} \quad (4.4)$$

For a TH approximately equal to zero, \mathbf{L} assumes the majority of the elements represent cracking, as shown in Figure 4.9(a). Those elements that have only slight variation due to the presence of environmental noise in addition to those elements that are cracked in the images are considered to be cracked elements. Therefore, significant noise is present at low TH , and the accuracy of the algorithm to identify the true crack is low. As the TH value increases, the noise from the environmental factors is gradually filtered out until the true cracked elements dominate the \mathbf{L} matrix, as shown in Figure 4.9(b). However, as the TH value continues to increase, those cracked elements are no longer considered cracked because they do not satisfy the conditions in Equation 4.4. Therefore the ‘true’ crack is filtered out. Moreover, this results in extremely low accuracy for crack detection, as demonstrated in Figure 4.9(c).



(a)

(b)

(c)

Figure 4.9: Variation of damage localization with (a) low TH , (b) average TH , and (c) high TH .

Once a threshold value was chosen, the cracked output image matrix (\mathbf{CR}) can be constructed from the following conditions using the damage localization matrix:

$$\mathbf{CR}(n, m) = \begin{cases} \mathbf{L}(n, n), & \mathbf{L}(n, n) = 255 \\ \mathbf{D}(n, n), & \mathbf{L}(n, n) = 0 \end{cases} \quad (4.5)$$

The cracked output image matrix was then converted back into an RGB image where the located pixel-level damage was highlighted in green, as shown in Figure 4.10.

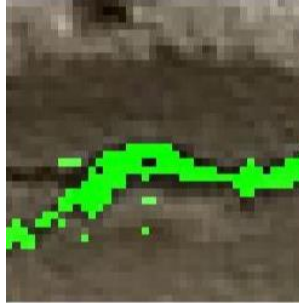


Figure 4.10: Crack detection using the proposed image-thresholding method.

4.3.1 Determination of optimal threshold

As demonstrated above, an optimal TH value must be chosen such that the majority of the low-level noise is filtered out without removing those elements that are cracked. To determine the optimal TH , the variation of the matrix density with respect to TH was investigated. Matrix density (ρ_m) is a value representing the percentage of elements contained within a matrix that are non-zero elements as represented by:

$$\rho_m = \frac{\sum_{i=1}^n \sum_{j=1}^m d_{nm}}{A_{mat}} \quad (4.6)$$

Where A_{mat} is the spatial area of the matrix, which is the product of the dimensions of the matrix, and d_{nm} is an element of the matrix d with position n and m . Furthermore, it is assumed that those elements that are considered cracked are the ‘dense’ elements, as shown in the binary condition below:

$$\mathbf{d}(n, m) = \begin{cases} 1, & \mathbf{T}(n, m) > TH \\ 0, & \mathbf{T}(n, m) \leq TH \end{cases} \quad (4.7)$$

Therefore, the ρ_m changes proportional to the change in TH , as shown in Figure 4.11. As the TH value increases, fewer elements contained within the L matrix are considered ‘cracked’; therefore, the matrix density decreases. This occurred rapidly initially as the low-level noise is filtered out and gradually tapered off as fewer elements are filtered out

at high TH values. Moreover, this resulted in a pseudo-exponential relationship between ρ_m and TH that can be quantified through nonlinear regression. Therefore, once an optimal TH value was chosen, the optimal matrix density ($\rho_{o,m}$) could also be quantified. However, it was expected that there would be significant variations of the exponential model coefficients and range of TH between various cracked images due to the spatial and geometric nonuniformity of cracking. As such, a normalization factor was calculated for each equation such that the area under the graph is equivalent to unity:

$$N_o^2 \int_{\min(TH)}^{\max(TH)} A^2 e^{2C(TH)} dTH = 1 \quad (4.8)$$

Where N_o is the normalization factor, A and B are the coefficients of exponential regression, as shown in the equation. Solving the integration, the normalization factor became:

$$N = \sqrt{\frac{2C}{A^2(e^{2C*\max(TH)} - e^{2C*\min(TH)})}} \quad (4.9)$$

Therefore, it was hypothesized that a relationship could be established between the normalization factor of the pseudo-exponential curve and the optimal matrix density.

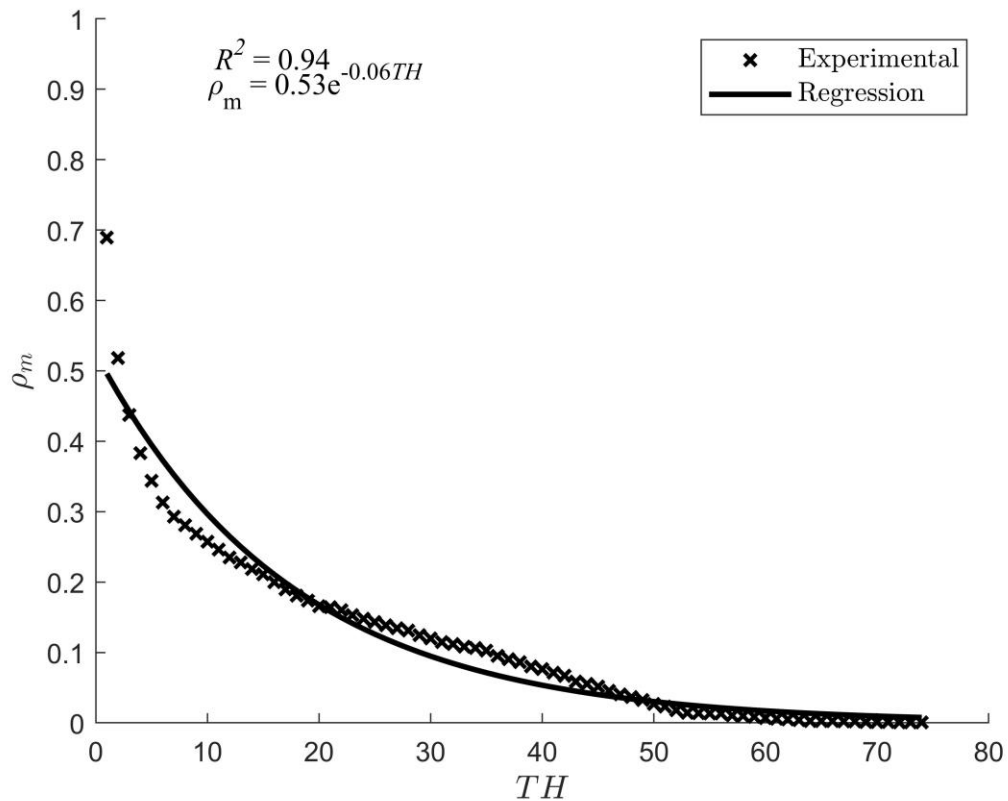


Figure 4.11: Variation of matrix density with the threshold value.

With the relationship between ρ_m and threshold values established, a metric was chosen to determine the optimal threshold and matrix density values that will most accurately locate the crack. Confusion matrices were used to determine the accuracy of the proposed IP technique for crack detection. This technique requires an established benchmark where the crack location is highlighted by an expert engineer. The true ‘crack’ location was highlighted by changing those pixels that were cracked to white (grayscale intensity = 255) using *GIMP 2.10.20*. Figure 4.12 shows the true crack region highlighted at the pixel level by postprocessing of the images, as discussed in Section 4.3.

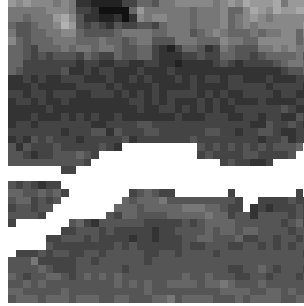


Figure 4.12: True classification of the cracks in the masonry prism.

Comparing Figure 4.12 to the one shown in Figure 4.10, the positive and negative correlations, as well as the confusion matrix, can be determined. However, this particular binary classification is ill-conditioned; there are significantly more pixels that are undamaged compared to those that are damaged. As such, there is a tendency for performance metrics, such as accuracy, derived from confusion matrices to yield misleading results as they are heavily influenced by the classification with the larger sample size (Boughorbel *et al.* 2017). Therefore, Matthew's Correlation Coefficient (MCC) (Matthews 1975) was used to measure the quality of the correlation between predicted and true values for binary classification. MCC has a range of $-1 < MCC < 1$ where 1 represents a perfect prediction, 0 represents no better than a random prediction, and -1 represents no prediction at all. The MCC value can be calculated using the following equation (Matthews 1975):

$$MCC = \frac{TP \cdot TN - FP \cdot FN}{\sqrt{(TP + FP)(TP + FN)(TN + FP)(TN + FN)}} \quad (4.9)$$

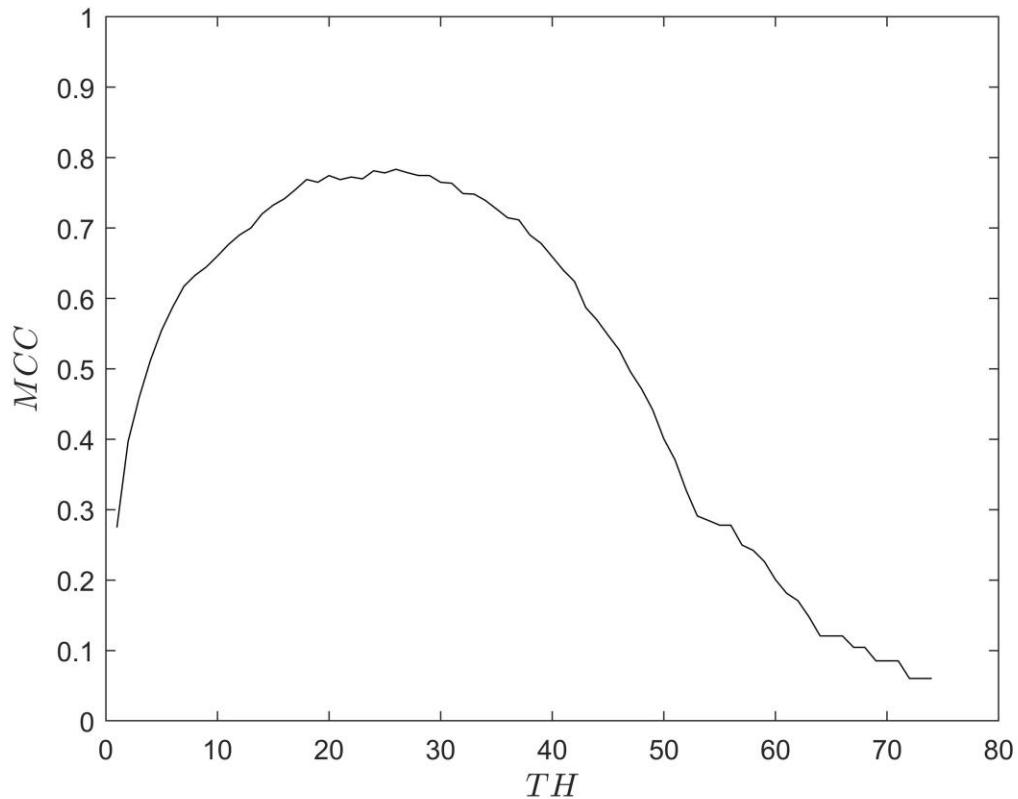


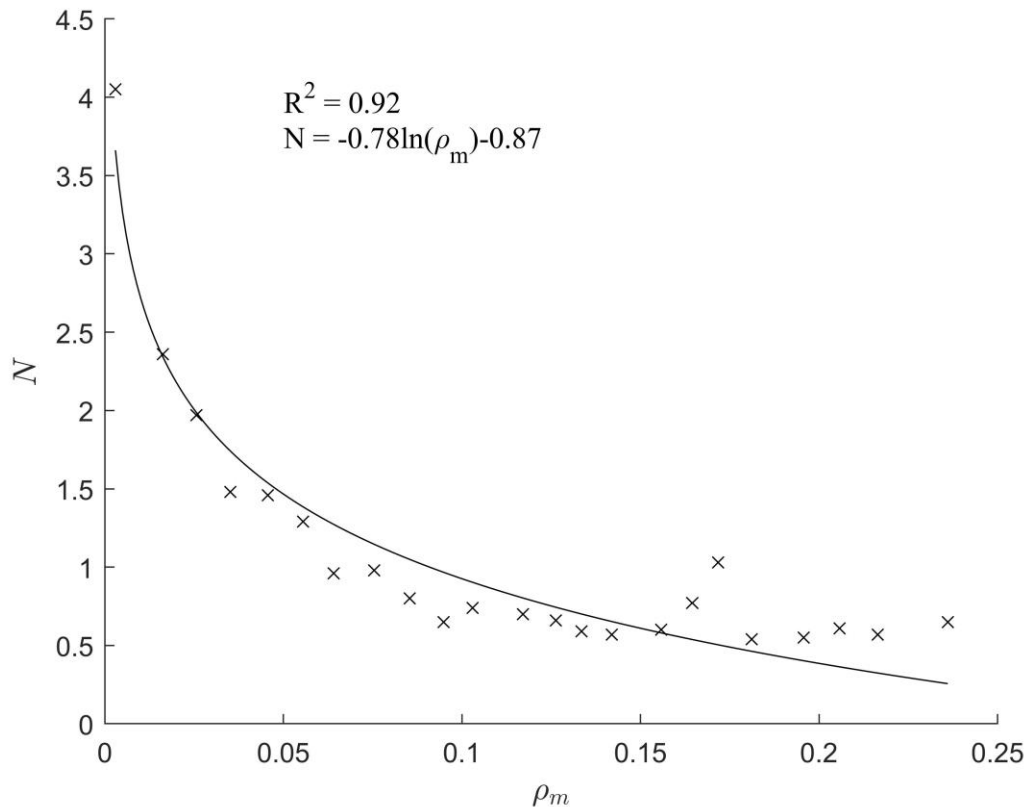
Figure 4.13: Variation of MCC with TH for determining optimal TH .

Therefore, for each TH the MCC was calculated, and a curve was established as depicted in Figure 4.13. It can be observed that the optimal TH occurs when the correlation between prediction and true classification is high, where MCC is a maximum. From the optimal TH , the $\rho_{o,m}$ was determined and correlated with the normalization factor of the pseudo-exponential fit. One hundred different cracked samples with varying size and orientation were analyzed to establish a correlation between the optimal matrix density and the normalization factor of the exponential equation. Table 4.4 summarizes the average of the performance indicators over the testing. Overall, the MCC and accuracy of the algorithm are significantly high, with low variance proving the robustness of the model to detect cracks of varying size and orientation. Additionally, the exponential fit showed a significant correlation over all samples proving that for cracks, ρ_m varies exponentially with TH for the proposed grayscale images.

Table 4.4: Statistical results obtained from the IP.

Parameter	Maximum <i>MCC</i>	Accuracy at maximum <i>MCC</i>	R^2
Average	0.86	0.97	0.91
COV	13.3%	2.7%	7.9%

The optimal matrix densities and normalization factors were clustered and averaged based on 1% ranges in the optimal matrix density from creating 23 bins from 0 to 23%. The average optimal matrix densities and normalization factors were plotted against each other, and a statistically significant correlation was determined, as shown in Figure 4.14.

**Figure 4.14: Variation of N with ρ_m .**

Establishing this correlation was done to remove the need for the optimization of the *TH* directly from the *MCC* value, which is time-consuming. Instead, the optimum *TH* can be determined from the optimal density value based on the calculated normalization factor from the data. Therefore, the steps of the proposed IP model are as follows:

1. Import a 40 x 40 undamaged image at $t = 0$ s and convert it to a greyscale undamaged image matrix (\mathbf{U}).
2. Import a 40 x 40 damaged image at $t > 0$ s and convert it to a greyscale damaged image matrix (\mathbf{D}).
3. Determine the threshold matrix \mathbf{T} from Equation 4.3.
4. For a TH range of $\min(\mathbf{T}) < TH < \max(\mathbf{T})$, determine the variation of the matrix density (ρ_m) with TH .
5. Determine the exponential model for the variation between ρ_m with TH , as shown in Figure 4.11, and calculate the normalization factor (N).
6. Use N to determine the optimal matrix density from the correlations shown in Figure 4.14.
7. From the optimal matrix density, use the exponential model to determine the optimal TH .
8. Use the optimal TH to determine the damage localization matrix (\mathbf{L}) and cracked output image matrix (\mathbf{CR}) as per Equations 4.4 and 4.5.
9. Convert \mathbf{CR} into a 40 x 40 RGB image where the pixel-level cracks are highlighted in green.

4.3.2 Proposed Hybrid Method

To address the challenges summarized in Sections 4.2.1 and 4.3 for standalone DL and IP techniques, an IP-driven hybrid CNN technique is proposed for the detection of cracks in early-age masonry structures with the flowchart illustrated in Figure 4.15. For continuous monitoring of structures under construction, DL techniques may not be efficient enough to promptly discern the localization of cracks in a timely matter such that those damages could be addressed before the failure occurs. Similarly, IP techniques are not entirely accurate with the detection of cracks over an entire image. Therefore, by using a DL technique to determine sub-images that have damage and a novel IP to accurately discretize those pixels that contain the damage, an accurate crack detection technique is proposed.

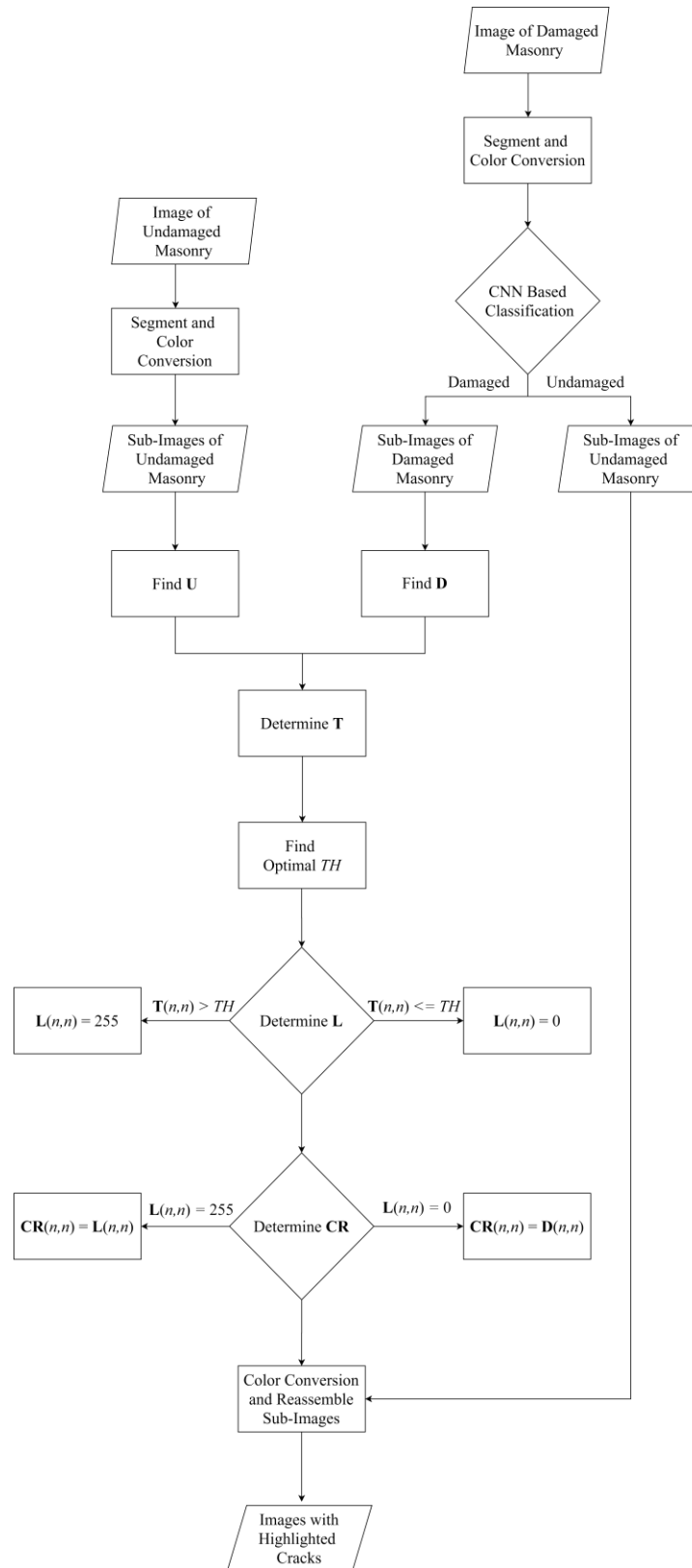
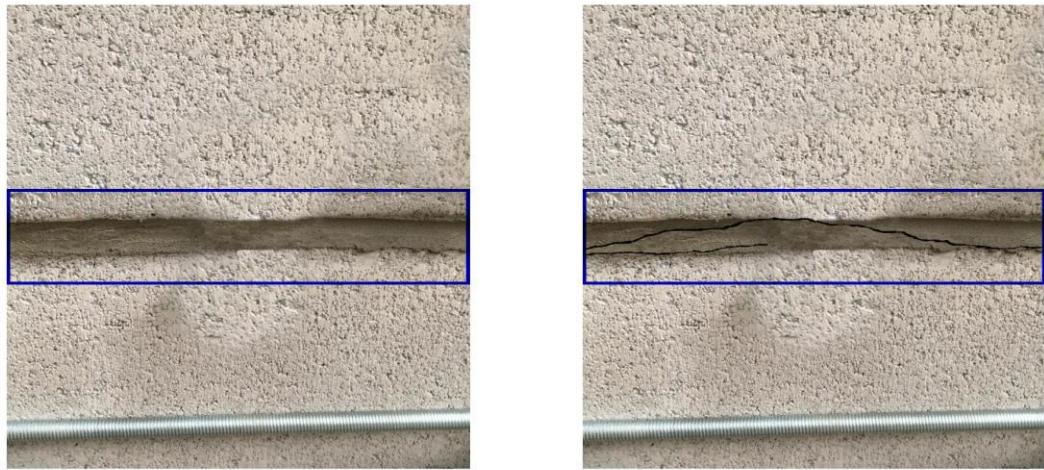


Figure 4.15: Flowchart of the proposed hybrid method.

4.3.3 Results and discussions

To validate the proposed technique, a simulation was conducted using a photoshopped damaged image created by *GIMP 2.10.10* and an original image, as shown in Figure 4.16. The original images were resized such that they have square dimensions; in this instance, the images are resized to 800 x 800. The sub-images of sizes 40 x 40 x 3 were taken from the damaged area highlighted in blue and converted to grayscale to create a database to be classified by CNN. The whole image was not used in the classification problem as it would create an ill-conditioned problem where the undamaged images far exceed the damaged sub-images. Furthermore, this would cause inaccuracies with the overall classification of these images by the DL network. Once the database was created, the images were classified using the pre-trained CNN network. Those sub-images that were correctly classified, either truly damaged or undamaged, are highlighted in blue while those that are incorrectly identified are highlighted in red, as shown in Figure 4.17. Damaged images that have been identified are then processed by the IP technique to determine the location of pixel-level damage. For each damaged sub-image, the normalization factor of the exponential equation representing the variation of matrix density and threshold value is calculated using step 5 of section 4.2. From the resulting normalization factor, the optimal density was determined using the equation in Figure 4.14, and the optimal threshold value was back-calculated from the exponential regression of step 6 to 7 of section 4.3.1, localizing the pixel level damage. Table 4.5 shows the values calculated for steps 5-9 of the proposed technique for all images classified as damaged.



(a)

(b)

Figure 4.16: A sample test image (a) undamaged, and (b) damaged state.

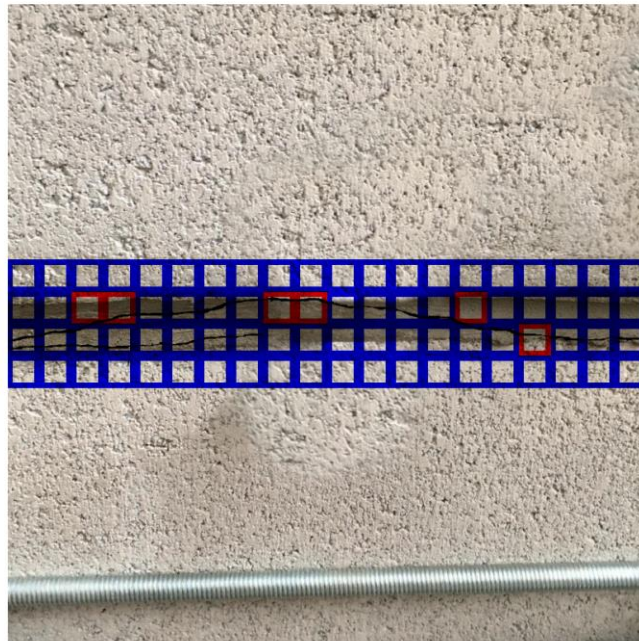


Figure 4.17: Classification of the sub-images by CNN.

Table 4.5: Algorithm parameters for pixel-level masonry crack detection.

Image #	A	B	Minimum TH	Maximum TH	N	Optimal ρ_m (%)	Optimal TH
1	0.25	-0.03	1.00	128.00	0.93	9.92	36
2	0.24	-0.04	1.00	95.00	1.18	7.24	32
3	0.31	-0.04	1.00	79.00	0.88	10.58	30
4	0.23	-0.05	1.00	76.00	1.39	5.50	31
5	0.27	-0.03	1.00	123.00	1.03	8.72	31
6	0.27	-0.02	1.00	90.00	1.17	7.29	28
7	0.26	-0.02	1.00	124.00	0.94	9.88	35
8	0.22	-0.03	1.00	121.00	0.95	9.73	39
9	0.47	-0.03	1.00	152.00	0.46	18.13	42
10	0.50	-0.03	1.00	130.00	0.46	18.11	39
11	0.40	-0.03	1.00	148.00	0.61	14.99	35
12	0.26	-0.03	1.00	151.00	0.95	9.72	34
13	0.27	-0.03	1.00	140.00	0.99	9.24	32
14	0.27	-0.03	1.00	133.00	0.98	9.36	32
15	0.30	-0.03	1.00	126.00	0.91	10.21	31
16	0.28	-0.04	1.00	117.00	1.07	8.32	29
17	0.14	-0.02	1.00	117.00	1.41	5.36	53
18	0.23	-0.02	1.00	117.00	0.87	10.71	39
19	0.24	-0.03	1.00	116.00	0.98	9.34	35
20	0.25	-0.05	1.00	136.00	1.31	6.13	29
21	0.26	-0.03	1.00	137.00	0.90	10.40	35

After the optimal TH was determined for each sub-image, the crack was identified and highlighted in green, as shown in Figure 4.18. Those areas where the crack has not been identified are because the CNN improperly classified those areas as undamaged sub-images. Therefore, the IP technique was not performed on those sub-images. Comparing with the true pixel-level location of the masonry crack, the confusion matrix for the pixel-level classification of damaged and undamaged was calculated. From the confusion matrix, the accuracy was determined to be 97.86%, while the MCC value was 0.4095. This suggests that the correlation between the predicted and true pixel-level masonry crack detection is only slightly better than a random correlation. Though the accuracy is very high and would suggest a robust method, due to the ill-conditioned nature of the classification, where the undamaged pixels are significantly higher than the damaged ones, this value is misleading. However, compared to the standalone CNN method, the inclusion of an IP technique allows for the detection of masonry cracks at the pixel-level. Conversely,

the inclusion of a CNN network allows for the isolation of cracked areas in the image, improving the accuracy of the typical standalone IP technique.



Figure 4.18: Pixel-level localization of early-age masonry crack.

4.4 Conclusions

This chapter presented a novel hybrid crack detection technique that was used for the pixel level detection of cracks in early-age masonry structures. Data augmentation and image segmentation were used to develop the training, validation, and testing databases for the DL algorithm. A novel IP processing technique was presented for the pixel level detection of masonry cracks using the variation of matrix density, normalization factor, and threshold values over different sub-images. Lastly, the hybrid method was presented, and a case study of early-age masonry cracks was illustrated using this method.

Future research should focus on refining the network parameters of the layers of CNN to improve accuracy. More autonomous techniques based on the loss function should be implemented to hyper-tune CNN more efficiently. Furthermore, additional images of early age masonry structures, both damaged and undamaged, should be compiled to create large image databases for analysis. A comparative study should be conducted against a pixel-wise DL algorithm to compare the program execution duration and the accuracy of the method. Finally, the effect of decreased sub-image size and improved DL accuracy on the

MCC value of the hybrid model for experimental studies should be investigated to improve the correlation between predicted and true masonry cracks at the pixel-level.

4.5 References

Avci, O., Abdeljaber, O., Kiranyaz, S., Hussein, M., Gabbouj, M. and Inman, D. J. (2020), “A Review of Vibration-Based Damage Detection in Civil Structures: From Traditional Methods to Machine Learning and Deep Learning Applications”. *Mechanical Systems and Signal Processing*, 147.

Aszemi, N. and Selvam, D. (2019), “Hyperparameter Optimization in Convolutional Neural Network using Genetic Algorithms”. *International Journal of Advanced Computer Science and Applications*, 10(6).

Azimi, M., Eslamlou, A. D. and Pekcan, G. (2020), “Data-driven structural health monitoring and damage detection through deep learning: state-of-the-art review. *Sensors*, 20, 2778.

Basha, S., Dubey, S. R., Pulabaigari, V. and Mukherjee, S. (2019), “Impact of Fully Connected Layers on Performance of Convolutional Neural Networks for Image Classification”. *Neurocomputing*, 378, 112 – 119. Bergstra, J. and Bengio, Y. (2012), “Random Search for Hyper-Parameter Optimization”. *Journal of Machine Learning Research*, 13, 281-305.

Bjerrum, E., Glahder, M. and Skov, T. (2017), “Data augmentation of Spectral Data for Convolutional Neural Network (CNN) Based Deep Chemometrics”. *arXiv e-print*.

Boughorbel, S., Jarray, F. and El-Anbari, M. (2017), “Optimal classifier for imbalanced data using Matthews Correlation Coefficient metric”. *PLOS ONE*, 12(6): e0177678.

Canny, J. (1986), “A Computational Approach to Edge Detection”. *IEEE Transaction on Pattern Analysis and Machine Intelligence*, 8(6), 679 – 698.

Haar, A. (1910), “Theorie der orthogonalen Funktionensysteme”. *Mathematische Annalen*, 69(3), 331 – 371.

- Krizhevsky, A., Sutskever, I. and Hinton, G. E. (2017), “ImageNet Classification with Deep Convolutional Neural Networks”. *Communications of the ACM*, 60(6), 84 – 90.
- Lee, W., Park, S. and Sim, K., (2018), “Optimal hyperparameter tuning of convolutional neural networks based on the parameter-setting-free harmony search algorithm”, *Optik*, 172, 359 – 367.
- Matthews, B. (1975), “Comparison of the predicted and observed secondary structure of T4 phage lysozyme”. *Biochimica et Biophysica Acta (BBA) – Protein Structure*, 405(2), 442 – 451.
- Mohan, A. and Poobal, S. (2018), “Crack detection using image processing: A critical review and analysis”. *Alexandria Engineering Journal*, 57(2), 787 – 798.
- Nabi, J. (2019, March 16), “Hyper-parameter tuning techniques in deep learning”. Retrieved from towards data science: <https://towardsdatascience.com/hyper-parameter-tuning-techniques-in-deep-learning-4dad592c63c8>.
- Ng, A. (2004), “Feature selection L_1 vs L_2 regularization, and rotational invariance”. *21st International conference on machine learning*. Banff.
- O’Shea, K. and Nash, R. (2015), “An introduction to Convolutional Neural Networks”, *arXiv e-prints*.
- Otsu, N. (1979), “A Threshold Selection Method from Gray-Level Histograms”. *IEEE Transactions on Systems, Man, and Cybernetics*, 9(1), 62 – 66.
- Quan, N. (1999), “On the momentum term in gradient descent learning algorithms”. *Neural Networks*, 12(1), 145 – 151.
- Ren, M. (2017), “Normalizing the normalizers: comparing and extending network normalization schemes”, *arXiv e-print*.
- Sobel, I. (2014), “An Isotropic 3x3 Image Gradient Operator”. *Presenetation at Stanford A.I. Project 1968*.

Szegedy, C., Liu, W., Jia, Y., Sermanet, P., Reed, S., Anguelov, D., Erhan, D., Vanhoucke, V. and Rabinovich, A. (2015), “Going deeper with convolutions”, *2015 IEEE Conference on Computer Vision and Pattern Recognition (CVPR)*, Boston, MA, 1 – 9.

Yamashita, R., Nishio, M., Do, R. and Togashi, K. (2018), “Convolutional neural networks: an overview and application in radiology”. *Insights into Imaging*, 9, 611 – 629.

Zeiler, M. and Fergus, R. (2013), “Visualizing and Understanding Convolutional Networks”. *arXiv e-print*.

5 Conclusions and Summary

This chapter summarizes the experimental and numerical studies and the proposed crack detection method that contributed to the increased understanding of SHM of early-age masonry structures. The contributions of this thesis have been described next, followed by the recommendation for potential future research.

5.1 Conclusions

This thesis proposes improved techniques for the SHM of early-age masonry structures at the construction site. The elastic material properties (i.e., E and σ_d) of early-age masonry assemblages under uniaxial tensile loads were investigated to develop accurate material models. These parameters were used to develop an accurate numerical model that can simulate the response of early-age masonry assemblages under various tensile loads. Lastly, a novel hybrid image processing-enabled deep learning algorithm was presented to detect a crack in early-age masonry walls at the construction site. Based on the overall results of chapters 2-4, the following conclusions are made to broadening the understanding of SHM of early-age masonry structures:

- Under tensile loading, E values and σ_d vary logarithmically with respect to curing time between 3-72 hours for the specified concrete block and mortar type.
- The masonry assemblages failed primarily due to debonding at the block-mortar interface under uniaxial tensile loads for all curing periods.
- Cohesion-based interaction surfaces can be considered as an accurate modeling technique to represent the failure mechanism of early-age masonry structures in a numerical simulation.
- Deep learning algorithms can effectively isolate sub-areas of images in which image processing techniques can accurately and efficiently localize the cracks in early-age masonry structures.

5.2 Contributions

In this thesis, intensive experimental and numerical studies are conducted to investigate the material properties of early-age masonry prisms. To the best of the author's knowledge, material properties of early-age masonry at various curing period have not yet been investigated in the literature. Lack of such information forms a hindrance to effectively design temporary bracing for premature masonry walls within the first few hours of construction at the job site. Moreover, a novel hybrid crack detection method is developed that can detect and localize cracks in early-age masonry at the construction site. The key contributions of the thesis are listed below:

- The E and σ_d of early-age masonry assemblages under uniaxial tensile loads were first time experimentally quantified for up to an initial 72-hour curing period.
- These parameters were used to develop an accurate material model to be interfaced with a numerical model that simulated the accurate response of early-age masonry assemblages under various tensile loads. The effect of stress concentrations on modeling accuracy due to rapid changes in geometric cross-section was quantified and used to improve model accuracy. A preliminary macroscopic model for capturing the global behavior of a masonry wall under wind loading was presented to justify further study of this topic.
- A hybrid image processing-based deep learning algorithm was developed for the detection of cracks in masonry walls under construction. The proposed method would allow damages to be readily localized such that they could be addressed and retrofitted on-site, immediately preventing further damage.

5.3 Future Work

With due course of this research, the following future work is recommended to expand the current work.

- In this thesis, only the tensile behavior of early-age masonry has been explored. Future research should investigate the behavior of early-age masonry under uniaxial compression and bending. Additionally, the effect of different block types,

dimensions, and different mortar compositions should be varied, and their effects should be explored.

- The parameters of the numerical model developed, in particular the cohesive-based interface, will need to be further updated once the flexural behavior of early-age masonry is investigated, as mentioned above.
- Full-scale testing of an early-age masonry wall must be conducted to confirm the validity of the case study presented. Also, the effect of cyclic loading on masonry walls needs to be investigated to quantify accurate response behavior during time-varying lateral loads such as winds and earthquakes.
- Further hyper-tuning should be conducted on the proposed hybrid model to improve the accuracy of crack detection for early-age masonry structures. Additionally, the image database used to train the DL algorithm should be diversified to include additional masonry materials such as clay or lime-based bricks.
- A comparative study should be conducted against a pixel-wise CNN algorithm to compare the program execution duration and the accuracy of the method. Additionally, the effect of sub-image size and different damage types on the robustness of the method should be investigated.

Appendices

Appendix A.1: Summary of tensile Parameters at 3-hour curing.

Prism #	σ_d (kPa)	ϵ_d	E (MPa)	R^2	Curing Period (Hrs)
1	11.5	0.0105	0.87	0.76	3.07
2	13.5	0.0091	1.40	0.98	3.28
3	9.6	0.0061	1.36	0.97	3.20
4	12.2	0.0052	2.38	0.99	3.38
5	11.0	0.0028	3.91	0.98	3.12
6	13.0	0.0016	10.28	0.88	3.13
7	10.4	0.0010	15.65	0.92	3.47
8	17.6	0.0043	4.45	0.98	2.88
9	13.7	0.0082	1.91	0.86	3.03
10	18.0	0.0108	1.78	0.92	3.23
Average	13.0	0.0059	4.40		3.18
COV	21.6%	60.4%	109.6%		5.4%

Appendix B.2: Summary of tensile Parameters at 4-hour curing.

Prism #	σ_d (kPa)	ϵ_d	E (MPa)	R^2	Curing Period (Hrs)
1	12.2	0.0091	0.32	0.70	3.63
2	13.5	0.0076	1.68	0.95	3.85
3	10.3	0.0038	2.70	1.00	3.98
4	10.3	0.0080	2.11	0.96	4.07
5	17.3	0.0042	3.39	0.89	3.63
6	12.4	0.0030	3.71	0.97	3.77
7	10.8	0.0036	2.72	0.95	3.88
8	14.4	0.0042	3.01	0.98	4.03
9	18.1	0.0056	2.89	0.91	4.08
10	22.6	0.0111	2.02	0.99	4.08
11	10.0	0.0020	5.90	0.98	3.62
Average	13.8	0.0056	2.77		3.87
COV	29.2%	51.2%	50.2%		4.9%

Appendix C.3: Summary of tensile parameters at 6-hour curing.

Prism #	σ_d (kPa)	ϵ_d	E (MPa)	R^2	Curing Period (Hrs)
1	12.2	0.0052	2.17	0.97	5.77
2	17.1	0.0172	0.89	0.93	6.26
3	12.5	0.0022	6.03	0.97	6.07
4	21.8	0.0052	4.71	0.94	6.08
5	18.4	0.0078	2.73	0.87	6.25
6	34.6	0.0078	4.07	0.94	6.40
7	20.5	0.0096	2.27	0.85	6.50
Average	19.6	0.0078	3.27		6.19
COV	38.6%	61.1%	53.7%		3.9%

Appendix D.4: Summary of tensile parameters at 7-hour curing.

Prism #	σ_d (kPa)	ϵ_d	E (MPa)	R^2	Curing Period (Hrs)
1	5.9	0.0143	3.15	0.87	6.65
2	24.1	0.0014	1.90	0.85	6.97
3	20.5	0.0024	10.92	0.86	7.13
4	27.0	0.0039	6.60	0.79	7.25
5	20.3	0.0024	8.92	0.97	6.98
6	19.0	0.0039	5.03	0.70	7.25
7	17.1	0.0022	9.93	0.73	7.40
8	16.3	0.0055	3.58	0.82	6.70
9	10.8	0.0009	13.74	0.96	6.90
10	22.7	0.0122	1.90	0.99	7.05
Average	18.4	0.0049	6.57		7.03
COV	34.1%	94.1%	63.0%		3.4%

Appendix E.5: Summary of tensile parameters at 13-hour curing.

Prism #	σ_d (kPa)	ϵ_d	E (MPa)	R^2	Curing Period (Hrs)
Prism 1	32.6	0.0033	11.11	0.89	12.32
Prism 2	32.0	0.0095	5.65	0.96	12.47
Prism 3	39.8	0.0061	5.99	0.94	12.72
Prism 4	37.4	0.0032	13.29	0.91	12.92
Prism 5	24.8	0.0078	3.19	0.84	13.12
Prism 6	35.0	0.0024	10.12	0.97	13.67
Prism 7	34.7	0.0100	3.34	0.93	13.85
Average	33.7	0.0060	7.53		13.01
COV	14.1%	52.1%	52.9%		4.5%

Appendix F.6: Summary of tensile parameters at 18-hour curing.

Prism #	σ_d (kPa)	ϵ_d	E (MPa)	R^2	Curing Period (Hrs)
1	39.8	0.0058	6.10	0.92	18.25
2	61.6	0.0116	2.68	0.89	18.47
3	33.7	0.0035	10.74	0.82	18.00
4	31.8	0.0030	10.93	0.98	18.18
5	35.6	0.0039	8.82	0.98	18.33
6	34.4	0.0036	10.52	0.87	18.55
7	35.0	0.0024	13.73	0.95	17.73
8	34.7	0.0034	10.20	0.99	17.93
9	26.3	0.0009	36.27	0.80	18.20
10	26.3	0.0020	13.68	0.94	18.40
11	27.3	0.0027	10.32	0.84	18.07
12	27.7	0.0041	7.65	0.80	18.35
13	45.3	0.0040	10.50	0.89	18.60
14	60.4	0.0060	9.35	0.94	18.80
Average	37.1	0.0041	11.53		18.28
COV	30.8%	62.8%	66.4%		1.6%

Appendix G.7: Summary of tensile parameters at 24-hour curing.

Prism #	σ_d (kPa)	ϵ_d	E (MPa)	R^2	Curing Period (Hrs)
1	32.9	0.0045	11.09	0.98	23.85
2	50.3	0.0064	6.49	0.86	24.17
3	40.8	0.0069	5.47	0.98	23.67
4	49.0	0.0172	2.66	0.98	24.15
5	34.5	0.0073	5.03	0.95	24.12
6	38.2	0.0051	6.35	0.87	24.50
7	34.3	0.0069	4.39	0.96	23.97
8	32.9	0.0056	8.49	0.98	24.95
9	44.6	0.0078	4.65	0.89	25.28
10	43.7	0.0105	4.41	0.96	24.92
Average	40.1	0.0078	5.90		24.36
COV	16.4%	47.3%	40.6%		2.2%

Appendix H.8: Summary of tensile parameters at 48-hour curing.

Prism #	σ_d (kPa)	ϵ_d	E (MPa)	R^2	Curing Period (Hrs)
1	60.42	0.0030	22.92	0.70	47.92
2	44.18	0.0016	29.20	0.96	48.28
3	66.98	0.0084	7.65	0.94	48.62
4	42.06	0.0057	8.95	0.88	48.07
5	50.20	0.0214	2.44	0.95	48.35
6	28.08	0.0026	12.24	0.92	48.60
7	47.53	0.0050	8.33	0.89	48.80
8	34.56	0.0034	9.33	0.88	48.08
9	31.34	0.0059	4.79	0.88	48.27
10	40.59	0.0018	25.03	0.87	48.90
11	33.63	0.0084	3.96	0.97	49.15
Average	43.60	0.0061	12.26		48.46
COV	27.8%	91.7%	74.8%		0.8%

Appendix I.9: Summary of tensile parameters at 72-hour curing.

Prism #	σ_d (kPa)	ε_d	E (MPa)	R^2	Curing Period (Hrs)
1	57.5	0.0045	13.44	0.97	72.28
2	64.3	0.0023	24.12	0.93	72.55
3	81.3	0.0047	17.57	0.99	72.85
4	62.6	0.0105	5.27	0.94	73.08
5	41.8	0.0085	4.15	0.95	72.30
6	43.5	0.0152	3.08	0.81	72.47
7	58.4	0.0042	12.83	0.91	72.67
8	53.5	0.0085	6.51	0.98	72.88
9	26.5	0.0077	3.34	0.99	72.10
10	38.8	0.0059	6.71	0.98	72.37
11	38.2	0.0047	8.97	0.96	72.57
12	52.9	0.0058	7.66	0.92	72.75
Average	51.6	0.0069	9.47		72.57
COV	28.5%	50.7%	67.6%		0.4%

Appendix J.1: Strength parameters of a 4-hour cured sample in ABAQUS.

Parameter	Concrete Masonry Unit (CMU)	Type S Mortar 4-Hours Cured
ρ (ton/mm ³)	2.00e-09	2.00e-09
ν	0.25	0.25
E (MPa)	2.31	2.01

Appendix K.2: Strength parameters of a 6-hour cured sample in ABAQUS.

Parameter	Concrete Masonry Unit (CMU)	Type S Mortar 6-Hours Cured
ρ (ton/mm ³)	2.00e-09	2.00e-09
ν	0.25	0.25
E (MPa)	2.73	2.37

Appendix L.3: Strength parameters of a 7-hour cured sample in ABAQUS.

Parameter	Concrete Masonry Unit (CMU)	Type S Mortar 7-Hours Cured
ρ (ton/mm ³)	2.00e-09	2.00e-09
ν	0.25	0.25
E (MPa)	2.88	2.51

Appendix M.4: Strength parameters of a 13-hour cured sample in ABAQUS.

Parameter	Concrete Masonry Unit (CMU)	Type S Mortar 13-Hours Cured
ρ (ton/mm ³)	2.00e-09	2.00e-09
ν	0.25	0.25
E (MPa)	3.52	3.06

Appendix N.5: Strength parameters of a 18-hour cured sample in ABAQUS.

Parameter	Concrete Masonry Unit (CMU)	Type S Mortar 18-Hours Cured
ρ (ton/mm ³)	2.00e-09	2.00e-09
ν	0.25	0.25
E (MPa)	3.86	3.36

Appendix O.6: Strength parameters of a 24-hour cured sample in ABAQUS.

Parameter	Concrete Masonry Unit (CMU)	Type S Mortar 24-Hours Cured
ρ (ton/mm ³)	2.00e-09	2.00e-09
ν	0.25	0.25
E (MPa)	4.15	3.61

Appendix P.7: Strength parameters of a 48-hour cured sample in ABAQUS.

Parameter	Concrete Masonry Unit (CMU)	Type S Mortar 48-Hours Cured
ρ (ton/mm ³)	2.00e-09	2.00e-09
ν	0.25	0.25
E (MPa)	4.87	4.23

Appendix Q.8: Strength parameters of a 72-hour cured sample in ABAQUS.

Parameter	Concrete Masonry Unit (CMU)	Type S Mortar 72-Hours Cured
ρ (ton/mm ³)	2.00e-09	2.00e-09
ν	0.25	0.25
E (MPa)	5.28	4.60

Appendix R.1: Material model for cohesion-based contact elements for a 4-hour curing period.

Parameter	Mortar Joint
Cohesive Stiffness	
K_{nn} (N/mm ³)	0.201
K_{ss} (N/mm ³)	0.201
K_{tt} (N/mm ³)	0.201
Damage Initiation	
t_n^o (MPa)	0.033
t_s^o (MPa)	0.033
t_t^o (MPa)	0.033
Damage Evolution	
Total/plastic Displacement	0.00001

Appendix S.2: Material model for cohesion-based contact elements for a 6-hour curing period.

Parameter	Mortar Joint
Cohesive Stiffness	
K_{nn} (N/mm ³)	0.237
K_{ss} (N/mm ³)	0.237
K_{tt} (N/mm ³)	0.237
Damage Initiation	
t_n^o (MPa)	0.044
t_s^o (MPa)	0.044
t_t^o (MPa)	0.044
Damage Evolution	
Total/plastic Displacement	0.00001

Appendix T.3: Material model for cohesion-based contact elements for a 7-hour curing period.

Parameter	Mortar Joint
Cohesive Stiffness	
K_{nn} (N/mm ³)	0.251
K_{ss} (N/mm ³)	0.251
K_{tt} (N/mm ³)	0.251
Damage Initiation	
t_n^o (MPa)	0.049
t_s^o (MPa)	0.049
t_t^o (MPa)	0.049
Damage Evolution	
Total/plastic Displacement	0.00001

Appendix U.4: Material model for cohesion-based contact elements for a 13-hour curing period.

Parameter	Mortar Joint
Cohesive Stiffness	
K_{nn} (N/mm ³)	0.352
K_{ss} (N/mm ³)	0.352
K_{tt} (N/mm ³)	0.352
Damage Initiation	
t_n^o (MPa)	0.079
t_s^o (MPa)	0.079
t_t^o (MPa)	0.079
Damage Evolution	
Total/plastic Displacement	0.00001

Appendix V.5: Material model for cohesion-based contact elements for a 18-hour curing period.

Parameter	Mortar Joint
Cohesive Stiffness	
K_{nn} (N/mm ³)	0.386
K_{ss} (N/mm ³)	0.386
K_{tt} (N/mm ³)	0.386
Damage Initiation	
t_n^o (MPa)	0.090
t_s^o (MPa)	0.090
t_t^o (MPa)	0.090
Damage Evolution	
Total/plastic Displacement	0.00001

Appendix W.6: Material model for cohesion-based contact elements for a 24-hour curing period.

Parameter	Mortar Joint
Cohesive Stiffness	
K_{nn} (N/mm ³)	0.415
K_{ss} (N/mm ³)	0.415
K_{tt} (N/mm ³)	0.415
Damage Initiation	
t_n^o (MPa)	0.100
t_s^o (MPa)	0.100
t_t^o (MPa)	0.100
Damage Evolution	
Total/plastic Displacement	0.00001

Appendix X.7: Material model for cohesion-based contact elements for a 48-hour curing period.

Parameter	Mortar Joint
Cohesive Stiffness	
K_{nn} (N/mm ³)	0.487
K_{ss} (N/mm ³)	0.487
K_{tt} (N/mm ³)	0.487
Damage Initiation	
t_n^o (MPa)	0.123
t_s^o (MPa)	0.123
t_t^o (MPa)	0.123
Damage Evolution	
Total/plastic Displacement	0.00001

Appendix Y.8: Material model for cohesion-based contact elements for a 72-hour curing period.

Parameter	Mortar Joint
Cohesive Stiffness	
K_{nn} (N/mm ³)	0.528
K_{ss} (N/mm ³)	0.528
K_{tt} (N/mm ³)	0.528
Damage Initiation	
t_n^o (MPa)	0.137
t_s^o (MPa)	0.137
t_t^o (MPa)	0.137
Damage Evolution	
Total/plastic Displacement	0.00001

Curriculum Vitae

Name: Kyle Dunphy

Post-secondary Education and Degrees: St. Lawrence University
Kingston, Ontario, Canada
2013-2016 Advanced Diploma – Civil Engineering Technology

Lakehead University
Thunder Bay, Ontario, Canada
2016-2018 Bachelor of Engineering – Civil

The University of Western Ontario
London, Ontario, Canada
2018-2020 Masters of Engineering Science - Structural

Honors and Awards: Province of Ontario Graduate Scholarship
2020-2021

Mitacs Accelerate Internship
2019-2020

NSERC USRA
2017-2018

Related Work Experience Teaching Assistant
The University of Western Ontario
2018-2020

Publications:

Sadhu, A., **Dunphy, K.**, Zerpa, C. (2019), “Investigation of vibration data-based human load monitoring system”. *Structural Health Monitoring*, SAGE, <https://doi.org/10.1177/1475921719836254>.

Sony, S., **Dunphy, K.**, Sadhu, A. and Capretz, M. (2020), “A systematic review of convolutional neural network-based structural condition assessment techniques”. *Engineering Structures*, Elsevier. (*Under Revision*).

Dunphy, K., Sadhu, A. and Banting, B. “Experimental and numerical investigation of tensile properties of early-age masonry”, (*Under Review*).

Dunphy, K. and Sadhu, A. “Hybrid crack detection and localization in masonry structures”, (*Under Review*).